Università degli Studi di Ferrara

DOTTORATO DI RICERCA IN
FISICA

CICLO XXII

COORDINATORE Prof. Filippo Frontera

The spatial alignment of the Muon Detector for the LHCb experiment

Settore Scientifico Disciplinare FIS/01

Dottoranda
Dott. Silvia Pozzi

Tutore
Prof. Mauro Savriè

Correlatrice
Dott. Stefania Vecchi

Anni 2007/2009

Disse e sparve. L'eroe balza dal cocchio
risonante nell'armi, e nella mano
palleggiando la lancia il campo scorre,
e raccende la pugna. Allor destossi
grande il conflitto. Rivoltaro i Teucri
agli Achivi la faccia, e di rincontro
le lor falangi rinforzâr gli Achivi.
Venuti a fronte, rinnovossi il cozzo,
e primiero si mosse Agamennóne
innanzi a tutti di pugnar bramoso.

Iliade, Libro XI

With his weapons Hector jumped out of his chariot
down to the ground. Brandishing his sharp spear, he moved
all through the army, urging men to battle on,
encouraging their spirits for the dreadful fight.
The troops rallied and stood up against Achaeans.
Opposing them, the Argives reinforced their ranks.
Agamemnon was among them, first to charge ahead,
eager to fight well out in front of everyone.

Iliad, Book XI

Contents

List of Figures

List of Tables

Introduction

The phenomenology of particle physics is well described by the Standard Model. However, some of the parameters of the model are not predicted and have to be experimentally determined, as for instance, the four parameters of the quark mixing matrix, the Cabibbo-Kobayashi-Maskawa (CKM) matrix. One of these parameters, the phase of the CKM matrix, is responsible of the violation of the CP symmetry that was identified as one of the causes for the asymmetry between matter and anti-matter in the Universe [1].

LHCb is one of the four experiments of particle physics at the Large Hadron Collider accelerator built at CERN.

The LHCb experiment is dedicated to high precision measurement of CP violating parameters in the system of B mesons. The large samples of $B - \overline{B}$ pairs that will be produced allow to measure very rare B decays like $B_s \rightarrow \mu^+\mu^-$. The branching ratio predicted by the Standard Model for this decay is of the order of $O(10^{-9})$, but it can receive large contributions by virtual processes involving new particles.

The challenge of the LHCb experiment is to efficiently discriminate the events of interest from the background produced by the $p - p$ collisions. For this reason the experiment is equipped not only with specific detectors, but also with an efficient trigger system, in which the Muon Detector plays an important role. The Muon Detector task, in the first stage of the trigger system, is the detection of muons with high transverse momentum[1]. Moreover, in the high level trigger and in the off-line

[1]Given the large mass of the B mesons, their decay products have a transverse momentum larger than the background particles.

reconstruction the Muon Detector provides the muon identification. The information on muons in the final states of B meson decays are used by the tagging algorithms for the determination of the b flavour of the decaying B mesons. This procedure is of great relevance in CP violation measurements.

Because of the role it plays in the experiment, it is crucial to know the actual position of the Muon Detector, and to monitor it during the time. This is the aim of the software alignment of the detector and the subject of this thesis.

The software procedure to align the Muon Detector, locally and globally, has been carried out developing specific algorithms for the track finding and reconstruction. The reconstructed tracks have been expressed in the standard LHCb track format and fitted with the default LHCb track fit method. The Muon Detector software alignment procedure has been tested with three kinds of data: Monte Carlo muons coming from the interaction point, real cosmic rays and Monte Carlo cosmic data. The real cosmic rays, analysed in this work, have been the first experimental data ever acquired by LHCb.

This thesis is divided in the following chapters:

Chapter 1 describes the CP violation in the Standard Model of particles with the phenomenology of interest in the LHCb experiment.

Chapter 2 briefly describes LHC and then discusses all the detectors that constitute the LHCb experiment.

Chapter 3 is entirely dedicated to the Muon Detector for its relevance to this thesis.

In Chapter 4 the alignment methods used are described.

Chapter 5, after a brief description of the LHCb software organisation, discusses the first test of the global alignment procedure applied to the Muon Detector, and performed with Monte Carlo data of single muons coming from the interaction point.

With real cosmic rays a local alignment of the Muon Detector was performed. In addition a preliminary study for a relative alignment of the detector with respect to the Outer Tracker was also carried on. This

is the subject of Chapter 6.

In Chapter 7 a Monte Carlo cosmic data sample has been produced for testing the local alignment performed with real cosmic rays and for studying local systematics arising from the acceptance of the Muon Detector unsuited for the cosmic ray geometry.

Chapter 1

B physics

After the first observation of CP violation in an experiment on the decay of the neutral K mesons (1964) by J. H. Christenson, J. W. Cronin, V. L. Fitch and R. Turlay [2] the same effect was observed in the neutral B mesons by the B factories experiments like BaBar [3] and Belle [4] in 2001. These phenomena are related to the presence of a complex phase in the matrix of Cabibbo-Kobayashi-Maskawa, the rotation matrix of the quark fields from the basis of the mass eigenstates to the basis of the flavour eigenstates.

The Standard Model describes three of the fundamental interactions (strong, weak and electromagnetic) owing to the unification of QED, QCD and weak interaction. This last is responsible of the CP violation.

The aim of the LHCb experiment is to perform precise measurements of CP violating quantities in the B sector.

Six measurements are singled out for constraining or discovering new physics, where LHCb can have a large impact even since its early period of data taking. These are the tree level determination of the angle γ of the Unitarity Triangle, the charmless charged two body hadron B decay, the mixing induced CP violation in $B_s \to J/\psi\phi$, the rare decay $B_s \to \mu^+\mu^-$, the decay $B^0 \to K^{0*}\mu^+\mu^-$ where forward-backward asymmetry in the leptons can discriminate between different models of new physics, and the radiative decay $B^0 \to \phi\gamma$ [5].

This chapter deals with several theorethical aspects. After an intro-

duction on the CKM matrix and the conditions that lead to the construction of the Unitarity Triangles, the three types of CP violation in the neutral B meson system are described: the CP violation in the decay, in the mixing, and in the interference between decay and mixing.

1.0.1 The CKM matrix

Since in the Standard Model the quarks in the basis of mass eigenstates and weak interaction eigenstes are not the same, the two bases are related by the unitary transformations

$$\begin{aligned} u_{Li} &= U^u_{ij} u'_{Lj}, \qquad d_{Li} = U^d_{ij} d'_{Lj} \\ u_{Ri} &= V^u_{ij} u'_{Rj}, \qquad d_{Ri} = V^d_{ij} d'_{Rj}, \end{aligned} \tag{1.1}$$

where

$$\begin{aligned} u_{L_i} &= (u_L, c_L, t_L), \qquad d_{L_i} = (d_L, s_L, b_L) \\ u_{R_i} &= (u_R, c_R, t_R), \qquad d_{R_i} = (d_R, s_R, b_R) \end{aligned} \tag{1.2}$$

are the weak interaction eigenstates and

$$\begin{aligned} u'_{L_i} &= (u'_L, c'_L, t'_L), \qquad d'_{L_i} = (d'_L, s'_L, b'_L) \\ u'_{R_i} &= (u'_R, c'_R, t'_R), \qquad d'_{R_i} = (d'_R, s'_R, b'_R) \end{aligned} \tag{1.3}$$

the mass eigenstates.

The mass terms in the Lagrangian are

$$\Delta\mathcal{L}_M = -\overline{d}_{Li} M^{d,diag}_{ij} d_{Rj} - \overline{u}_{Li} M^{u,diag}_{ij} u_{Rj} + \text{h.c.} \tag{1.4}$$

where M^{diag}_{ij} is the mass matrix

$$\begin{aligned} M^{u,diag}_{ij} &= \frac{v}{\sqrt{2}} (U^u)^\dagger_{il} Y^u_{lm} V^u_{mj} = (U^u)^\dagger_{il} M^u_{lm} V^u_{mj} \\ M^{d,diag}_{ij} &= \frac{v}{\sqrt{2}} (U^d)^\dagger_{il} Y^d_{lm} V^d_{mj} = (U^d)^\dagger_{il} M^d_{lm} V^d_{mj}, \end{aligned} \tag{1.5}$$

and v the vacuum expectation value of the physical Higgs field. In this basis the vector current of the W boson assumes the shape

$$J_W^{\mu+} = \frac{1}{\sqrt{2}}\overline{u}_{Li}\gamma^\mu d_{Li} = \frac{1}{\sqrt{2}}\overline{u}'_{Li}\gamma^\mu (U^{u\dagger}U^d)_{ij} d'_{Lj} = \frac{1}{\sqrt{2}}\overline{u}'_{Li}\gamma^\mu V_{ij} d'_{Lj} \quad (1.6)$$

where $V_{ij} = (U^{u\dagger}U^d)_{ij}$ is the Cabibbo-Kobayashi-Maskawa matrix (CKM).

The definition of the CKM matrix is not unique, in fact the three families of quarks can be permuted. In general it is preferred the permutation that allows to arrange the quarks according to increasing values of mass (u, c, t) and (d, s, b). Besides, the mass matrix M^{diag} does not change if matrices U and V are multiplied by a diagonal matrix containing only phases.

The CKM matrix is a unitary matrix $n \times n$ with complex elements that rotates the quark fields in the flavour space, where n is the number of the quark families of the theory. The unitarity condition set n^2 constraints, and $2n^2 - 1$ phases can be absorbed redefining the quark fields. Of the remaining $(n^2 - 1)$ physical parameters, $n(n-1)/2$ are angles and $(n-1)(n-2)/2$ are phases that can not be eliminated. Thus, with three generations of quarks the matrix is parametrised by three angles and one phase.

In literature several parametrisations of the CKM matrix have been proposed, but the standard [6] and the Wolfenstein [7] parametrisations are the most used. Calling $c_{ij} = \cos\vartheta_{ij}$ e $s_{ij} = \sin\vartheta_{ij}$ $(i, j = 1, 2, 3)$ the standard parametrisation is given by

$$\mathbf{V}_{\mathrm{CKM}} = \begin{pmatrix} c_{12}c_{13} & s_{12}c_{13} & s_{13}e^{-i\delta} \\ -s_{12}c_{23} - c_{12}s_{23}s_{13}e^{i\delta} & c_{12}c_{23} - s_{12}s_{23}s_{13}e^{i\delta} & s_{23}c_{13} \\ s_{12}s_{23} - c_{12}c_{23}s_{13}e^{i\delta} & -s_{23}c_{12} - s_{12}c_{23}s_{13}e^{i\delta} & c_{23}c_{13} \end{pmatrix} \quad (1.7)$$

where δ is the phase that can not be eliminated and that violates CP. It is possible to choose c_{ij} e s_{ij} positive and δ in the range $[0, 2\pi]$.

The absolute values of the CKM elements, experimentally measured, show a hierarchical pattern with the diagonal elements $(|V_{ud}|, |V_{cs}|, |V_{tb}|)$ close to one, $|V_{us}|$ and $|V_{cd}|$ of the order of 0.2, $|V_{cb}|$ and $|V_{ts}|$ of the order of

5×10^{-2}, and $|V_{ub}|$ and $|V_{td}|$ of the order of 5×10^{-3} [8]. The Wolfenstein parametrisation explicitely shows this hierarchy. It is an approximate parametrisation of the CKM matrix, in which the elements are expanded in powerful series of the parameter $\lambda = \sin\vartheta_{12} \approx 0.22$ [7]

$$\mathbf{V}_{CKM} = \begin{pmatrix} 1 - \frac{\lambda^2}{2} & \lambda & A\lambda^3(\rho - i\eta) \\ -\lambda & 1 - \frac{\lambda^2}{2} & A\lambda^2 \\ A\lambda^3(1 - \rho - i\eta) & -A\lambda^2 & 1 \end{pmatrix} + \mathcal{O}(\lambda^4) \qquad (1.8)$$

where the independent parameters are

$$\lambda, \quad A, \quad \rho, \quad \eta. \qquad (1.9)$$

They can be defined by the following relations with the parameters of the standard parametrisation

$$s_{12} = \lambda, \qquad s_{23} = A\lambda^2, \qquad s_{13}e^{-i\delta} = A\lambda^3(\rho - i\eta) \qquad (1.10)$$

valid for all the orders in λ. Expanded up to the order λ^5, the CKM matrix in the Wolfenstein parametrisation can be generalised as [9]

$$\begin{pmatrix} 1 - \frac{\lambda^2}{2} - \frac{\lambda^4}{8} & \lambda + \mathcal{O}(\lambda^7) & A\lambda^3(\rho - i\eta) \\ -\lambda + \frac{A^2\lambda^5}{2}(1 - 2(\rho + i\eta)) & 1 - \frac{\lambda^2}{2} - \frac{\lambda^4}{8}(1 + 4A^2) & A\lambda^2 + \mathcal{O}(\lambda^8) \\ A\lambda^3(1 - \overline{\rho} - i\overline{\eta}) & -A\lambda^2 + \frac{A\lambda^4}{2}(1 - 2(\rho + i\eta)) & 1 - \frac{A^2\lambda^4}{2} \end{pmatrix}, \qquad (1.11)$$

where the new parameters are introduced

$$\overline{\rho} = \rho(1 - \frac{\lambda^2}{2}) \quad \text{and} \quad \overline{\eta} = \eta(1 - \frac{\lambda^2}{2}). \qquad (1.12)$$

By definition the expression for V_{ub} does not change with respect to the original Wolfenstein parametrisation, and the corrections to V_{us} and V_{cb} appear only at the λ^7 and λ^8 orders. The advantage of this generalisation is the absence of large corrections to V_{us}, V_{cd}, V_{ub} and V_{cb}, and the fact that the unitarity triangle (discussed in the next section) expressed in terms of $\overline{\rho}$ and $\overline{\eta}$ does not receive higher order corrections.

1.0.2 The Unitarity Triangle

The unitarity of the CKM matrix imposes the following relations among its elements

$$\sum_k V_{ik}V_{jk}^* = \delta_{ij}\,, \quad \text{where } \; k = \{u\,, c\,, t\} \; \text{ and } \; i,\, j = \{d\,, s\,, b\}. \tag{1.13}$$

The off-diagonal relations can be represented as unitarity triangles in the complex plane. Sides and angles af these triangles are invariant under phase transformations of the quark fields, while the triangles are rotated in the $(\overline{\rho}, \overline{\eta})$ plane by a phase transformation.

The structure of the triangles corresponding to relations in Eq. (1.13) is

$$\mathcal{O}(\lambda) + \mathcal{O}(\lambda) + \mathcal{O}(\lambda^5) \quad = 0 \qquad \text{for} \quad \begin{cases} i{=}d,\ j{=}s \\ i{=}d,\ j{=}d \end{cases} \tag{1.14}$$

$$\mathcal{O}(\lambda^3) + \mathcal{O}(\lambda^3) + \mathcal{O}(\lambda^3) = 0 \qquad \text{for} \quad \begin{cases} i{=}d,\ j{=}b \\ i{=}b,\ j{=}d \end{cases} \tag{1.15}$$

$$\mathcal{O}(\lambda^4) + \mathcal{O}(\lambda^2) + \mathcal{O}(\lambda^2) = 0 \qquad \text{for} \quad \begin{cases} i{=}s,\ j{=}b \\ i{=}b,\ j{=}s \end{cases} \tag{1.16}$$

thus only in two cases the three sides are of the same order of magnitude.

One of these is the unitarity triangle unsually considered

$$V_{ud}V_{ub}^* + V_{cd}V_{cb}^* + V_{td}V_{tb}^* = 0. \tag{1.17}$$

Since

$$V_{cd}V_{cb}^* = -A\lambda^3 + \mathcal{O}(\lambda^7), \tag{1.18}$$

with great accuracy $V_{cd}V_{cb}^*$ is real, with $|V_{cd}V_{cb}^*| = A\lambda^3$. Limiting to the order $\mathcal{O}(\lambda^5)$ and scaling all the terms in Eq. (1.17) of a factor $A\lambda^3$, it is possible to represent equation Eq. (1.17) as a triangle in the complex plane $(\overline{\rho}, \overline{\eta})$, with the vertices in $B(1,0)$ and $C(0,0)$, as shown in

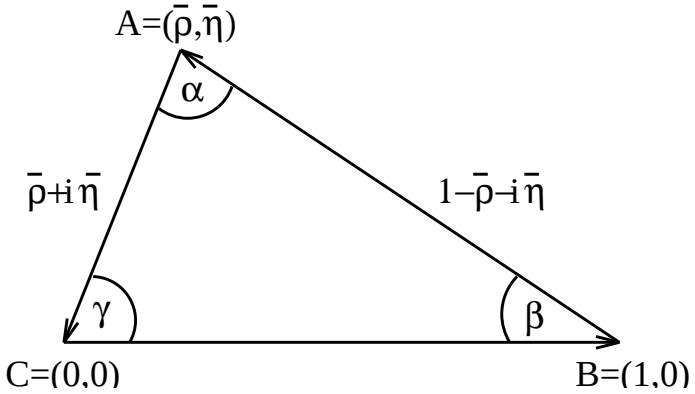

Figure 1.1: The unitarity triangle corresponding to the relation Eq. (1.17) scaled, in the complex plane.

Figure 1.1, and with the length of the sides given by

$$R_b \equiv \overline{AC} = \frac{|V_{ud}V_{ub}^*|}{|V_{cd}V_{cb}^*|} = \sqrt{\overline{\rho}^2 + \overline{\eta}^2} = \left(1 - \frac{\lambda^2}{2}\right)\frac{1}{\lambda}\left|\frac{V_{ub}}{V_{cb}}\right| \tag{1.19}$$

$$R_t \equiv \overline{AB} = \frac{|V_{td}V_{tb}^*|}{|V_{cd}V_{cb}^*|} = \sqrt{(1-\overline{\rho})^2 + \overline{\eta}^2} = \frac{1}{\lambda}\left|\frac{V_{tb}}{V_{cb}}\right|. \tag{1.20}$$

The angles β and γ (with $\gamma = \delta$, the phase of the CKM matrix of Eq. (1.7)) in the convention of phase of the CKM matrix of the unitarity triangle are related with the complex phase of the elements V_{td} e V_{ub} of the CKM matrix through

$$V_{td} = |V_{td}|e^{-i(\beta-\pi)}, \qquad V_{ub} = |V_{ub}|e^{-i(\gamma+\pi)}. \tag{1.21}$$

Each angle is related to the relative phase of the two adjacent sides

$$\alpha = \arg\left(-\frac{V_{td}V_{tb}^*}{V_{cd}V_{cb}^*}\right),\ \beta = \arg\left(-\frac{V_{cd}V_{cb}^*}{V_{td}V_{tb}^*}\right),\ \gamma = \arg\left(-\frac{V_{ud}V_{ub}^*}{V_{cd}V_{cb}^*}\right), \tag{1.22}$$

the unitarity relation can then be rewritten as

$$R_b e^{i\gamma} + R_t e^{-i\beta} = 1\,. \tag{1.23}$$

The Standard Model, with three families of quarks and leptons pre-

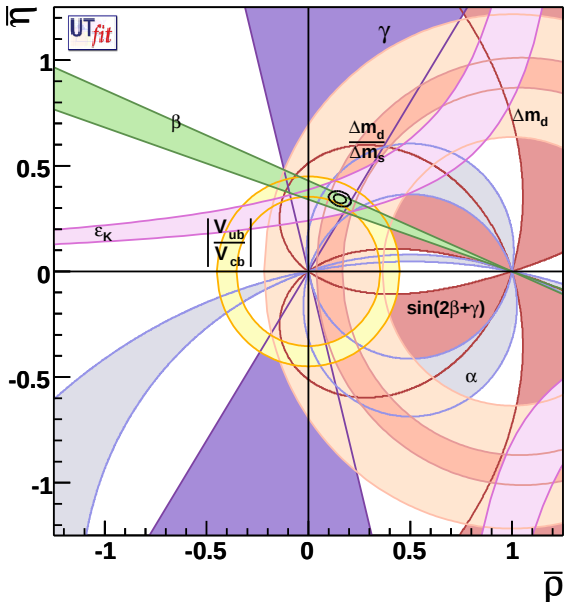

Figure 1.2: The Standard Model constraints to the Unitarity Triangle: the experimental determination of $|V_{ub}/V_{cb}|$, of Δm_{B_d}, of $\Delta m_{B_d}/\Delta m_{B_s}$, of the parameter describing the CP violation in the K system ε_K, $\sin 2\beta$.

dicts that all the processes that violate CP are correlated so that the values of $\overline{\rho}$ e $\overline{\eta}$ are consistent with the vertex of the triangle $A(\overline{\rho}, \overline{\eta})$ as shown in Figure 1.2 [10].

1.1 The neutral B meson system

There are two self-conjugate pairs of mesons involving b quarks, namely the B_d and B_s mesons. They are made by the b and $\overline{b}$ quarks together with a d and a s quark respectively ($B_d = d\overline{b}$, $B_s = s\overline{b}$). In the neutral B meson system different neutral states are present: the two flavour eigenstates and the Hamiltonian eigenstates, that have defined mass and lifetime. The mass eigenstates are also CP eigenstates if CP were a good symmetry.

The time evolution of B^0 and $\overline{B}^0$ is given by the Schrödinger equation

$$i\frac{d}{dt}\begin{pmatrix} B^0 \\ \overline{B}^0 \end{pmatrix} = H\begin{pmatrix} B^0 \\ \overline{B}^0 \end{pmatrix} = \left(M - \frac{i}{2}\Gamma\right)\begin{pmatrix} B^0 \\ \overline{B}^0 \end{pmatrix} \tag{1.24}$$

where the B^0 and $\overline{B}^0$ are the flavour eigenstates. M and Γ are the mass and decay matrices respectively. They are hermitian so

$$M_{12} = M_{21}^*, \quad \text{and} \quad \Gamma_{12} = \Gamma_{21}^*, \tag{1.25}$$

and the validity of the CPT symmetry imposes

$$M_{11} = M_{22}, \quad \text{and} \quad \Gamma_{11} = \Gamma_{21}, \tag{1.26}$$

so that the two states B^0 and $\overline{B}^0$ have same mass and same decay width.

The non zero values of the off-diagonal elements in Eq. (1.25) allow the oscillations between the two states B^0 and $\overline{B}^0$. The Hamiltonian has to be diagonalised to find the eigenstates which are

$$|B^0_{H,L}\rangle = p|B^0\rangle \mp q|\overline{B}^0\rangle \tag{1.27}$$

where $|q|^2 + |p|^2 = 1$ according to the normalization condition. The mass difference Δm_B and the decay width $\Delta\Gamma_B$ between the two above eigenstates are defined as

$$\Delta m_B \equiv M_H - M_L\ , \qquad \Delta\Gamma \equiv \Gamma_H - \Gamma_L \tag{1.28}$$

so that Δm_B is positive by definition. Solving the Schrödinger equation Eq. (1.24) gives the relation between the ratio q/p and the off-diagonal elements M_{12} and Γ_{12}

$$\frac{q}{p} = -\sqrt{\frac{M_{12}^* - i\Gamma_{12}^*/2}{M_{12} - i\Gamma_{12}/2}} \tag{1.29}$$

The time evolution of a B meson initially produced as B^0 or $\overline{B}^0$ is

$$|B^0(t)\rangle = g_+(t)|B^0\rangle + \frac{q}{p}g_-(t)|\overline{B}^0\rangle \tag{1.30}$$
$$|\overline{B}^0(t)\rangle = g_+(t)|\overline{B}^0\rangle + \frac{p}{q}g_-(t)|B^0\rangle$$

where the time dependence is given by

$$g_\pm(t) = \frac{1}{2}\left(e^{-(im_L+\frac{\Gamma_L}{2})t} \pm e^{-(im_H+\frac{\Gamma_H}{2})t}\right), \tag{1.31}$$

and thus the probability for a B meson originally produced as B^0 or $\overline{B}^0$ to be observed in a B^0 or $\overline{B}^0$ state is

$$|\langle B^0|B^0(t)\rangle|^2 = |g_+(t)|^2 \tag{1.32}$$
$$|\langle \overline{B}^0|B^0(t)\rangle|^2 = \left|\frac{q}{p}\right|^2 |g_-(t)|^2 \tag{1.33}$$
$$|\langle B^0|\overline{B}^0(t)\rangle|^2 = \left|\frac{p}{q}\right|^2 |g_-(t)|^2 \tag{1.34}$$
$$|\langle \overline{B}^0|\overline{B}^0(t)\rangle|^2 = |g_+(t)|^2 \tag{1.35}$$
$$\tag{1.36}$$

where

$$|g_\pm(t)|^2 = \frac{e^{-\Gamma t}}{2}\left[\cosh\left(\frac{\Delta\Gamma}{2}t\right) \pm \cos\left(\Delta m t\right)\right]. \tag{1.37}$$

The oscillations are cosinusoidal with a frequency given by the mass difference. The current values for the mass difference in the B^0_d and B^0_s systems are [8]

$$\Delta m_{B^0_d} = (0.507 \pm 0.005)\,\mathrm{ps}^{-1},\ \Delta m_{B^0_s} = (17.77 \pm 0.12)\,\mathrm{ps}^{-1}. \tag{1.38}$$

In order to measure the fast B^0_s oscillations, a good vertex resolution is needed.

1.1.1 The CP violation in the B meson system

CP violation can occur in three ways

- CP violation in decay
- CP violation in mixing
- CP violation in the interference between decays with and without mixing

CP violation in decay. It occurs when the amplitude for a decay and its CP conjugate have different magnitudes.

The amplitudes for a B^0 or $\overline{B}^0$ decaying into a final state f are

$$A_f = \langle f|H|B^0\rangle \quad \text{and} \quad \bar{A}_f = \langle f|H|\overline{B}^0\rangle \tag{1.39}$$

where H is the weak interaction Hamiltonian, and the amplitudes for the decay in the CP-conjugated final state $\overline{f}$ are

$$A_{\overline{f}} = \langle \overline{f}|H|B^0\rangle \quad \text{and} \quad \overline{A}_{\overline{f}} = \langle \overline{f}|H|\overline{B}^0\rangle. \tag{1.40}$$

The decay amplitudes $A_{\overline{f}}$ and $\overline{A}_{\overline{f}}$ can be written as

$$A_f = \sum_i A_i e^{i\delta_i + \phi} \quad \text{and} \quad \overline{A}_{\overline{f}} = \sum_i A_i e^{i\delta_i - \phi} \tag{1.41}$$

where A_i is a real number, equal for both B^0 and $\overline{B}^0$, δ_i is the strong phase that is the same in the B^0 and $\overline{B}^0$ decays because the strong interaction conserves CP, and ϕ_i is the weak phase that changes sign under a CP transformation. When only one amplitude contributes to a decay there is no CP violation because $|A_f| = |\overline{A}_{\overline{f}}|$. Therefore if

$$|A_f|/|\overline{A}_{\overline{f}}| \neq 1 \tag{1.42}$$

there is CP violation in decay, or direct CP violation. It means that the decay rate of a B^0 into a final state f is different from that of a $\overline{B}^0$ into the CP-conjugated final state $\overline{f}$.

CP violation in mixing. It appears in the time evolution of a neutral B meson and its anti-meson described by the Schrödinger equation Eq. (1.24). CP violation arises from a difference in the rates of $B^0 \to \overline{B}^0$ and $\overline{B}^0 \to B^0$ that happens when the magnitudes of the off-diagonal elements in the effective Hamiltonian are different. From Eq. (1.29)

$$\left|\frac{q}{p}\right|^2 = \left|\frac{\left(M_{12}^* - \frac{i}{2}\Gamma_{12}^*\right)}{\left(M_{12} - \frac{i}{2}\Gamma_{12}\right)}\right|. \tag{1.43}$$

When CP is conserved the mass eigenstates are CP eigenstates and the relative phase between M_{12} and Γ_{12} vanishes, so that from

$$|q/p| \neq 1 \tag{1.44}$$

there follows the CP violation in the mixing, or indirect CP violation.

For the neutral B mesons this effect can be observed through the asymmetry in semileptonic decays

$$a_{sl}(t) = \frac{\Gamma(\overline{B}^0(t) \to \ell^+\nu X) - \Gamma\left(B^0(t) \to \ell^-\nu X\right)}{\Gamma(\overline{B}^0(t) \to \ell^+\nu X) + \Gamma\left(B^0(t) \to \ell^-\nu X\right)}\,. \tag{1.45}$$

A non zero value of a_{sl} means that a B^0 or $\overline{B}^0$ oscillated in its antiparticle decaying in the lepton of the "wrong" sign.

CP violation in the interference between decays with and without mixing. A final state f_{CP}, that is a CP eigenstate with eigenvalue $\eta_{f_{CP}}$, is accessible to both B^0 and $\overline{B}^0$ decays. It is useful to introduce the quantity

$$\lambda \equiv \frac{q}{p}\frac{\overline{A}_{f_{CP}}}{A_{f_{CP}}} = \eta_{f_{CP}}\frac{q}{p}\frac{\overline{A}_{\overline{f}_{CP}}}{A_{f_{CP}}}. \tag{1.46}$$

When CP is conserved $|q/p| = 1$ and $|\overline{A}_{\overline{f}_{CP}}|/|A_{f_{CP}}| = 1$, so that

$$\lambda \neq \pm 1 \tag{1.47}$$

implies a violation of the CP symmetry in the interference between decays with and without mixing, or indirect CP violation. It can occur also when there is no CP violation in either decay ($|q/p| = 1$) or mixing ($|\overline{A}_{\overline{f}_{CP}}|/|A_{f_{CP}}| = 1$), being $|\lambda| = 1$ but $\mathrm{Im}\,\lambda \neq 0$.

For the neutral B mesons, indirect CP violation can be observed by comparing at the time $t \neq 0$ the decays into final CP eigenstates of a B meson produced as a B^0 to those of a B produced as a $\overline{B}^0$

$$a_{f_{CP}}(t) = \frac{\Gamma(B^0(t) \to f_{CP}) - \Gamma(\overline{B}^0(t) \to f_{CP})}{\Gamma(B^0(t) \to f_{CP}) + \Gamma(\overline{B}^0(t) \to f_{CP})}. \tag{1.48}$$

1.1.2 CP violation in the decay $B^0_d \to J/\psi \overline{K}^0_S$

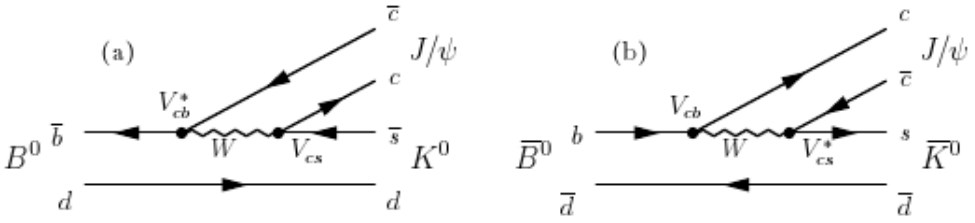

Figure 1.3: Feynman tree diagrams for the decays $B^0 \to J/\psi K^0$ and $\overline{B}^0 \to J/\psi \overline{K}^0$

The $B^0_d \to J/\psi \overline{K}^0_S$ allows the extraction of the angle β of the Unitarity Triangle in Figure 1.1. The time-dependent decay rates of B^0 and $\overline{B}^0$ decaying into a common final state f are

$$\begin{aligned}
\Gamma_{B^0 \to f}(t) &= e^{-\Gamma t}\frac{|A_f|^2}{2}\big[\big(1+|\lambda|^2\big) + \big(1-|\lambda|^2\big)\cos(\Delta m\, t) \\
&\qquad - 2\,\mathrm{Im}(\lambda)\sin(\Delta m\, t)\big] \\
\Gamma_{\overline{B}^0 \to f}(t) &= e^{-\Gamma t}\frac{|A_f|^2}{2|\lambda|^2}\big[\big(1+|\lambda|^2\big) - \big(1-|\lambda|^2\big)\cos(\Delta m\, t) \\
&\qquad + 2\,\mathrm{Im}(\lambda)\sin(\Delta m\, t)\big]\,,
\end{aligned} \tag{1.49}$$

where λ is defined in Eq.(1.46). For the $B^0_d \to J/\psi \overline{K}^0_S$ decay it is

$$\lambda_{J/\psi K^0_S} = \left(\frac{q}{p}\right)_{B_d} \frac{\overline{A}_{J/\psi K^0_S}}{A_{J/\psi K^0_S}} = \left(\frac{q}{p}\right)_{B_d} \frac{\overline{A}_{J/\psi \overline{K}^0}}{A_{J/\psi K^0}} \left(\frac{p}{q}\right)_K \tag{1.50}$$

$$= -\left(\frac{V^*_{tb}V_{td}}{V_{tb}V^*_{td}}\right)\left(\frac{V_{cb}V^*_{cs}}{V^*_{cb}V_{cs}}\right)\left(\frac{V_{cs}V^*_{cd}}{V^*_{cs}V_{cd}}\right) = e^{-2i\beta}\,. \tag{1.51}$$

where the factor $(p/q)_K$ takes into account that the B^0 ($\overline{B}^0$) decays into a K^0 ($\overline{K}^0$) that oscillates to a K^0_S.

The penguin diagrams contributing to this decay are strongly suppressed, and the dominant one has the same weak phase as the tree diagram in Figure 1.3, so that $|\overline{A}_f/A_f|^2 = 1$ with a good accuracy [11]. Since with a good approximation $|q/p| = 1$ [8], also $|\lambda_f| = 1$. Thus, neglecting $\Delta\Gamma$, Eq. (1.49) simplifies to

$$\Gamma_{B^0_d \to J/\psi \overline{K}^0_S}(t) = |A_f|^2 e^{-\Gamma t}\left[1 - \mathrm{Im}(\lambda)\sin(\Delta m\, t)\right] \tag{1.52}$$

$$\Gamma_{\overline{B}^0_d \to J/\psi \overline{K}^0_S}(t) = |A_f|^2 e^{-\Gamma t}\left[1 + \mathrm{Im}(\lambda)\sin(\Delta m\, t)\right] \tag{1.53}$$

and the asymmetry in Eq. (1.48) becomes

$$a_{CP}(t) = \sin 2\beta \sin(\Delta m\, t)\,. \tag{1.54}$$

1.1.3 $B^0_s \to J/\psi\phi$

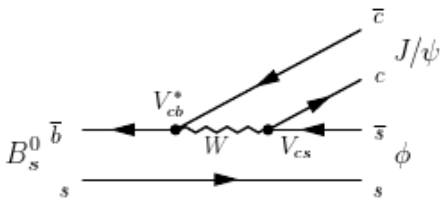

Figure 1.4: Feynman tree diagram for $B \to J/\psi\phi$

The decay $B^0_s \to J/\psi\phi$ is very similar to $B^0_d \to J/\psi \overline{K}^0_S$, from which it differs for the spectator quark that is a s instead of a d. The Feynman

diagram for this decay is shown in Figure 1.4. The parameter λ is

$$\lambda_{J/\psi K_S^0} = \left(\frac{q}{p}\right)_{B_s} \frac{\overline{A}_{J/\psi\phi}}{A_{J/\psi\phi}} \tag{1.55}$$

$$= \left(\frac{V_{tb}^* V_{ts}}{V_{tb} V_{ts}^*}\right)\left(\frac{V_{cb} V_{cs}^*}{V_{cb}^* V_{cs}}\right) \tag{1.56}$$

$$= -e^{-2i\chi} \tag{1.57}$$

where

$$\chi = arg\left(-\frac{V_{cb} V_{cs}^*}{V_{tb} V_{ts}^*}\right) \tag{1.58}$$

is the small angle of the unitarity triangle corresponding to the unitarity relation

$$V_{us} V_{ub}^* + V_{cs} V_{cb}^* + V_{ts} V_{tb}^* = 0 \tag{1.59}$$

of the CKM matrix, Eq. (1.16).

Being a pseudo-scalar that decays into two vector mesons, due to the conservation of the total angular momentum, the observed final state is a superposition of three possible states with relative orbital angular mometum between the vector mesons, ℓ. The CP -eigenvalue of the observed final state depends on ℓ. An angular analysis is then necessary to disentangle the CP -odd and CP -even components.

1.1.4 Rare decay $B_s^0 \to \mu^+\mu^-$

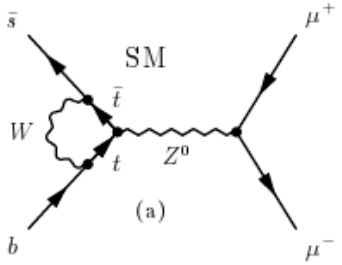

Figure 1.5: One of the Standard Model Feynman diagrams for $B_s^0 \to \mu^+\mu^-$

The $B_s^0 \to \mu^+\mu^-$ has not yet been observed. It is a rare decay in

the Standard Model, with a calculated branching ratio of $\mathcal{O}(10^{-9})$. It is a Flavour Changing Neutral Current (FCNC) process, that in the Standard Model is suppressed by the Glashow Iliopoulos Maiani (GIM) mechanism [12], so that it can not occur at the tree level but the diagrams with at least one loop have to be also considered. These features make this process an interesting probe to physics beyond the Standard Model, given that new particles entering in the loop can enhance considerably the branching ratio. In Figure 1.5 is shown one of the possible one-loop Feynman diagrams describing the $B_s^0 \to \mu^+\mu^-$ decay. In the minimal supersymmetrical extension of the Standard Model, the Minimal Supersymmetric Standard Model (MSSM) [13], with the Minimal Flavour Violation (MFV) hypothesis [14] restraining the CP violating parameters to the CKM matrix of the Standard Model, the branching ratio is proportional to

$$BR(B_s \to \mu^+\mu^-)_{SUSY} \propto \frac{m_b^2 m_\mu^2 \tan^6\beta}{M_{A^0}^4}, \qquad [15] \qquad (1.60)$$

where m_b and m_μ are the masses of the b quark and the muon, respectively, A^0 is one of the Higgs boson of the theory, and $\tan\beta$ is the ratio of the vacuum expectation values of the two Higgs doublets H_u and H_d needed to give mass to the up- and down-type quarks [13]. In principle the branching ratio can be enhanced by a factor of 10^3. The current experimental upper limit, set by Tevatron [16, 17], is larger of a factor of 25, cutting part of the MSSM parameter space.

Chapter 2

The LHCb Experiment

The LHCb experiment is one of the experiments at the Large Hadron Collider (LHC) [18]. Its aim is to perform precise measurements of CP violating quantities in the decays of B mesons and Λ_b hadrons. An hadronic collider has the main advantage to provide a very high statistics[1] and the high energy in the centre of mass reached by LHC enables the observation of effects of New Physics beyond the Standard Model. However, it is a great challenge for the detector to distinguish and select the events of interest in the harsh hadronic environment.

Moreover an accurate separation between kaons and pions is needed to properly reconstruct the hadronic B decay final states such as $B^0 \to \pi^+\pi^-$, $B^0 \to DK^*$ and $B_s^0 \to D^{\pm}K^{\mp}$, which are taken care of by the ring imaging Cherenkov detectors.

To study the time-dependent asymmetries of the CP violation, it is important to have an excellent proper-time resolution. To this, the vertex detector provides a very precise measurements on the position of the production and of the decay vertices.

It is also of crucial importance the tagging of the decaying B meson, for which purpose an accurate tagging using the signal and the acompanying B has been developed.

However, for all these to have some relevance, it is necessary a fast

[1] 10^{12} $b-\bar{b}$ per nominal year of data taking are foreseen, given the nominal luminosity at which LHCb will work 2×10^{32} $\mathrm{cm}^{-2}\mathrm{s}^{-1}$, the energy in the centre of mass is $\sqrt{s} = 14\mathrm{TeV/c}^2$, and the expected b production cross section of $\sigma_{b\bar{b}} = 500\mu\mathrm{b}$

and efficient decision whether the current event is of any interest or it can be discarded. This is the task of the first stage of the trigger system, that starting from the hight LHC rate of 40 MHz is able to select a rate of 1 MHz of relevant events. Its decisions are then confirmed and refined in the two subsequent trigger stages that further reduce the rate down to a value of 2 kHz and make the storage of the selected data and the off-line analysis possible.

Finally the Muon Detector has the task to identify and trigger on muons of high transverse momentum in the first trigger stage, and to subsequently confirm this decision with a stand-alone track reconstruction. It also provides the identification of muons for the off-line reconstruction. Given that muons can be found in the final states of many B decays which are sensitive to CP violation, their correct identification is of great relevance for the LHCb experiment.

In this chapter after a brief description of the Large Hadron Collider, the elements that consitute the LHCb experiment are illustated in details according to the order they are located along the beam pipe from the interaction point on, with the exception of the Muon Detector that is considered in a dedicated chapter.

The LHCb detector is composed by (Figure 2.2)

- the VErtex LOcator (VELO)
- the Tracker Turicensis (TT)
- the first Ring Imaging CHerenkov detector (RICH1)
- the magnet
- the second Ring Imaging CHerenkov detector (RICH2)
- the Tracking stations (T1÷T3)
- the first Muon station (M1)
- the Electromagnetic and Hadronic CALorimeters (ECAL and HCAL), with the Scintillator Pad Detector (SPD) and the Pre-Shower (PS)

- the last four Muon stations (M2÷M5).

The detectors listed above are grouped in systems according to their function. VELO, TT and T stations are part of the *tracking system* that provides the track reconstruction, while the particle identification is provided by RICH detectors, calorimeters and Muon stations. In addition, the first stage of the *trigger system*, the Level-0 (L-0)trigger, receives information from part of the vertex detector, from the calorimeters and from the Muon stations for a first selection of the B decay products.

A sketch of the LHCb functioning

Before considering each detector separately and their grouping in systems, to give an overview of the connection of the detectors, a charged particle produced in a B decay is followed along its trip through the LHCb experiment.

When a B meson is produced, the position of the production vertex is reconstructed by the vertex detector. The B meson travels ~ 1 cm before its decay. A secondary charged particle interacts leaving hits in VELO, TT and T stations. The detectors reconstruct the trajectory and, using the curvature exerted by the magnetic field, determine the electrical charge and the momentum. In RICH1 (in which it is already passed) and in RICH2 the particle emits Cherenkov radiation from which it is possible to measure its velocity and, combining this information with the momentum measured by the tracking system, an estimate of its mass is provided. The mass is used for an accurate separation between kaons and pions. After RICH2 the particle enters the calorimeters where it interacts with the material producing a cascade of secondary particles that are absorbed and used to determine its energy. If the particle is a muon, it passes through the calorimeters and interacts with the Muon detector. If it has momentum greater than ~ 6 GeV/c it reaches the last station (M5) leaving hits in the four previous stations.

At this point the muon component of the L-0 Trigger starts with a quick stand-alone track reconstruction backward, from M5 towards the interaction point. With the information from stations M1 and M2 an

estimate of the track momentum is given. The muon (pair of muons) with transverse momentum (sum of transverse momenta) greater than 1.2 (1.5) GeV/c is selected.

Analogously, the calorimeter L-0 trigger looks for high transverse energy candidates indentifying particles from the energy deposits in ECAL and HCAL together with the information provided by the two additional detectors, Scintillator Pad Detector and PreShower.

Besides, the Pile-Up system, which is part of the VELO detector, vetoes the events if more than one vertex is detected.

After L-0 is the turn of High Level Trigger (HLT) that at its first stage confirms the decision of L-0 and afterwards, with the help of the full event reconstruction, accurately selects the events of interest.

2.1 The Large Hadron Collider

The Large Hadron Collider (LHC) is the new proton-proton collider built at CERN in the tunnel that until 2000 housed the Large Electron Positron collider (LEP). The tunnel has a circumference of 26.7 km and it is located from 45 to 170 m underground. LHC boosts to the final energy of 7 TeV/c^2 protons of 450 GeV/c^2 provided by a chain of preaccelerators (LINear ACcelerator 1, Proton Syncrotron Booster, Proton Syncrotron and Super Proton Syncrotron). Protons travel in opposite directions and collide in the four interaction points IP1, IP2, IP5, and IP8, were the LHC experiments ATLAS (A Toroidal LHC ApparatuS) [19], ALICE (A Large Ion Collider Experiment) [20], CMS (Compact Muon Solenoid) [21] and LHCb (Large Hadron Collider *b*-physics) [22] are located, see Figure 2.1. For the ALICE purposes the LHC is filled in dedicated runs with heavy ions like Pb instead of protons.

At an energy of 7 TeV/c^2, protons require an 8.33 T magnetic field to maintain their orbit. This field is provided by superconducting magnets. As the two proton beams travel in opposite directions through the ring, separate beam pipes with opposite magnetic field directions are needed. They are arranged according to what was called a *two in one solution* [18],

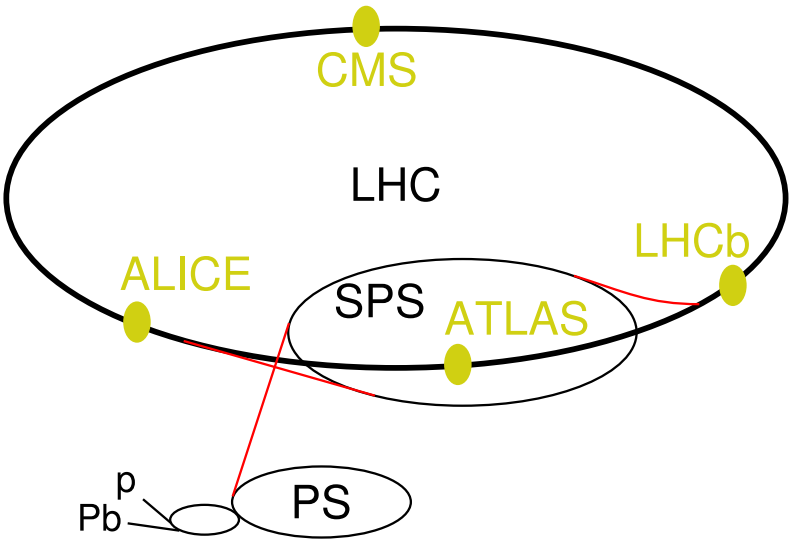

Figure 2.1: The LHC ring with the preaccelerator chain: the linear accelerators (LINAC1 for protons and LINAC3 for Pb ions), the Proton Syncrotron Booster (PSB), the Proton Syncrotron (PS), and the Super Proton Sincrotron (SPS). In yellow are indicated the four main experiments: ATLAS, ALICE, CMS, and LHCb, located at the interaction points IP1, IP2, IP5, and IP8 respectively.

where the magnet coils surrounding the two beam channels are embodied inside the same iron yoke. The whole superconducting magnet is placed inside a cryostat, containing superfluid helium with a temperature of 1.9 K.

Since the time needed for an orbit is 89 μs and the design bunch spacing is 25 ns, as much as 3564 bunches could be carried out in each orbit. In effect, because of the rise times of the SPS and LHC Injection Kicker and of the LHC Dump Kicker, only 2808 non empty bunches can be obtained. The nominal number of protons per bunch is 1.15×10^{11} [18].

2.2 LHCb

The aim of the LHCb experiment is to study the physics regarding the B mesons with high statistics.

The luminosity achieved by the LHC machine is by design $\mathcal{L} = 10^{34}$ cm^{-2} s^{-1}, as required by the high luminosity experiments ATLAS and

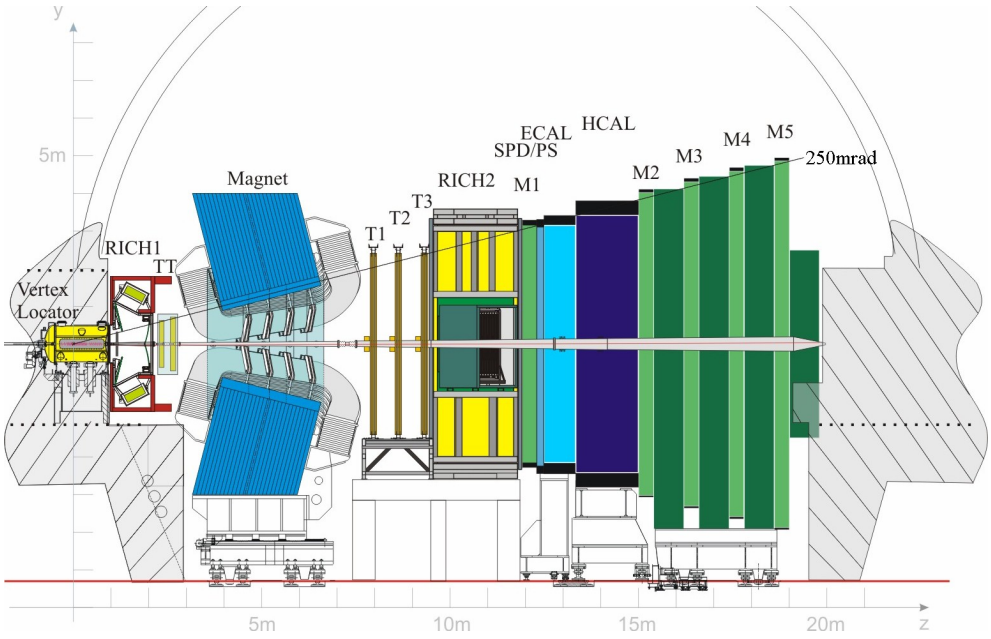

Figure 2.2: Side view of the LHCb detector. The LHCb reference coordinate system is shown.

CMS. This is however too high for LHCb that needs a precise identification of the production and decay vertices of the B mesons. Thus the luminosity can be tuned by changing the beam focus at the LHCb interaction point independently from the others. At a luminosity of $\mathcal{L} = 2 \times 10^{32}$ cm^{-2} s^{-1} the detector occupancy remains low, the radiation damage is reduced and the events are dominated by a single p-p interaction so that the production and decay vertices are easier to indentify. About 10^{12} $b - \bar{b}$ pairs are expected to be produced in one year of data taking (10^7 s) at nominal conditions.

At the high energy in the centre of mass provided by LHC, $\sqrt{s} = 14\text{TeV/c}^2$, the $b - \bar{b}$ pairs are expected to be produced together in forward or backward cone around the beam axis. The adopted geometry for the LHCb detector was that of a single-arm spectrometer with an angular acceptance that covers a range of $10 - 300$ mrad in the horizontal (bending) plane, and $10 - 300$ mrad in the vertical (non-bending) plane. The limits are set by the beam pipe at small angles and by the magnet

at large angles.

In order to discriminate the B decay events among the huge amount of particles produced in $p-p$ collisions the LHCb experiment needs a good vertex and momentum resolution, as well as a proper particle identification. In addition, it has to be provided with efficient trigger system and tagging algorithms.

Thus the LHCb detector, [22], consists of a vertex detector (VELO), a tracking system (VELO, TT, T sations), two Cherenkov detectors, a calorimeter system, and a muon detector.

2.3 VELO

The task of the VELO is to provide a precise measurement of the production and decay vertices of the B mesons. This is crucial in some key measurements, *e.g.* the time dependent analysis of the $B_s^0 - \overline{B}_s^0$ oscillations.

The vertex detector is made by two halves containing 21 modules each. A module consists of two semicircular silicon sensors mounted back to back, measuring the distance from the beam (r-sensor) and the polar angle (ϕ-sensor) of a hit (Figures 2.3 and 2.4). Two additional stations just located upstream the VELO sensors constitute the Pile-Up veto system used in the Level-0 trigger (see 2.9).

During the injection into the LHC machine, the acceleration, and the dump of the beam, the detector is retracted of 30 mm away from the beam line to be protected from radiation. Each half is placed in a box to protect the sensors from the radio frequency (RF) field caused by the beam. To reduce the material crossed by the particles, the side of the boxes facing the beam is made of a thin foil of aluminium (300 μm) and this requires the VELO sensors to be placed in a secondary vacuum. After that a stable beam is obtained the detector has to be placed back in its nominal position at the distance of 8 mm from the beam. This is performed by a motion mechanism with an accuracy of $\mathcal{O}(10\ \mu\text{m})$.

The r sensors have 4×512 circular strips centred on the beam axis to

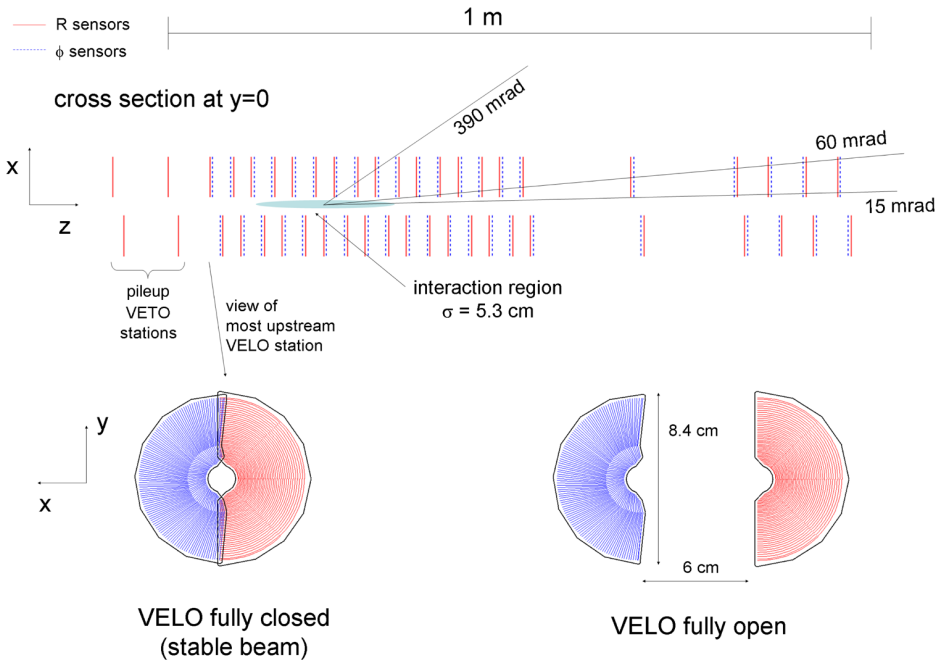

Figure 2.3: Cross section in the (x, z) plane of the VELO silicon sensors, at $y = 0$, with the detector in the fully closed position. The front face of the first modules is also illustrated in both the closed and open positions. The two pile-up veto stations are located upstream of the VELO sensors.

measure the distance r of a track from the beam axis, while the ϕ sensors have 683 radial strips ϕ in the inner region and 1365 radial strips in the outer region to measure the azimuthal angle ϕ. The two half-stations are separated in z by a 1.5 cm gap which allows for an overlap between sensors on the left and on the right of the beam.

With these parameters, the VELO achieves a hit resolution between 5 and 25 μm depending on the track angle and on the strip pitch, which varies between $\sim$ 40 μm and $\sim$ 100 μm from the inner part of the sensors outwards. The resolution of the VELO on the primary vertex is ~ 40 μm in z and ~ 10 μm in x and y, while on the secondary vertex is $100 - 300$ μm, depending on the number of tracks.

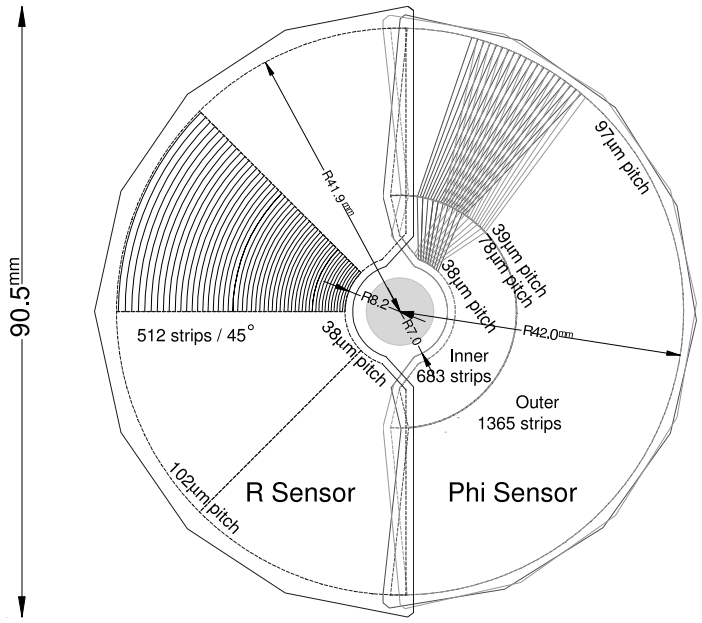

Figure 2.4: Sketch showing the $r\phi$ geometry of the VELO sensors.

2.4 RICH 1 and RICH 2

Particle identification (PID) is a fundamental requirement for LHCb. For the goals of the experiment it is essential to separate pions from kaons in the selected B-hadron decays. To be able to identify K and π particles on a wide range of momenta, from ~ 1 up to 100 GeV/c, LHCb is equipped with two RICH detectors. Both detectors use the Cherenkov effect: when a particle traverses a medium with a speed βc greater than the speed of light c/n in the medium, n being the refractive index of the medium, it emits photons. These Cherenkov photons are emitted with an angle θ_C with respect to the particle trajectory. The Cherenkov angle satisfies the relation:

$$\cos\theta_C = \frac{1}{\beta n} \tag{2.1}$$

which implies that the condition $n\beta \geqslant 1$ must be satisfied to be able to detect the Cherenkov light. This relation is also used to determine the choice of radiator depending on the momentum range to cover.

The RICH1 [22] covers the low momentum range $\sim 1 - 60$ GeV/c

(a) (b)

Figure 2.5: (a) Side view of RIC1 and (b) top view of RICH2.

in the full LHCb angular acceptance (25 mrad to 300 mrad (horizontal) and 250 mrad (vertical)) using silica aerogel ($n = 1.03$) and C_4F_{10} ($n = 1.0014$). The RICH2 [22] instead covers the high momentum region ~ 15 GeV/c up to 100 GeV/c in a limited angular acceptance ($\sim \pm 15$ mrad to ± 120 mrad (horizontal) and ± 100 mrad (vertical)) and uses CF_4 ($n = 1.0005$).

The light cones emitted by the charged particles are projected as ring images by focusing mirrors onto a plane of photodetectors (Figure 2.5). The example of an event in both RICH1 and RICH2 is shown in Figure 2.6. The radius of the ring gives a measure of the opening angle of the corresponding light cone, which in turn gives a value of the particle velocity. By combining this information with the measurement of the particle momentum (obtained from the track curvature in the magnetic field) an estimate of the particle mass is obtained.

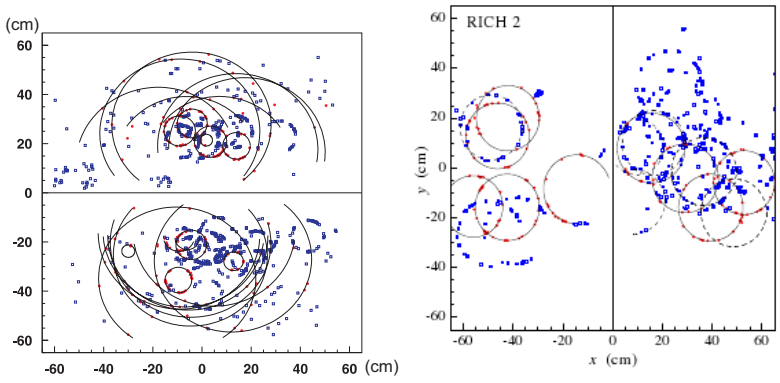

(a) (b)

Figure 2.6: A typical event for both RICH detectors. In the RICH1 (left), the densely populated small diameter rings are related to the gas radiator C_4F_{10} while the more sparsely populated and large diameter rings are from silica aerogel.

2.5 Tracker Turicensis

Located between the RICH1 and the magnet, the Tracker Turicensis (TT) task is to reconstruct the tracks upstream the magnet. The comparison of the tracks reconstructed upstream and downstream the magnet gives the curvature due to the magnetic field and consequently the measurement of the momentum of the particles.

It consists of two stations (TTa and TTb) of silicon strip detectors, separated in z by 27 cm and covering an area of $\sim 130 \times 150$ cm^2 each. In each station two layers are arranged: an x layer with vertical strips and a stereo layer with strips rotated by a stereo angle of $\pm 5°$ (u, v layers). The station TTa is formed by an x layer and a u layer, while the station TTb by a v layer and an x layer. The measurement of the x coordinate of the hit is given by the x layers. The x layers, combined with the two stereo layers, give the measurement on the y coordinate.

The layout of the TTbV and TTbX layers are shown in Figure 2.7. Each layer consists of two 7-sensor ladders lying above and below the beam pipe and eight 14-sensor ladders (seven in TTa) lying on each side of the beam pipe. This gives a total of 896 silicon-strip sensors (420 in TTa and 476 in TTb). The sensors are 500 μm thick, 9.64 cm wide and

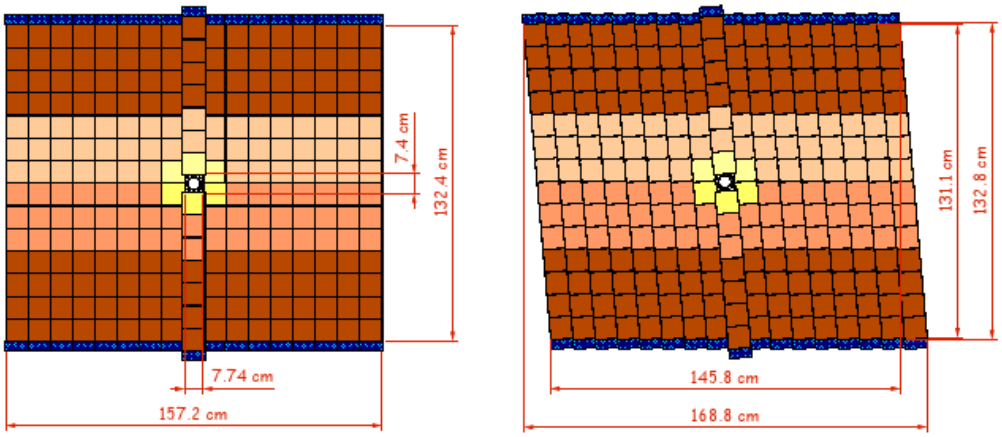

Figure 2.7: Layout of the two silicon-sensor layers of the TTb Station: the vertical X layer on the left and the +5°-tilted stereo layer on the right.

9.44 cm long, and each of them has 512 readout strips with a strip pitch of 183 μm. The spatial resolution on a single hit is about ~ 50 μm.

2.6 T Stations

The T stations are three, located after the magnet at an average distance from the nominal interaction point of 7.75, 8.44, and 9.13 m. They are divided in an Inner and an Outer Tracker because of the occupancy that is bigger close to the beam pipe. Each station is composed by four layers with the same $x-u-v-x$ configuration as the TT. All the three stations have the same dimensions (4.8×5.9 m^2, Figure 2.8), determined by the angular acceptance requirement at the last station. Like the TT, IT uses silicon detectors.

The inner part of each T station consists of four boxes placed above, below, and on the sides of the beam pipe, called top, bottom, A and C boxes.

Each box contains the four $x-u-v-x$ layers and each layer contains seven strips of silicon modules (ladders). The adjacent modules are staggered by 4 mm in z and overlap by 3 mm in x to avoid acceptance

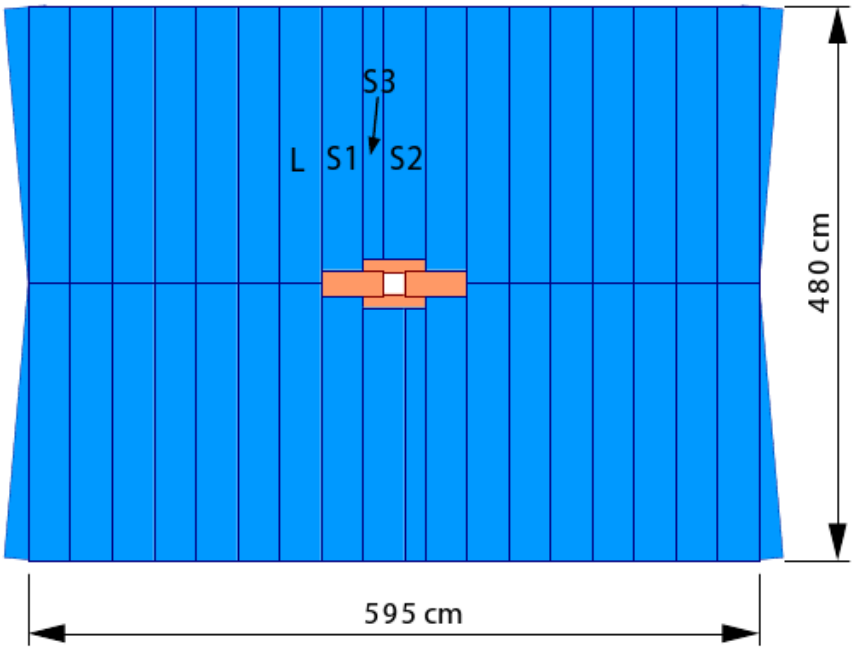

Figure 2.8: Front view of a T station with the modules of the Outer Tracker and the boxes of the Inner Tracker.

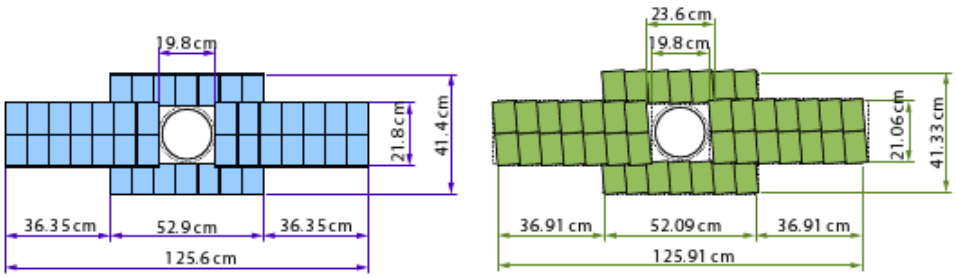

Figure 2.9: Layout of an IT x and u layer with the silicon sensors in the four boxes. In the middle a cross section of the beam pipe is drawn.

gaps. The dimensions and the layout of an IT station are shown in Figure 2.9. The spatial hit resolution provided by each detector module is about 60 μm.

The Outer Tracker occupies the rest of the T station surfaces, with

a small overlap with the IT. Straw tubes constitute the OT detector because of the small flux of particles it receives. Seven long modules (4.8 m) with 256 straw tubes are adjacent to the A and the C IT boxes, while eight short modules (2.3 m) containing 128 tubes are placed on top and bottom of the IT top and bottom boxes.

The straw tubes are filled with 70% Ar and 30% CO_2 to give a fast drift time and a spatial hit resolution of $\sim 200\mu$m .

2.7 Calorimeters

The tasks of the calorimeter system are the identification and selection of hadrons, electrons and photons with high transverse energy, and the measurement of their energies and positions [22]. It is composed by the Scintillating Pad Detector (SPD), the PreShower (PS), the Electromagnetic and the Hadronic CALorimeters (ECAL and HCAL).

In the electromagnetic and hadronic calorimeters layers of scintillator are sandwiched between layers of absorber. The energy of the particles is sampled by collecting photons from showers of secondary particles. To improve both spatial and energy resolution, two additional subsystems are used, namely the Scintillating Pad Detector and the PreShower.

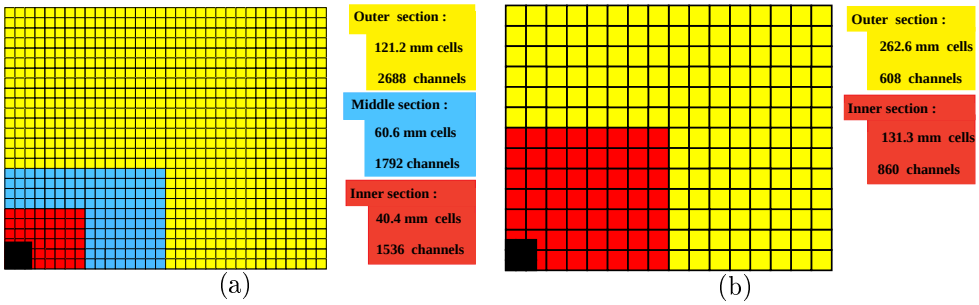

Figure 2.10: Lateral segmentation of the SPD/PS and ECAL and the HCAL. One quarter of the detector front face is shown. (a) the cell dimensions for the SPD/PS and ECAL and (b) for the HCAL.

The charged particles are identified by the SPD since they produce ionisation, as opposite to the neutral particles. The SPD and PS, placed

in front of the main calorimeters, are both 12 mm thick planes of polystyrene scintillating tiles separated by a 15 mm thick lead wall that initiates the electromagnetic showers, discriminating them from the hadronic showers that start later. While SPD is used to separate electrons from photons, the PS is used to separate hadrons from electrons and photons.

The ECAL consists of cell-partitioned 2 mm thick lead and 4mm thick scintillator pads in order to measure the electromagnetic showers of electrons and photons with a resolution [22]

$$\frac{\sigma_E}{E} = \frac{10\%}{\sqrt{E(\mathrm{GeV})}} \oplus 1.0\% \,. \tag{2.2}$$

The HCAL is similar to the ECAL in design, and consists of 16 mm-thick iron sheets, interspersed with ~ 4 mm-thick scintillator regions. It measures the energy of the hadrons with a resolution [22]

$$\frac{\sigma_E}{E} = \frac{80\%}{\sqrt{E(\mathrm{GeV})}} \oplus 10\% \,. \tag{2.3}$$

Almost all hadrons interact with the HCAL, while muons continue traversing it and reaching the muon chambers.

The PS/SPD, ECAL and HCAL adopt a variable lateral segmentation, shown in Figure 2.10, since the hit density varies by two orders of magnitude over the calorimeter surface. A segmentation into three different sections has been chosen for the ECAL and projectively for the SPD/PS. Given the dimensions of the hadronic showers, the HCAL is segmented into two zones with larger cell sizes.

2.8 Tracking System

The tracking system, [22], groups VELO, TT, IT and OT. The task of the tracking system is to reconstruct the trajectories of charged particles that traverse the detector from the production vertex.

The VELO is used for the reconstruction of primary and secondary vertices, whereas the TT, IT and OT are used in the track reconstruction

to determine momenta of charged particles, with a resolution $\delta p/p \sim 0.4\%$.

2.9 Trigger System

The trigger system is composed by two levels, the Level-0 (L-0) and the High Level Trigger (HLT). Its task is to reduce the bunch crossing rate of 40 MHz down to a value of 2kHz, so that data can be stored for the off-line analysis.

L-0 is an hardware trigger that combines the information provided by the VELO, the Calorimeters and the Muon System, to decide whether an event is interesting or not, reducing in this way the data rate to 1 MHz, which is the maximum capability of readout frequency.

HLT at the contrary consists of a C++ application running on the dedicated Event Filter Farm [22], used to further reduce the data rate from 1 MHz a 2 kHz.

The Level-0 trigger is subdivided into three components: the Pile-Up system, the L-0 calorimeter trigger and the L-0 muon trigger. Each component is connected to one detector and to the Level-0 Decision Unit (DU) which collects all information calculated by the trigger systems to evaluate the final decision.

The Pile-Up system is needed to distinguish between crossings with single and multiple visible interactions. It uses four silicon sensors of the same type as those used in the VELO to measure the radial position of tracks. The Pile-Up system provides the position of the primary vertex candidates along the beam-line and a measure of the total backward charged track multiplicity.

The L-0 Calorimeter Trigger system looks for high E_T particles: electrons, photons or hadrons. It forms clusters by adding the E_T of 2×2 cells and selecting the clusters with the largest E_T. Clusters are identified as electron, γ or hadron based on the information from the components of the Calorimeter system .

The L-0 Muon Trigger is based on a stand-alone reconstruction of

muons with a momentum resolution of $\sim 20\%$. Track finding is performed by processing elements which combine data from the five muon stations to form towers pointing towards the interaction region. The Level-0 muon Trigger selects up two muons with the highest p_T for each quadrant of the Muon Detector.

The High Level Trigger is divided in two sublevels, HLT1 and HLT2. HLT1 refines the L-0 decisions performing a partial reconstruction of the event applying sequences of algorithms (*alleys*) dependent on the L-0 decisions. The L-0 candidates are confirmed or discarded by adding information from a tracking subdetector and applying requirements on the transverse momentum and impact parameter with respect to the primary vertex. This step is called *Level 0 confirmation*, and reduces the data rate from 1 MHz to 40 kHz.

Subsequently the HLT2 performs a full reconstruction of the events and applies selections, so reducing the rate to 2 kHz. Two final selections are applied: inclusive and exclusive. The inclusive selections are used for triggering several signals and control channels. The exclusive selections, where a particular B decay channel is reconstructed, are specifically designed to provide the highest possible efficiency for the specific B decay channels of interest.

Chapter 3

The Muon Detector

Since a relevant fraction (3%) of the B meson decays contain muons in the final state, the Muon Detector is important for the identification and reconstruction of muons.

In particular two muons are present in the final state of the two *gold plated* B meson decays $B_d^0 \to J/\psi(\mu^+\mu^-)K_S$ and $B_s^0 \to J/\psi(\mu^+\mu^-)\phi$, from which the angle β of the Unitarity Triangle can be extracted. Furthermore, the charge of muons coming from semi-leptonic B decays is used to tag the initial state flavour of the accompanying neutral B mesons. Moreover muons are present in the rare decay $B_s^0 \to \mu^+\mu^-$, that has never been measured before, and it is a good probe for an indirect detection of effects of new physics.

Hence an efficient muon triggering and particle identification are fundamental requirements for the LHCb experiment.

Muons with high transverse momentum (p_T) are a typical signature of a B meson decay, and the Muon System exploits this feature both for muon trigger and for reconstruction algorithms.

3.1 Detector Structure

Since muons are the most penetrating particles, the Muon Detector is located downstream along the beam axis as the last detector of the LHCb experiment. It consists of five stations (M1÷M5) the first of

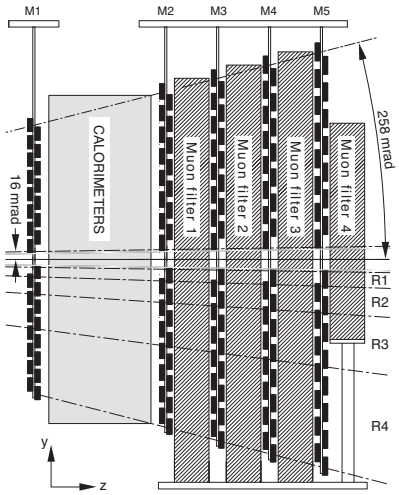

Figure 3.1: Side view of the Muon system.

which is situated in front of the calorimeter preshower, at 12.1 m from the interaction point. The other four stations lie behind the hadronic calorimeter with a distance of 1.2 m from each other and are interleaved with 80 cm thick filters consisting of iron blocks (Figure 3.1).

The filters have the task to absorb hadrons, electrons and photons, so that only penetrating muons can reach the last muon station. Thus, to reduce mis-identifications, only particles that traverse all the five stations are identified as a muons. The minimum momentum needed by a muon to reach station M5 is ~ 5 GeV/c.

The geometry of the detector is projective with respect to the interaction point to mantain the angular acceptance of the experiment, 250 (300) mrad in the bending (non bending) plane. In addition, since the particle rate is more intense in the area around the beam pipe, the stations are divided in four concentric rectangular regions (R1$\div$R4) with size increasing according to the ratio $1 : 2 : 4 : 8$ to roughly have the same acceptance. The dimensions of the readout elements (*pads*) are set such that the occupancy is approximately constant. As a consequence the chambers, segmented in pads, have different sizes according to the region and station to which they belong (Figure 3.2).

The detector technology chosen for the Muon stations is the Multi

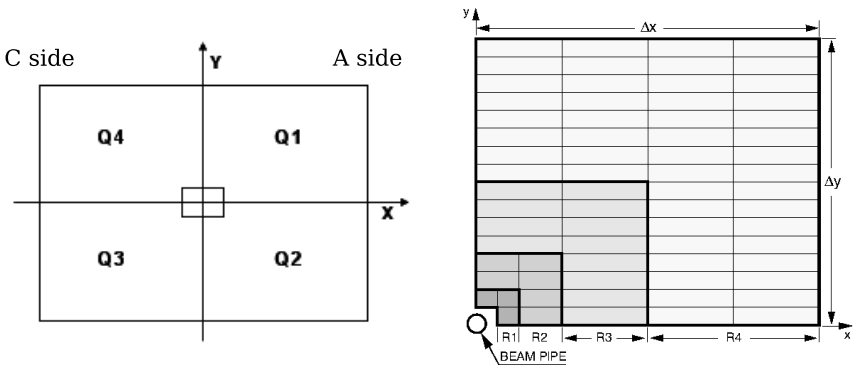

(a) (b)

Figure 3.2: (a) The Muon System quadrants as seen from the interaction point, and (b) front view of one quadrant of a Muon station showing the different regions. Each rectangle represents one chamber.

Wire Proportional Chamber (MWPC). However, in the inner part of the first station Gas Electron Multiplier (GEM) detectors were preferred because of their better ageing properties under intense radiation. In Table 3.1 it is reported the particle rate calculated for each region and station, including a safety factor of two for station M1 and of five for the others. There are 1368 MWPC's and 12 GEM's, for a total of 1380

	M1	M2	M3	M4	M5
R1	460	37.5	10	6.5	4.4
R2	186	26.5	3.3	2.2	1.8
R3	80	6.5	1.0	750×10^{-3}	650×10^{-3}
R4	25	1.2	415×10^{-3}	250×10^{-3}	225×10^{-3}

Table 3.1: Particle rates (kHz/cm^2) in the muon system calculated at a luminosity of $\mathcal{L} = 5 \times 10^{32}$ cm^{-2} s^{-1}

chambers. In stations M2÷M5 the MWPC's are composed of four gas gaps filled with a gas mixture of $Ar/CO_2/CF_4$ in the proportion of 40 : 55 : 5, and arranged in two sensitive layers with independent readout. In station M1 the chambers have only two gas gaps to minimize the material in front of the electromagnetic calorimeter [22]. Each of the 12 GEM chambers consists of two triple-GEM detectors superimposed and

forming two sensitive layers. The gaps are filled with the gas mixture $Ar/CO_2/CF_4$ in the proportion of $45:15:40$ [24].

To provide a complete geometrical acceptance to the particles originated in the interaction point the chambers are mounted on supporting walls at four different positions in z ($z_{2,3} = \pm 6$ mm and $z_{1,4} = \pm 14$ mm) (Figure 3.3(a)). Chambers in the same row are alternately placed at two different z, while chambers in the same column are all located at the same distance from the supporting walls (Figure 3.3(b)-(c)). In addition the chambers are symmetrically placed on both sides of a wall, z_1 and z_2 in front and z_3 and z_4 behind the walls, as shown in Figure 3.3(a). This peculiar arrangement was devised to safe the walls from deformations that could occur if asymmetrically loaded.

Besides, the muon stations, including the iron filters, are separated into two halves which can move on rails away from the beam pipe for maintenance and installation. The two halves are labelled side A(ccess) and C(ooling). In the LHCb system of coordinates the A side is placed in the positive half of the x axis, while the C side at negative x, see Figure 3.2(a).

3.2 The readout

All the chambers are segmented into *physical pads* with different readout depending on their position in the detector. The GEM's have anode readout, while the MWPC's have both anode wire and cathode readout. Each physical pad is read out by a Front-End (FE) channel.

The readout of the binary signal is carried out on logical units, *logical pads*. These devices allow to reach a compromise between spatial resolution and the number of readout channels. To keep noise and dead-time under a reasonable level, the physical pad dimensions need to be underdimensioned with respect to the required spatial resolution. In this case up to four physical pads are combined in OR in the FE boards, building a logical pad.

In the innermost regions (R1 and R2) of stations M2 and M3, where

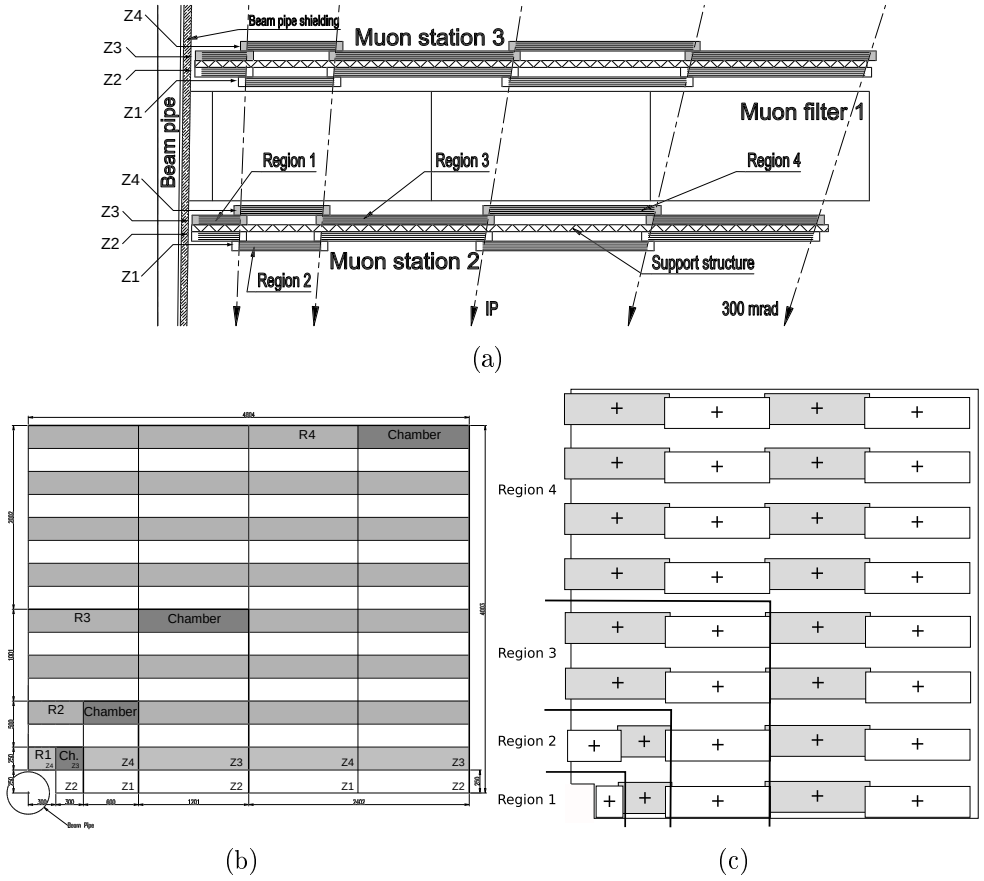

Figure 3.3: (a) Top view of a half of M2 and M3 stations, the chamber setup with respect to the supporting walls is shown.. Front view of quadrant Q1 of station M2, (b) the rows of chambers marked in a darker shade are in positions $z_{3,4}$ behind the support structure, those not marked are in $z_{1,2}$ in front of the support structure; (c) in grey is highlighted the column of chambers located closer to the support wall. The chamber of the same column are placed at the same distance from the wall.

high spatial resolution is needed, logical pads with the required dimensions can not be practically built. In these regions a mixed readout has been adopted: anode wires are grouped into vertical strips to measure the x coordinate of the particle trajectory, while the granularity of the horizontal cathode pads provide the y coordinate. The coincidence of wire and cathode pads give the logical pads.

The size of the logical pads in different regions and stations, and their readout is summarized in Table 3.2. Figure 3.6 shows a quadrant of a

station with the sizes of chambers belonging to different regions and the division into logical pads of four chambers belonging to the four regions of station M1.

	Logical Pad	M1	M2	M3	M4	M5
R1	Size	10×25	6.3×31.1	6.7×33.7	29×36	31×39
	Readout	Anode	Mixed	Mixed	Cathode	Cathode
R2	Size	20×50	12.5×62.5	13.5×67.5	58×72	62×77
	Readout	Anode	Mixed	Mixed	Cathode	Cathode
R3	Size	40×100	25×125	27×135	116×145	124×155
	Readout	Cathode	Cathode	Cathode	Cathode	Cathode
R4	Size	80×200	50×250	54×270	231×290	248×309
	Readout	Anode	Anode	Anode	Anode	Anode

Table 3.2: The readout methods and the logical pad dimensions ($x \times y$, in mm^2) used in the muon chambers.

To reduce the readout channels, horizontal and vertical strips of logical pads are grouped in *OR* into *logical channels* in the whole M2 and M3 stations, and in regions R2÷R4 of stations M4 and M5. The logical pads are then reconstructed by the combination of two crossing strips. In effect the strip readout is not possible in the whole M1 station because of the high rate of particles, while in regions R1 of stations M4 and M5 the reduction in logical channels would be insignificant.

Thus, the total of $122,112$ physical channels is then reduced into $25,920$ logical channels which are combined to obtain $55,296$ logical pads.

For the L-0 trigger processing, the Muon System is subdivided into 192 towers pointing towards the interaction point, as shown in Figure 3.4. Each tower collects the signals of groups of logical pads across the five stations: 8 pads in M1, 96 in M2, 96 in M3, 24 in M4 and 24 in M5 are connected to a Processing Unit (PU). At every bunch crossing, each PU runs 96 track finding algorithms in parallel, one for each pad of M3 in the tower. For each logical pad hit in M3 the straight line passing through the hit and the interaction point is extrapolated to M2, M4 and M5. In these stations hits are looked for within search windows, called Field Of

Interest (FOI), centered on the extrapolated straight line. When at least one hit is found inside the FOI in each station, a muon track is flagged. The position of the track in station M1 is determined extrapolating a straight line from M3 and M2, and searching in the M1 FOI the pad hit closest to the extrapolation point, [23]. Among the 96 candidates that can be found, one per M3 pad of the tower, the two candidates closest to the beam are selected. Their transverse momentum p_T is determined from the track hits in M1 and M2. The track finding is run on each quadrant of the muon system independently. Therefore, the two muon tracks of highest p_T are selected for each quadrant and the information for up to eight selected tracks is transmitted to the L-0 decision unit.

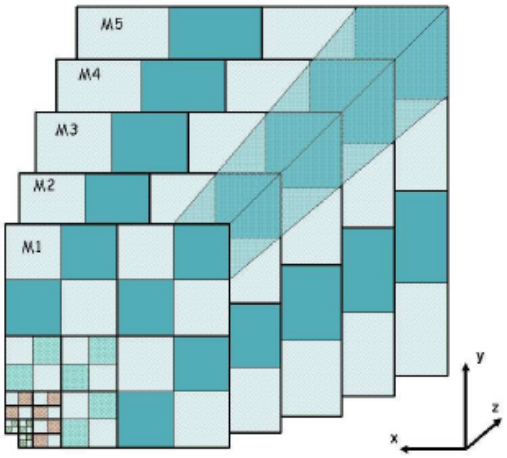

Figure 3.4: A quadrant of the Muon System showing the towers layout.

3.3 Hardware alignment

During the installation, chambers and support walls of the stations M2÷M5[1] were placed in the nominal position within a precision of 1 mm.

[1]station M1 was not installed in the meantime of M2÷M5, but during the 2009 shutdown

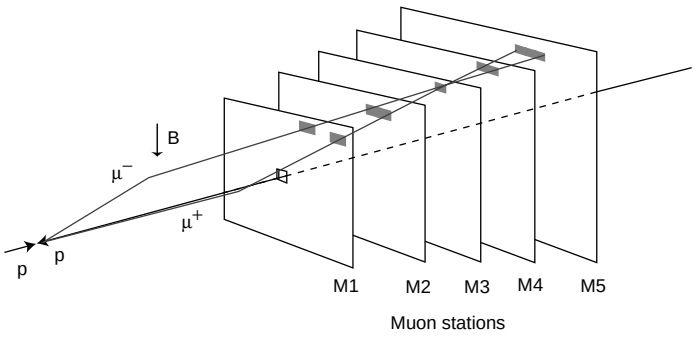

Figure 3.5: Track finding in the L-0 muon trigger.

Afterwords, in a survey measurements campaign, the actual position of the half-stations was determined within a precision of 10 μm.

To detect possible rotations of the supporting walls, the vertical position of half-stations was checked with a plumb line along the innermost edge, and the horizontal position of the top edge with the water level in a pipe. Besides, the wall bending in the horizontal plane on top and bottom edges of the stations, and the position and shape of the beam pipe cut were checked. To ensure a good closure of walls the innermost edges need to be vertical and the beam pipe cuts need to have the right shape and dimensions.

For the x alignment of the chambers reference bars were set on the top edge of the walls at the nominal x position of the chambers in each of the four columns. Then the x position of the chambers was checked with a plumb line. The y alignment was performed by measuring the distance between the centre of the chambers and the reference bars on top of the wall, after a preliminary check on the horizontal positions performed with water level. An example of alignment is shown in Figure 3.7.

The procedure adopted for the x alignment of the chambers could not be used for the more internal chambers, while their y position was still determined by measuring the distance between the centre of the chambers and the reference bars on top of the walls. Even with a complete opening of the supporting walls, the inner edges are still unaccessible

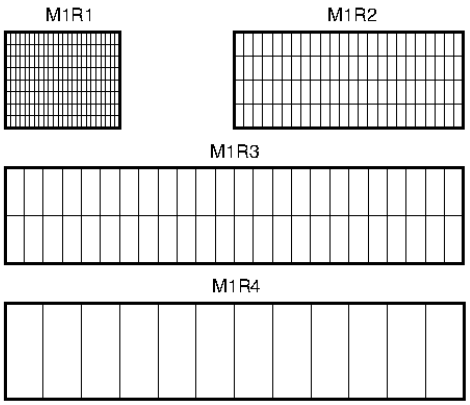

Figure 3.6: The division into logical pads of four chambers belonging to the four regions of station M1. Chamber and pad dimensions scale by a factor of 2 from one region to the next. The scale factor is ~ 1 in y going from M1 to M5 and the ratio between the x dimensions is 2:1:1:4:4 going from M1 to M5.

because of the filters, and the centres of the chambers belonging to R1 and the innermost column of R2 are not visible. In addition, there is no suitable place where to put a reference bar on top of the walls between the reference point A and B of Figure 3.7 (a). For these reasons the x position of the chambers in the outermost column of R2 was determined measuring their distance with respect to the plumb line of the column A, while the innermost chambers (R1 and the innermost column of R2) were aligned measuring the overlaps with the neighbour chambers.

The hardware alignment gives a precision of 1 mm on the position of the chambers.

After opening and closing the position of the half-stations was measured and found reproducible within a precision of 1 mm.

Since the filters can not be completely closed around the beam pipe due to technical problems, the stations are placed as distant as the filters from the beam axis to protect the chambers from an excess of radiation. Each half of M2 and M3 stations is placed at 9 mm from the beam axis, and each half of M4 and M5 at 10 mm. The survey measurements of the half-stations M2-M5 listed in Table 3.3 give the actual position of the

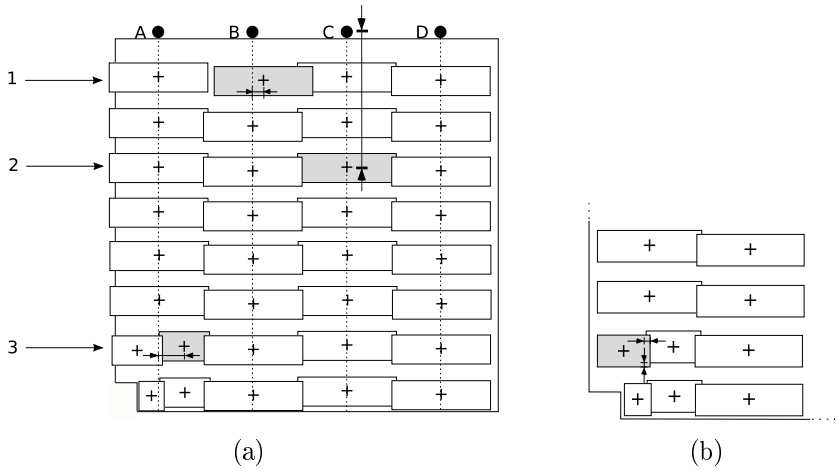

Figure 3.7: Hardware alignment of chambers in a quadrant of station. Only the chambers on one side of the wall are drawn. (a) on top of the walls there are the reference bars. Dashed lines represent the plumb lines used to check the x position of the chambers with respect to the reference bars. Three examples of alignment of chambers (in grey) are indicated with the numbers: (1) the x alignment is performed measuring the distance between the centre of the chamber and the plumb line. (2) the y alignment is performed measuring the distance between the centre of the chamber and the reference bar on top of the support wall. (3) the x alignment of one of the outermost R2 chambers is performed measuring the distance between the centre of the chamber and the plumb line of column A. (b) zoom on the chambers of regions R1, R2 and R3. The alignment of a R2 chamber (in grey) is shown. To align the innermost chambers of regions R2 and those of regions R1 the overlaps with the neighbour chambers are measured.

centres of the half-stations expressed in its own local frame of reference: for the C side half-stations the right handed local frame of reference has the z axis perpendicular to the surface pointing upstream and the x axis antiparallel to the LHCb one, while for the A side half-stations the x axis is parallel to the LHCb one and the z axis points downstream, as shown in Figure 3.8.

All the information related to the actual position of the elements of the detectors are stored in databases that are retrieved by the software reconstruction, so that the actual position of a hit can be determined. Therefore, to have unbiased reconstruction the information about the position of the detector elements in the database need to be as close as possible to their real positions. This can be achieved by an accurate

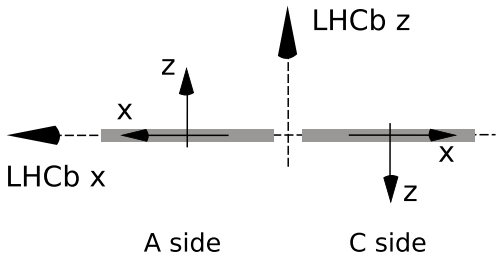

Figure 3.8: The local half-station systems of reference in the LHCb system of reference.

	Tx (mm)	Ty (mm)	Tz (mm)	Rx, Ry, Rz (mrad)
M2 A	$+9 \pm 1$	0 ± 1	-10 ± 1	0.0 ± 0.5
M2 C	$+9 \pm 1$	0 ± 1	$+11 \pm 1$	0.0 ± 0.5
M3 A	$+9 \pm 1$	0 ± 1	-3 ± 1	0.0 ± 0.5
M3 C	$+9 \pm 1$	0 ± 1	$+7 \pm 1$	0.0 ± 0.5
M4 A	$+10 \pm 1$	0 ± 1	-10 ± 1	0.0 ± 0.5
M4 C	$+10 \pm 1$	0 ± 1	$+14 \pm 1$	0.0 ± 0.5
M5 A	$+10 \pm 1$	0 ± 1	-7 ± 1	0.0 ± 0.5
M5 C	$+10 \pm 1$	0 ± 1	$+2 \pm 1$	0.0 ± 0.5

Table 3.3: List of the survey measurements for the half-stations M2-M5 with respect to their nominal positions. With $Tx(Ty, Tz)$ are indicated translations along the $x(y, z)$ axis and with $Rx(Ry, Rz)$ rotations around the $x(y, z)$ axis. The measurements are given in each half-station local system of reference, as indicated in Figure 3.8. The support walls are opened by $9-10$ mm and placed closer to the interaction point with respect to the nominal position. The rotations around the axes are found negligible.

alignment of the detector, by means of the alignment of its elements. In the case of the Muon Detector the elements independently alignable are the single chambers, the half-stations and the whole system.

Chapter 4

Alignment

To achieve their goals, the LHCb detectors must be aligned with great precision[1]. In spite of the accuracy in the construction, during the installation and in the survey, some unpredictable movements of the detectors may occur. In addition some deformations may happen with the passing of time. For these reasons a software tool to align detectors with high precision is of great importance. Besides it can be used when the experiment is operational and survey measurements are no longer possible due to several reasons, such as the high radiation environment and the inaccessibility of certain parts of the detector.

Mis-alignments are in any case expected in parts of the system once operational. For instance the tracking system is subject to a non zero magnetic field which can slightly move the supporting structures. In addition the magnetic field polarity is planned to be periodically inverted for cross checking possible asymmetries of charge. At each refill of the beam the VELO has to be moved away from the beam pipe and realigned, although for this purpose it is equipped with a motion system of high precision. The resolution requirements of the Muon System are not as stringent as for the other detectors since it is mainly devoted to trigger and particle identification and the tracking performance is intrinsically poor. However it has the duty to select muons in the trigger, thus the importance of its alignment can not be underestimated.

[1]The requirements on the alignment precision depend on the task of each detector

The goal of the software alignment procedure is to evaluate the positions of all the alignable elements inside a system of reference valid for the whole experiment. Being the most precise detector and the closest to the interaction point, the global system of reference is based on the VELO.

The software alignment can be carried out with tracks traversing all the detectors of the experiment (global alignment). It can be also achieved by a two step procedure, if the relative positions of the components of each detector are first established (local alignment) and then the position of the detector in the global system of reference is determined.

A local alignment was carried out for the Muon System alignment with cosmic rays. The data analysed were taken during the detector commissioning of Fall 2008. VELO, TT and IT, due to their small surfaces and angular acceptance did not participate in the data taking, while OT joined only for a short period. In spite of the scarce data collected by OT, a preliminary study for a relative alignment between the Muon Detector and OT could be carried out. The results of this study will be discussed in the following chapters while here the theoretical aspects of the alignment methods adopted for the Muon Detector are presented.

Several approaches exist to the problem of the detector alignment and all are based on the minimisation of the residuals between the measured hit positions and the predicted hit positions at the intercept of the tracks with the detector planes. The strategy here adopted is mainly based on the *Kalman filter fit* [25], a least-squares fit method which is the default track fit in the LHCb reconstruction. The Kalman filter fit method was chosen for the Muon Detector alignment because of the "natural" way in which it includes the process noise, like the multiple scattering.

The Kalman filter fit method runs in an alignment framework where C++ code is configured via python scripts. The framework accesses the detector elements in the LHCb databases, so that the alignment constants can be easly updated. It is a general framework and can align any detector whose hits are on a track, *i.e.* for which a measurement function h exists in the LHCb track model. However, for the Muon

Detector some small adjustments were necessary. In the track selection some specific requirements suitable for the tracks reconstructed in the Muon Detector were added to the general default requirements. They are specified in the Chapters where the results on the alignment are discussed.

In addition to the Kalman filter fit method, the local alignment was also performed with the Histogram Based method, specifically developed for the Muon Detector, as planned [31].

4.1 The track format in LHCb

Once a track has been found, it needs to be fitted in order to determine the most precise estimate of the track parameters. These parameters are then used to match the tracks with hits in the Particle Identification systems, locate the origin and decay vertices and calculate invariant masses in physics analyses. The track fit is also the first stage for the software alignment of the detectors.

In the LHCb software a track is described by a set of *states*, where each of them is a five component vector $\overrightarrow{x}$, and a 5×5 covariance matrix C[2], [26]. Given the geometry of the detector, the track states are parametrised as a function of z. The state vectors are defined, at a given z, by the x and y positions, the track slopes and the particle momentum

$$\overrightarrow{x} = \begin{pmatrix} x \\ y \\ t_x \\ t_y \\ q/p \end{pmatrix} \tag{4.1}$$

where $t_x = dx/dz$ and $t_y = dy/dz$ are the slopes in the (x, z) and (y, z) planes, q is the signed charge and p is the momentum of the particle, obtained through the track curvature due to the magnetic field. The

[2]The covariance matrix has variances in its diagonal and covariances in its off-diagonal elements.

location of the track states can be chosen anywhere along the trajectory, however in the track fit it is useful to determine the states at the measurement planes.

4.2 Kalman filter fit

The Kalman filter is the default track fit method in the LHCb software and also used in the alignment method. Using the same method in the track fitting and in the alignment of the detectors has some advantages. It allows to determine the tracks making use of the same track model of the track reconstruction, and to properly account for the multiple scattering, the magnetic field and the energy loss corrections. In addition it may profit from any improvement in the track model or track reconstruction software.

This fit procedure developped in 1960 by R.E.Kalman [29], is used in many different fields, from the navigation systems to the meteorology, and it is now common for the high energy physics experiments.

The principle of this fitting method is to add the measurements one by one to the track fit, each time updating the current track state with the new entry. It is based on the minimisation of the χ^2 of a single measurement on the track. In addition it allows to include process noise, such as the multiple scattering, in an easy way.

The Kalman filter fit procedure works in three steps:

1. in the *prediction* phase a track state is predicted on the basis of the previous track states.

2. In the *filter* step the predicted state is updated with the current measurement through the filter equations. The prediction and filter steps are repeated until all the measurements are added to the fit. After the filter step the track state is the best estimate of the track trajectory based on all the measurements previously added.

3. After all the measurements have been added to the track, the *smoothing* procedure, running in the reverse direction, updates all

the track states with the information from all the measurements.

The first two steps are represented in Figure 4.1.

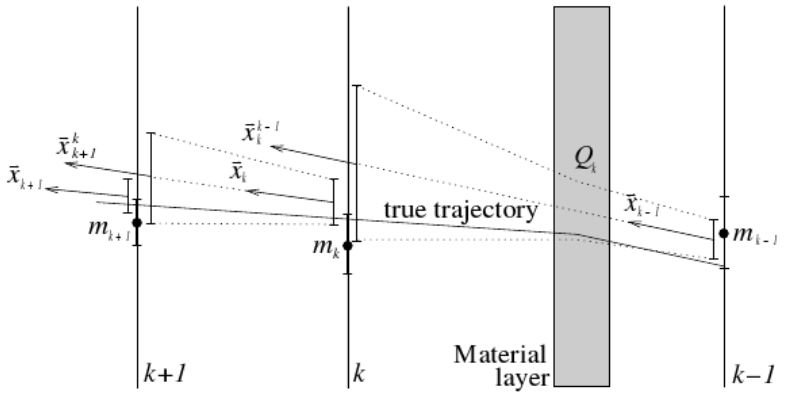

Figure 4.1: Schematic picture of the Kalman filter, showing the prediction and the filter steps. The predicted state $\overrightarrow{x}_k^{k-1}$ is updated in the filter step with the current measurement m_k.

Prediction The propagation relation, that determines the prediction for the next state vector with its covariance matrix, starting from the current state with its covariance matrix, is

$$\overrightarrow{x}_k^{k-1} = f_k(\overrightarrow{x}_{k-1}) + \overrightarrow{w}_k \tag{4.2}$$

$$C_k^{k-1} = F_k C_{k-1} F_k^T + Q_k \tag{4.3}$$

where the superscript $k-1$ indicates the number of measurements that have been already added to the fit when the prediction for the state k is made, so that $\overrightarrow{x}_k^{k-1}$ is the prediction for the state k having considered $k-1$ measurements. The state with no superscript is an already filtered state.

In Eq. (4.2), f_k is the so-called track propagation function, which describes the extrapolation of a state x_k from the previous one, x_{k-1}. For a straight line extrapolation f_k is

$$f_k(\overrightarrow{x}_{k-1}) = F_k \overrightarrow{x}_{k-1} \tag{4.4}$$

where the so-called transport matrix F_k is

$$F_k = \begin{pmatrix} 1 & 0 & \Delta z & 0 & 0 \\ 0 & 1 & 0 & \Delta z & 0 \\ 0 & 0 & 1 & 0 & 0 \\ 0 & 0 & 0 & 1 & 0 \\ 0 & 0 & 0 & 0 & 1 \end{pmatrix} \tag{4.5}$$

and $\Delta z = z_k - z_{k-1}$. $\overrightarrow{w}_k$ is the process noise as result of multiple scattering, for instance, and the matrix Q_k in Eq. (4.3) is the contribution of the process noise to the covariance matrix C.

At the beginning of the track fit an estimate for the initial state $\overrightarrow{x}_0$ is needed in order to make the first prediction. The initial estimate of the covariance matrix C_0 needs to have increased values for the errors on the diagonal, to avoid any bias from the estimate of $\overrightarrow{x}_0$. These informations can be roughly estimated by the track finding algorithms.

The residual is the distance between the measurement and the vector state projected on the measurement. From the predicted state of Eq.(4.2) the predicted residual and its covariance matrix are

$$r_k^{k-1} = m_k - h_k(\overrightarrow{x}_k^{k-1}) \tag{4.6}$$

$$R_k^{k-1} = V_k + H_k C_k^{k-1} H_k^T \tag{4.7}$$

where H_k is the measurement matrix and V_k is the meaurement variance. If a detector directly measures the x coordinates, for example, h_k simplifies to

$$h_k(\overrightarrow{x}_k) = H_k \overrightarrow{x}_k \tag{4.8}$$

where the measurement matrix is given by

$$H_k = (1 \quad 0 \quad 0 \quad 0 \quad 0) \; . \tag{4.9}$$

The contribution of this measurement to the total χ^2 is

$$\left(\chi_+^2\right)_k^{k-1} = r_k^{k-1} \left(R_k^{k-1}\right)^{-1} r_k^{k-1} \, . \tag{4.10}$$

The task of the Kalman fit is to find the optimal track states that yield a minimal χ^2_+.

Filter In the filter step the information of the current measurement k is added to the state predicted on the basis of the first $k-1$ measurements in the track. The filtered state vector and its covariance matrix are given by the filter equation:

$$\overrightarrow{x}_k = \overrightarrow{x}_k^{k-1} + K_k r_k^{k-1} \tag{4.11}$$

$$C_k = (\hat{1} - K_k H_k) C_k^{k-1} \tag{4.12}$$

where K_k is a 5×1 gain matrix given by

$$K_k = C_k^{k-1} H_k^T (V_k + H_k C_k^{k-1} H_k^T)^{-1} = C_k^{k-1} H_k^T (R_k^{k-1})^{-1} \tag{4.13}$$

The complete derivation of this Kalman gain matrix is given in [30]. The filtered residual and its covariance matrix become

$$r_k = m_k - h_k(\overrightarrow{x}_k^{k-1}) = (1 - H_k K_k) r_k^{k-1} \tag{4.14}$$

$$R_k = (1 - H_k K_k) V_k = V_k - H_k C_k H_k^T \tag{4.15}$$

The contribution of this measurement to the total χ^2 is then

$$(\chi^2_+)_k = r_k R_k^{-1} r_k \,. \tag{4.16}$$

Smoothing After the last measurement has been added to the fit, the information is propagated backwards to all the previous states in the smoothing step. The smoothed state vector and covariance matrix are

$$\overrightarrow{x}_k^n = \overrightarrow{x}_k + A_k(\overrightarrow{x}_{k+1}^n + \overrightarrow{x}_{k+1}^k) \tag{4.17}$$

$$C_k^n = C_k + A_k(C_{k+1}^n - C_{k+1}^k) A_k^T \tag{4.18}$$

where

$$A_k = C_k F_{k+1}^T (C_{k+1}^k)^{-1} \tag{4.19}$$

is the 5×5 smoother gain matrix. The smoothed residual and covariance matrix are then

$$r_k^n = m_k - h_k(\overrightarrow{x}_k^n) \tag{4.20}$$

$$R_k^n = V_k - H_k C_k^n H_k^T \tag{4.21}$$

and the smooothed contribution to the total χ^2 is

$$(\chi_+^2)_k^n = r_k^n (R_k^n)^{-1} r_k^n \,. \tag{4.22}$$

At this level all the measurements have been included and their information propagated on all the states with which the track is made.

4.3 The χ^2 minimisation

The aim of the track fitting is to find the optimal parameters to describe the trajectory of a charged particle that traverses a detector. They are determined by the minimisation of the χ_+^2 given in Eq. (4.22) and summed to obtain a total χ^2 in the form

$$\chi^2 = r^T V^{-1} r. \tag{4.23}$$

The optimal set of track parameters x is the one that minimises Eq. (4.23), so that it satisfies the condition

$$\frac{d\chi^2}{dx} = 0 \,. \tag{4.24}$$

Eq. (4.24) can be rewritten by using an initial estimate x_0 of the track parameters and a linear expansion of the measurement model around it

$$h(x) = h(x_0) + H \cdot (x - x_0) \,, \tag{4.25}$$

where

$$H = \left. \frac{\partial h(x)}{\partial x} \right|_{x_0} \tag{4.26}$$

is the projection matrix of Eq. (4.9). Eq. (4.24) then becomes

$$0 = \frac{d\chi^2}{dx} = -2H^T V^{-1}[m - h(x_0) - H(x - x_0)] \tag{4.27}$$

The solution of Eq. (4.27) is

$$x = x_0 - CH^T V[m - h(x_0)]\,, \tag{4.28}$$

where the covariance matrix of the track parameters is given by

$$C = 2\left(\frac{d^2\chi^2}{dx^2}\bigg|_{x_0}\right)^{-1} = 2\left(2H^T V^{-1}\frac{dh(x)}{dx}\bigg|_{x_0}\right)^{-1} = (H^T V^{-1} H)^{-1}. \tag{4.29}$$

If H depends on x (non-linearity), iterations are needed in order to reach some predefined convergence criterion. This criterion is usually a minimal change in the track χ^2. This numerical method of successive approximations of real zeros of a real function is called the Newton-Raphson method. In this case, Eq. (4.28) becomes

$$x = x_0 - \left(\frac{d^2\chi^2}{dx^2}\bigg|_{x_0}\right)^{-1} \frac{d\chi^2}{dx}\bigg|_{x_0}. \tag{4.30}$$

In order to use the Kalman filter fit in an alignment procedure, not only the track parameters x but also the alignment parameters α need to be taken into account in the measurement model

$$h(x) \to h(x, \alpha)\,. \tag{4.31}$$

Once the track parameters x have been determined through a track fit using a first estimate of the alignment parameters, they can be obtained by minimising the sum of the track χ^2 with respect to α, taking into account the dependence of x on α through the total derivative

$$\frac{d}{d\alpha} = \frac{\partial}{\partial\alpha} + \frac{dx}{d\alpha}\frac{\partial}{\partial x}\,. \tag{4.32}$$

The matrix of derivatives $dx/d\alpha$ comes from the condition for the χ^2 to be minimal with respect to the track parameters x, from which it follows that

$$\frac{d}{d\alpha}\left(\frac{\partial\chi^2}{\partial x}\right) = \frac{\partial}{\partial\alpha}\left(\frac{\partial\chi^2}{\partial x}\right) + \frac{dx}{d\alpha}\frac{\partial^2\chi^2}{\partial x^2} = 0\,. \tag{4.33}$$

This implies

$$\frac{dx}{d\alpha} = -\frac{\partial^2\chi^2}{\partial\alpha\partial x}\left(\frac{\partial^2\chi^2}{\partial x^2}\right)^{-1}\,. \tag{4.34}$$

Then the condition that the total χ^2 be minimal with respect to the alignment parameters can be expressed as

$$\frac{d\chi^2}{d\alpha} = 0\,. \tag{4.35}$$

This condition leads to a system of N coupled non-linear equations, where N is the number of alignment parameters. This system is solved using the Newton-Raphson method.

As for the track fitting, the solution is found through a linear expansion around an initial estimate α_0 of the alignment parameters. The system of N linear equations to solve for $\Delta\alpha$ becomes

$$\left.\frac{d^2\chi^2}{d\alpha^2}\right|_{\alpha_0}\Delta\alpha = -\left.\frac{d\chi^2}{d\alpha}\right|_{\alpha_0}\,. \tag{4.36}$$

Linearising the residual $r = m - h(x,\alpha)$ up to the first order around the expansion point $(x(\alpha_0),\alpha_0)$ and defining its derivative to α as

$$A_{ij} = \frac{\partial r_i}{\partial\alpha_j}\,, \tag{4.37}$$

then the derivative of the track parameters with respect to α, in Eq. (4.34), can be written as

$$\frac{dx}{d\alpha} = -\left(-2A^TV^{-1}H\right)\left(H^TV^{-1}H\right)^{-1} = A^TV^{-1}HC \tag{4.38}$$

and the total derivative for α, in Eq. (4.33), can be written as

$$\frac{d}{d\alpha} = \frac{\partial}{\partial\alpha} + A^T V^{-1} H C \frac{\partial}{\partial x}\,. \tag{4.39}$$

The first and second derivative for the track χ^2 with respect to the alignment parameters α are given by

$$\begin{aligned}\frac{d\chi^2}{d\alpha} =& \frac{d\chi^2}{\partial\alpha} + A^T V^{-1} H C \frac{\partial\chi^2}{\partial x} \\ =& 2A^T V^{-1} r + A^T V^{-1} H C \left(-2H^T V^{-1} r\right) \\ =& 2A^T V^{-1} \left(r - H C H^T V^{-1} r\right) \\ =& 2A^T V^{-1} \left(V - H C H^T\right) V^{-1} r\end{aligned} \tag{4.40}$$

and

$$\begin{aligned}\frac{d^2\chi^2}{d\alpha^2} =& \frac{d}{d\alpha}\left(\frac{d\chi^2}{d\alpha}\right) \\ =& 2A^T V^{-1} \left(V - H C H^T\right) V^{-1} A\,.\end{aligned} \tag{4.41}$$

Comparing these equations with Eq. (4.27) and Eq. (4.29) the difference is in the matrix HCH^T. This matrix represents the covariance matrix of the track parameters in the measurement space, and

$$R = V - H C H^T \tag{4.42}$$

is the covariance matrix of the residuals r, already found in the track fit.

If the track parameters x are the best estimate for the given alignment parameters, *i.e.* they satisfy the condition in Eq. (4.27)), then it is $H^T V^{-1} r = 0$ and the first derivative in Eq. (4.40) becomes

$$\frac{d\chi^2}{d\alpha} = 2A^T V^{-1} r\,. \tag{4.43}$$

If the residuals are not linear in α and x, the procedure needs several iterations to obtain $\Delta\alpha$. A criterion to stop the iterations is the change in the χ^2. Ignoring the higher order derivatives in α, the change in the total

χ^2 as a result of a change in the alignment parameters can be written as

$$\begin{aligned}\Delta\chi^2 &= \left(\frac{d\chi^2}{d\alpha}\right)^T \Delta\alpha \\ &= \left(-\frac{d^2\chi^2}{d\alpha^2}\Delta\alpha\right)^T \Delta\alpha \\ &= -\left(\Delta\alpha\right)^T \left(\frac{d^2\chi^2}{d\alpha^2}\right) \Delta\alpha \\ &= -\left(\Delta\alpha\right)^T \mathrm{Cov}(\alpha)^{-1} \Delta\alpha\,.\end{aligned} \tag{4.44}$$

So that the change in the total χ^2 is equivalent to the significance of the correction to the alignment parameters. For a value of $\Delta\chi^2$ less than 1 the changes in the alignemnt parameters are statistically insignificant and, thus, the alignment parameters can be considered as having converged.

4.3.1 The Histogram based method

The residuals between a hit measurement and the track are the quantities at the basis of the alignment methods. They enter in the minimisation of the χ^2 by its own definition

$$\chi^2 = \sum \frac{(m - h(x))^2}{\sigma_m^2} = \frac{r^2}{\sigma^2} \tag{4.45}$$

where $r = m - h(x)$ is the residual between the measurement m and the track defined by the function h, and σ is the measurement error.

An alignment software dedicated to the Muon Detector and based on the residual distributions of tracks crossing all the stations was developed to determine the detector alignment constants.

In this method, the Histogram Based method, the residuals are used in a direct way for the estimate of the mis-alignments. The method is a simplified procedure that does not take into account the material traversed by the particles even though the Muon stations are interspersed with absorbers to stop hadrons and to select muons (the calorimeters between stations M1 and M2, iron filters amid the other stations) and the multiple scattering is not negligible.

In principle the method can handle a global alignment, in which case it uses tracks which should be provided by an external algorithm. Here it was used to perform a local alignment. In this instance a frame of reference is set by fixing two stations, assumed to be in their nominal position. The tracks are defined by the hits in these two reference stations, and then extrapolated to the others.

In case of local alignment, once the tracks are defined as described above, the residuals are calculated in the remaining stations. This procedure is performed in the (x, z) and (y, z) planes independently. The distributions of the mean values of the residuals as a function of the coordinates yield a direct evaluation of the mis-alignment. The residuals will be distributed around zero mean in case of perfect alignment, or non zero mean in case of misalignment.

Compared to an alignment method like the Kalman filter fit, the Histogram Based method presents several semplifications, as the errors of the measurements and the material crossed by the particles are not taken into account, and there is no track fit. On the other hand it has some advantages: a mis-alignment of a (half-)station is not propagated to the others because there is no track fit, and the residual distributions are more sensitive to local systematics, as the sampling of the measurements. In any case the analysis of the residual distributions reveals to be particularly useful in working out irregularities related to the response of the Muon Detector.

Chapter 5

Global alignment with Monte Carlo single muons

The first validation of the alignment method applied to the Muon Detector was performed with Monte Carlo muons in the simplest configuration, that is using single muons coming from the interaction point. The simulation was performed with both the detector aligned and misaligned to test the effectiveness of the method in reproducing the input values of its positions.

When this work started, a track reconstruction in the Muon Detector was foreseen only for the muon particle identification. The algorithm for the track reconstruction is based on the extrapolation of the *long tracks*[1] to the Muon stations [32]. To perform a local alignment of the Muon Detector it was necessary to develop a track finding algorithm that could only rely on the the information if the Muon Detector. However, to provide a global alignment for the Muon Detector, the muon tracks had to be converted into the standard LHCb track format. For this purpose a measurement model for the muon readout elements had to be added to the LHCb measurement models, so that the standard Kalman filter track fitting could be adopted.

After a first stage of preliminary studies on the local alignment, the

[1]The long tracks are tracks reconstructed by the whole LHCb tracking system from the VELO to the T stations.

tracks reconstructed in the Muon Detector could be matched with the long tracks. This was possible because the Monte Carlo simulated single muons were generated in the interaction point and simulated in the whole apparatus.

5.1 The LHCb software chain

For the purpose of this study several Monte Carlo data have been simulated according to a software in use at LHCb that is here described.

The LHCb software is based on the Gaudi framework [33, 34]. It is organised in a chain of applications that take care of different phases, from the simulation to the analysis, collecting the algorithms needed.

The event simulation is performed with the external program Pythia [35] which simulates the $p - p$ interactions, while the B decay part is controlled by EvtGen [36]. After the event generation the evolution of the particles in the detector is simulated by Geant4 [37,38] who takes care of the interactions of particles with the materials inside the detector, the effect of the magnet on the trajectories of charged particles and the decay of unstable particles. All these phases are controlled by Gauss [39], the simulation project.

The Boole [40] application takes as input the Gauss output and simulates the response of each detector, the *digitisation* procedure. In this phase the imperfections of the detectors measured in the test beam are included, as in particular the electronic noise and the cross talk. The Boole output file has the same format as the data provided by the acquisition system, so that from this point on the applications and the algorithms they include can indifferently and equally handle both simulated and real data with no needs of changes.

The subsequent application in the chain is Brunel [41], the reconstruction project, who has the task of running the reconstruction of tracks and vertices and the algorithms of particle identification.

Finally the event selection algorithms are executed in the DaVinci [42] application.

In addition, the application Panoramix [43] can be used to visualize the events at different stage of the software application chain.

For specific studies, instead of the whole $p-p$ collision event provided by Pythia, it is also possible to generate single particles by the `ParticleGun` algorithm, where the type of particle (p, μ, e, π, J/ψ), the momentum range, the angular distribution and the position of the production vertex are set by the user. In addition a generator for cosmic rays, `CosmicsGun` [56], was added to the package.

5.2 Simulation

The simulation of single $\mu^{\pm}$ was performed with the `ParticleGun` package, with an uniform momentum distribution in the range form 5 to 100 GeV/c and a uniform angular distribution in the full acceptance of the detector. Even though this is an ideal distribution, not completely corresponding to the expected experimental one, with the simulated data a deep analysis is allowed.

With this configuration of angular and momentum distributions, two different data samples were generated. The displacements are introduced through the databases that are picked up in the track reconstruction. In order to test the ability of the alignment methods of reproducing the input positions of the stations, a first sample was generated with the nominal positions of the detector elements, and a second one with an asymmetrical opening of the station M4. The M4 A side was opened by 3mm and the M4 C side by 6 mm. These values were chosen $O(1\text{mm})$, *i.e.* of the same order of magnitude of the required precision on the alignment, [31]. An asymmetrical opening was chosen in order to test different values of mis-alignment.

A total of $180,000$ events are in the aligned and $120,000$ in the mis-aligned samples. In the mis-aligned case, the data were simulated with the mentioned displacement of the M4 station, while the digitisation and reconstruction were performed using the nominal positions of the detector elements, in this way mimicking an unknown mis-alignment.

5.3 Reconstruction and track selection

When the work on the alignment started, the algorithm for the track finding and reconstruction had to be developed to perform the alignment of the Muon Detector.

Following the same procedure of the High Level Trigger [44] reconstruction algorithm, a new algorithm was derived as the `AlignMuonRec` algorithm of the package `MuonTrackAlign`. The algorithm was expanded to include a pad clusterisation to properly take the cross talk into account, and a process to convert the reconstructed tracks into objects of the class LHCb::Track. In addition, a measurement model was created for the Muon Detector so that the tracks could be fitted with the Kalman filter fit. Thus the Kalman filter fit was set as the default track fit for the reconstructed tracks.

The original intention was to perform a stand-alone alignment of the Muon Detector, and for this purpose the reconstruction algorithm was developed. Since it is possible to match the reconstructed muon tracks with the long tracks and to perform a global alignment, this was eventually done developing a matching algorithm.

The track finding starts with hits on M5 station, to be used as *track seeds*. Then a Field Of Interest (FOI) is opened on M4 around the direction connecting the seed on M5 to the interaction point. When a hit is found in this area, the direction connecting the seed and the hit on M4 is extrapolated on M3 and a FOI is opened around it. When a hit is found on M3, it is used together with the hit found in the previous station to determine the new direction around which the FOI in M2 is opened. As last step, the direction individuated by the hits found in M3 and M2 is extrapolated on M1 and a FOI is opened on this station in order to search for hits. This procedure is depicted in Figure 5.1. The size of the fields of interest depends on the station and on the region for taking into account the multiple scattering, the pad size and the particle deflection in the (x, z) plane because of the magnetic field, Table 5.1.

In case of real events of collisions, where more than one muon is formed, the algorithm may find two or more tracks with hits in common

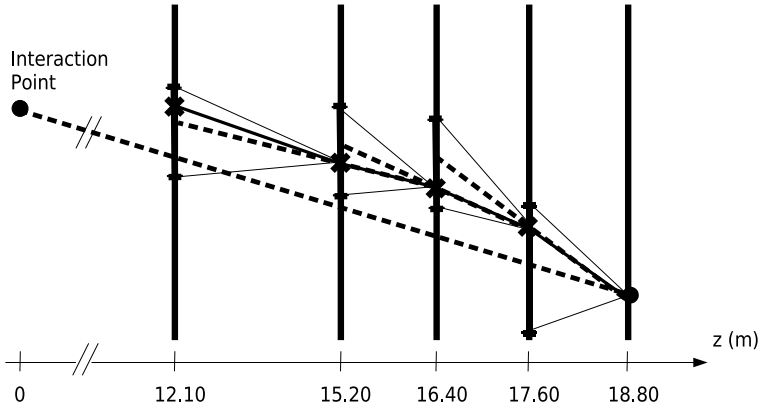

Figure 5.1: Sketch representative of the track finding implemented in the `AlignMuonRec` algorithm. Dashed lines indicate the directions around which the fields of interest (thin lines) are opened. Thick lines indicate the track segments between a station and the next one.

(*clone tracks*). Clones have to be eliminated to avoid double counting of tracks. Two methods to detect and eliminate clones were developed. In the first method a clone is defined when two tracks share hits in M2, M3 and M4, and in the second when the hits are shared only in M2 and M3. In both methods a flag is assigned to one of the two tracks.

	M1	M2	M3	M4
R1	100×30	100×60	100×60	400×60
R2	200×60	200×120	200×120	400×120
R3	300×100	300×180	300×240	400×240
R4	400×150	400×240	400×480	400×480

Table 5.1: The size (x(mm)$\times y$(mm)) of the field of interest opened in the different regions and stations in the track finding.

In the Monte Carlo samples of muons, the particles are generated in the interaction point. Unless they have large slopes and low momentum, so that they are kicked out by the magnet, they cross the entire LHCb detector, from the VELO to the Muon stations, leaving hits in all the detectors they traverse.

Once the track segments are found and reconstructed in the Muon

Detector with programs *ad hoc* developed, it is then possible to match these segments with the long tracks. The matching makes possible to profit of the better resolution of the tracking detectors in the determination of the tracks, and also to perform a global alignment, *i.e.* to evaluate the position of the detector elements with respect to the global system of reference of the LHCb experiment set by the VELO.

The matching, depicted in Figure 5.2, is performed by calculating a χ^2 with the coordinates and the slopes of the two segments of a complete track, the long track and the muon segment, to be matched

$$\chi^2_{match} = \frac{(x_L - x_\mu)^2}{\sigma^2_{x_L} + \sigma^2_{x_\mu}} + \frac{(y_L - y_\mu)^2}{\sigma^2_{y_L} + \sigma^2_{y_\mu}} + \frac{\left(t_{x_L} - t_{x_\mu}\right)^2}{\sigma^2_{t_{x_L}} + \sigma^2_{t_{x_\mu}}} + \frac{\left(t_{y_L} - t_{y_\mu}\right)^2}{\sigma^2_{t_{y_L}} + \sigma^2_{t_{y_\mu}}} \quad (5.1)$$

where $x_L(y_L)$ and $x_\mu(y_\mu)$ are the $x(y)$ coordinates of the first state of the muon track segment and the last state of the long track segment, respectively. The the long track is extrapolated at the same z of the first state of the muon track segment. t_{x_L} and t_{y_L} are the slopes in the (x, z) and in the (y, z) planes of the long track, while t_{x_μ} and t_{y_μ} are calculated as

$$t_{x_\mu} = \frac{x_{M_2} - x_{M_1}}{z_{M_2} - z_{M_1}} \quad \text{and} \quad t_{y_\mu} = \frac{y_{M_2} - y_{M_1}}{z_{M_2} - z_{M_1}}\,. \quad (5.2)$$

It was experimentally found that in order to have a good match, a cut on the $\chi^2_{match} < 12$ need to be imposed.

This matching procedure was performed with both the aligned and mis-aligned Monte Carlo samples of muons produced.

With these *complete* tracks (long + muon) the (global) alignment of the ten half-stations that compose the Muon detector was carried out with $180,000$ in the aligned and $120,000$ events in the misaligned samples.

5.3.1 Cross Talk correction

A delicate topic in the optimisation of the algorithm for the track reconstruction in the Muon Detector, is the treatment of the cross talk.

The cross talk occurs when a particle passing through a detector station generates more than one hit on the logical pads. It can be of

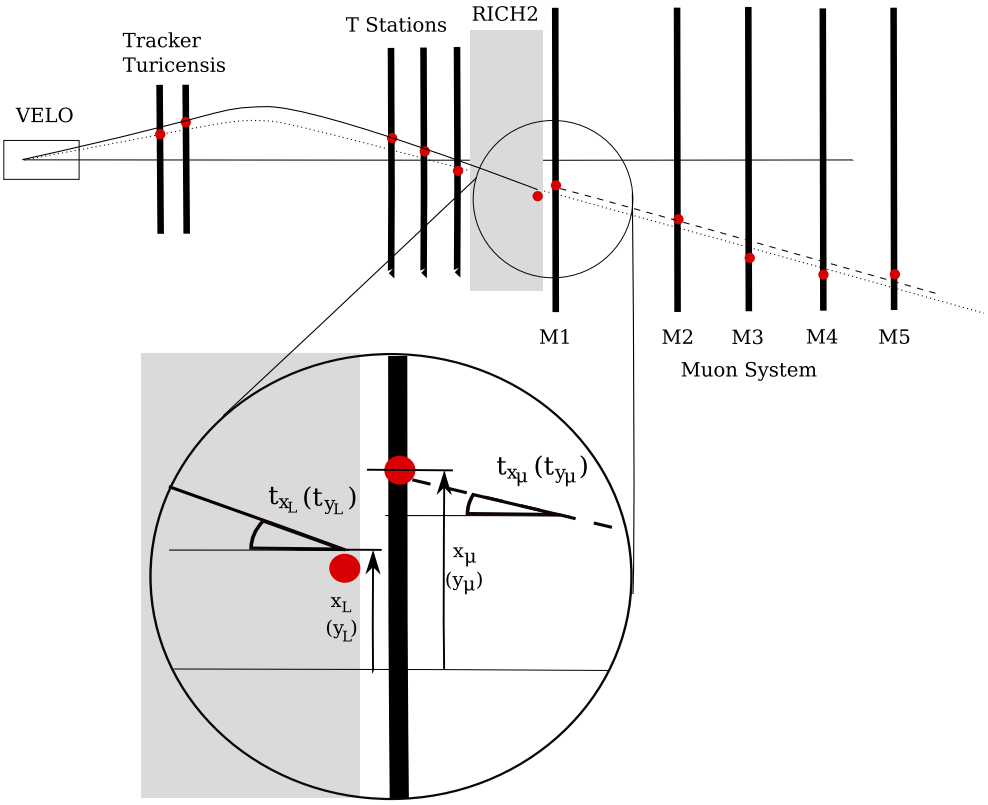

Figure 5.2: Sketch showing the matching betwen a track reconstructed in the Muon System and a long track. Dotted line: trajectory of the simulated muon. Red dots: the hits left by the particles in the detectors. Solid line: the long track reconstructed by the tracking system. Dashed line: the muon track reconstructed in the Muon stations. Zoom on the matching region showing the slopes and the coordinates of the two matching tracks. The last state stored by default in the long tracks is located at end of the RICH2.

different nature depending on the mechanism by which the signal in the additional pads is generated [49]:

- the *electronic* cross talk is due to capacitive and inductive couplings of pads;

- the *direct* cross talk can originate when a particle traversing a pad close to its border induces a signal on a neighbour pad. If the pads are small, it occurs even if the particle is not passing close to the border;

- the *geometrical* cross talk occurs when a particle with a trajectory far from the normal to the plane, hits a chamber. It then may occur that it does not cross the same pad in the two (bi)gaps.

Depending on the origin of the cross talk the measurement associated to the hits should be considered in a different way: in the case of electronic cross talk only one pad is correctly associated to the coordinate of the particle, being the additional cross talk hits induced by capacitive or inductive coupling. As it is impossible to identify the right hit, in principle a measurement corresponding to the sum of the hits should be used. In practice since it is a minor effect (3%) with respect to the direct and the geometric ones, the electronic cross talk is neglected, and the measurement is treated as if the whole cross talk were direct and geometrical.

In the cases of direct and geometrical cross talk, instead, the different hits are all associated to the particle thus they have to be taken into account.

A study on the best treatment of the pads hit by cross talk was performed testing the effects of the resulting reconstruction on the alignment. Three configurations were studied to optimise the reconstruction algorithm. The first one just ignores the cross talk, so that all the hits are associated to muons. In the second configuration, if more than one hit is found in the Field Of Interest, the closest to the position of the extrapolated direction is used, neglecting the others. In the third, the

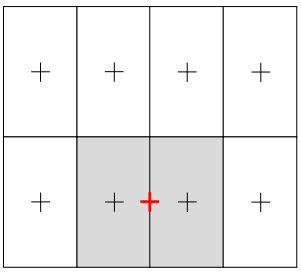

Figure 5.3: Scheme of the large virtual pad: eight pads are drawn with their centres. In grey two neighbour hit pads clustered in a larger pad. In red the centre of gravity of the larger pad.

adjacent hit pads are regarded as clustered together to form one larger pad with coordinates cooresponding to those of the centre of gravity of the pad cluster, as depicted in Figure 5.3.

In all the three configurations the cross talk on M5 was not taken into account, since all the hits found on the station were used as seeds for the track finding. Once the best of the three configuration was identified, a clusterisation was also made with the pads in M5 hit by cross talk.

The three cross talk configurations are tested evaluating their influence on the global alignment of the ten half-stations of the detector. The results are shown in Figure 5.4 for data simulated with an aligned detector, and in Figure 5.5 for data simulated with the two halves of the M4 station misaligned. Tables with errors are reported in Appendix A. In the aligned case, Figure 5.4 (a), with no cross talk correction the flow of the alignment constants spreads in a larger interval, introducing apparent misalignments. In (b) and (c) plots, the values are more grouped with no sensible difference one from the other. In the misaligned case, Figure 5.5 (a), the displacement introduced in input is rapidly reached, however, the mis-aligned M4 half-station induces an apparent mis-alignmnet also on the two half-stations of M5. In the (b) plot the half displaced by 6 mm is found at 3 mm from the expected position. In the (c) plot, a good compromise is reached: the mis-alignment of M4 is reproduced and a smaller displacement is induced on M5.

Of the three cross talk configurations the correction by large pads seemed to better approximate the input conditions relative to the half-station positions. Thus the correction was adopted and the subsequent alignment study was performed with the clusterisation in the large virtual pad in all the five stations of the Muon detector.

5.4 Multiple scattering

The interaction of a charge particle with the LHCb detectors is carried on by the Geant4 program. It uses a so-called *condensed* algorithm to simulate multiple scattering, as usually done by the high energy sim-

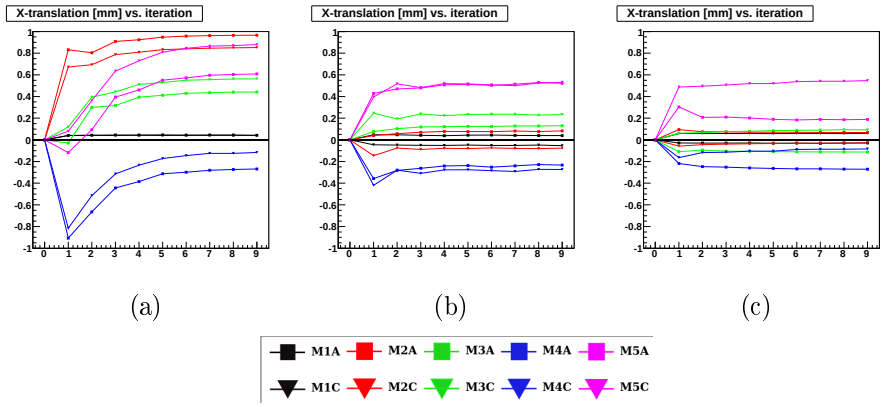

Figure 5.4: Comparison of the flow of alignment constants of the 10 half-stations aligned for translations along x. Data simulated with the detector aligned, and reconstructed with the three different treatments of the cross talk as described: (a) no cross talk is considered; (b) only the hit pad closest to the extrapolated direction; (c) the pad clustersation is taken into account.

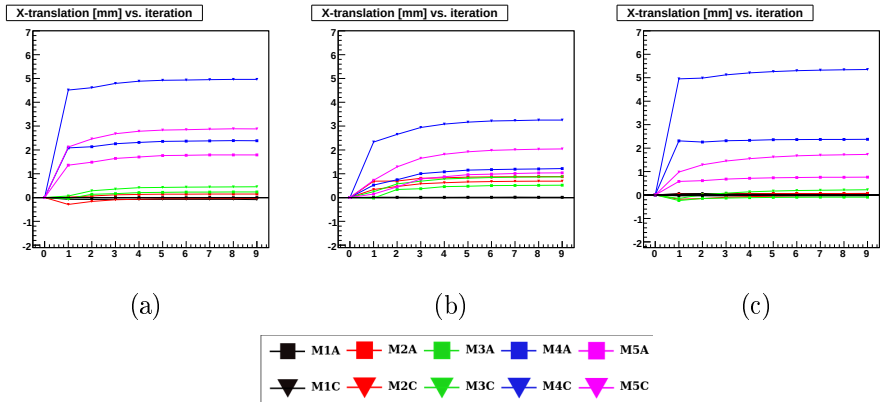

Figure 5.5: Comparison of the flow of alignment constants of the 10 half-stations aligned for translations along x. Data simulated with the half-stations of M4 opened by 3mm (A side) and 6mm (C side), and reconstructed with the three different treatments of the cross talk as described: (a) no cross talk is considered; (b) only the hit pad closest to the extrapolated direction; (c) the pad clusterisation is taken into account.

ulation codes [45]. To save processing time, the condensed algorithms do not simulate all the interactions experienced by the particle that traverses a material, but compute the global effects of the collisions (lateral displacement and change of direction) at the end of a track segment.

The most used theories of multiple scattering are of Molière [46], Goudsmit and Saunderson [47], and Lewis [48]. While the first two give only the angular distribution after a step, the Lewis theory, on which Geant4 is based, calculates also the moments of the spatial distribution. Because none of the theories gives the probability distribution of the spatial displacement, the simulation codes have their own algorithm to determine the spatial displacement of the particle after a given step. These algorithms are not exact, and are the sources of the most uncertainties in the multiple scattering simulation codes. Their results can strongly depend on the value of the step length, that has to be carefully chosen.

While the step chosen for the multiple scattering simulation in the LHCb detector materials is a good compromise between the simulation accuracy and the time consuming, in the thick iron filters of the Muon Detector a proper choice of the step length would require a huge computing time. To keep this time under a reasonable level, the step length was by default set too large.

Given the relevence of the multiple scattering simulations for the Muon Detector, the best options to be set in Geant4 in order to improve the simulation have been investigated. The angular distribution given by the Molière theory has been used for a comparison with the Geant4 simulation.

According to this theory, the change of direction after a path of length x inside a material is roughly Gaussian for small deflection angles. The width of the distribution of deflection angles projected in a plane is

$$\vartheta_0 = \frac{13.6\,\mathrm{MeV}}{\beta cp} z \sqrt{\frac{x}{X_0}} \left[1 + 0.038 \ln\left(\frac{x}{X_0}\right) \right] \tag{5.3}$$

where p, βc, and z are momentum, velocity and charge of the particle, and x/X_0 is the thickness of the material traversed expressed in radiation lenght.

In Figure 5.6 the lateral displacement δx versus the change of direction $\delta\vartheta_x$ in the (x, z) plane is plotted. The δx is calculated as

$$\delta x = x_{M_i} - x_{M_{i-1}} \tag{5.4}$$

i.e. as the difference of the x coordinate between a station and the previous one. Similarly $\delta\vartheta_x$ is computed as

$$\delta\vartheta_x = \vartheta_{x_{M_i}} - \vartheta_{x_{M_{i-1}}} \,. \tag{5.5}$$

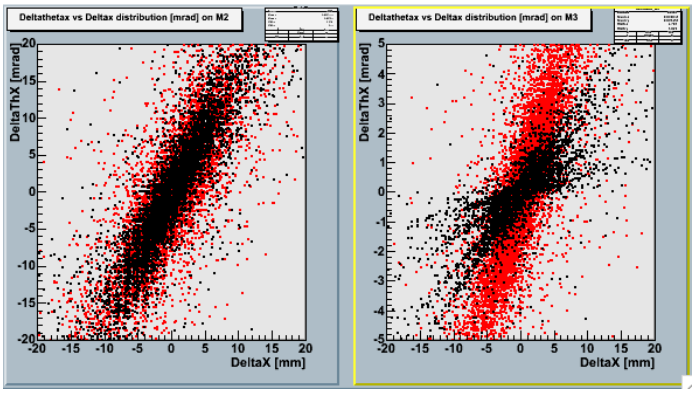

Figure 5.6: The distribution of δx versus $\delta\vartheta_x$ in M2 where the multiple scattering is due to the calorimter materials (left), and in M3 where the multiple scattering is due to the iron in the filters. In red the distributions simulated according to the formula of the Molière theory, in Eq. (5.3), while in black the LHCb simulation. It can be seen the non correct correlation between δx and $\delta\vartheta_x$ of the iron filter, in the black distributions.

In the left side of the figure the distributions are plotted where the multiple scattering is due to the materials of the calorimeters, between M1 and M2 stations, while in the right side where the multiple scattering is due to the iron filters, between M2 and M3 stations. The two distributions, in black that of Geant4 and in red that calculated according to Eq. (5.3) are superimposed.

For the M1-M2 simulation the two distributions are in agreement, while for the M2-M3 the black distribution shows an incorrect correlation between δx and $\delta\vartheta_x$, probably related to the number of steps in the filter used by the default simulation. In fact, tuning the settings of Geant4 a better simulation has been achieved. These settings have been used to simulate data for the alignment with Monte Carlo cosmic rays, later on discussed.

The effect of this not proper simulation of the multiple scattering in

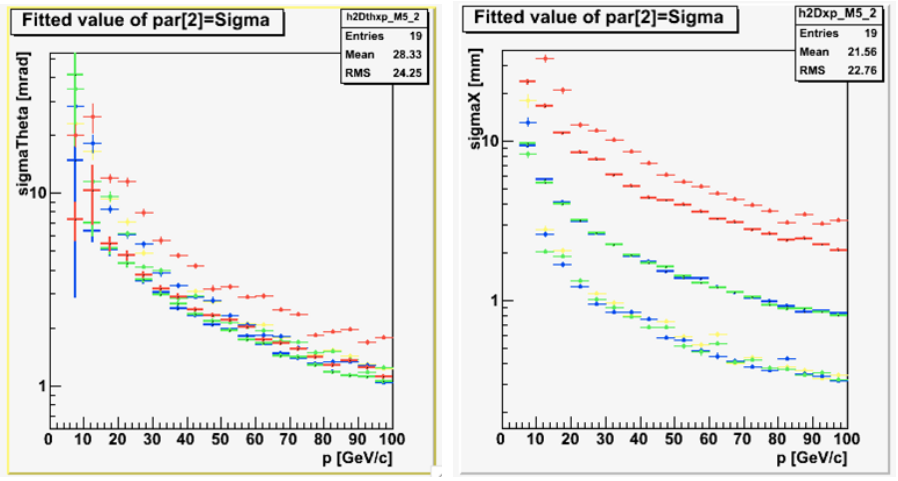

(a) (b)

Figure 5.7: The sigmas of the distributions of $\delta\vartheta_x$ (a) and δx (b) for the different stations (M2 in red, M3 in green, M4 in blue and M5 in yellow) and the two different simulations (thin lines LHCb simulation, thick lines Molière theory).

the iron filters is an under-estimation of the multiple scattering contribution to the measurement errors. In Figure 5.7 there are plotted the sigmas of the distributions of ϑ_x (left plot) and x (right plot) versus the momentum of the particle traversing the material for the different stations (M2 in red, M3 in green, M4 in blue and M5 in yellow). As can be seen the sigmas on ϑ_x for the station M2 are a bit over-estimated with respect to the others. While among the sigmas on δx there is an over-estimation for the station M2, a systematic under-estimation is present for the other stations, though interleaved by the iron filters.

5.5 Global alignment with Kalman filter fit method

5.5.1 Aligned sample

The global alignment of the Muon Detector was performed with a sample of 120,000 complete tracks under the conditions

- the half stations in their nominal positions
- cross talk correction by cluster of pads
- approximate simulation of the multiple scattering, resulting in a possible under-estimation of the errors.

The results on the alignment constants, *i.e.* the positions of the detector elements determined by the alignment procedure, are given in Table 5.2 and shown in Figure 5.8, where the flow of the alignment constants shows a quick and stable convergence.

	Translations x		Translations y	
station	A Side	C Side	A Side	C Side
M1	0.01 ± 0.04	0.04 ± 0.04	-0.02 ± 0.10	-0.12 ± 0.10
M2	0.03 ± 0.03	-0.05 ± 0.03	-0.07 ± 0.12	-0.16 ± 0.12
M3	-0.15 ± 0.03	0.04 ± 0.03	-0.01 ± 0.13	-0.31 ± 0.13
M4	-0.31 ± 0.12	-0.41 ± 0.12	0.10 ± 0.15	-0.21 ± 0.15
M5	-0.21 ± 0.13	-0.13 ± 0.13	0.05 ± 0.17	-0.27 ± 0.17

Table 5.2: The alignment constants with errors in aligning the ten half-stations M1 to M5 for translations along x and y with data simulated with the detector in the nominal position.

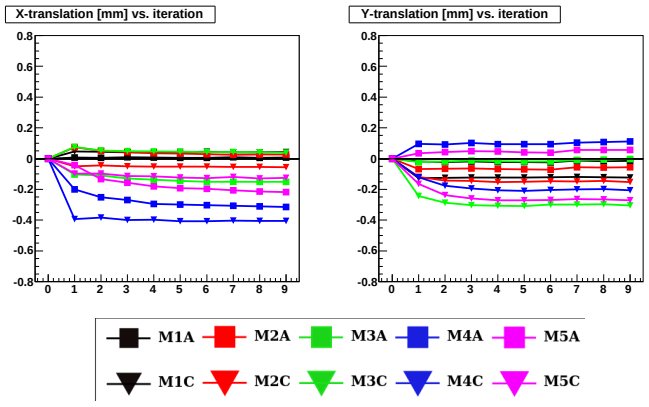

Figure 5.8: The flow of the alignment constants versus iteration aligning the ten half-stations for translations along x (left plot) and y (right plot), obtained with data simulated with the detector in the nominal position.

As can be seen the constants are compatible with the nominal positions of the detector elements within 3σ, with the exception of M3 A side, within 5σ, and M4 C side, within 4σ, both along x.

The alignment results can be regarded as satisfactory. However, it has to be considered that the multiple scattering in the iron absorbers is not properly simulated, and this may result in an under-estimatation of the multiple scattering contribution to the errors . The pattern of the errors, that approximately increase from station M1 to M5, depends on the contribution of the multiple scattering and, as far as x in concerned, also on the contribution of the variable pad size.

5.5.2 Misaligned sample

With the misaligned data sample the global alignment was performed with $85,000$ complete tracks under the conditions

- M4 A side opened by 3 mm, M4 C side opened by 6 mm, and the other half stations in their nominal positions
- cross talk correction by cluster of pads
- approximate simulation of the multiple scattering, resulting in a possible under-estimation of the errors.

The results obtained for the alignment constants are listed in Table 5.3 and shown in Figure 5.9, where, also in this case, a quick and stable convergence is reached. The input mis-alignment values are roughly reached in the first iterations.

The displacement of the two mis-aligned stations, M4 A and C sides, lie within 5σ and 4σ, respectively, with respect to the expected values. In addition, also M3 A side is in its nominal position within 5σ. The other half-stations are compatible with their nominal position within 3σ.

The same remarks on the errors made for the aligned case are still valid here, however the smaller number of tracks used reflects in the errors that are globally larger.

	Translations x		Translations y	
station	A Side	C Side	A Side	C Side
M1	-0.01 ± 0.05	0.01 ± 0.05	-0.17 ± 0.12	-0.12 ± 0.12
M2	0.04 ± 0.03	-0.10 ± 0.03	-0.08 ± 0.14	-0.25 ± 0.14
M3	-0.20 ± 0.04	0.04 ± 0.04	-0.17 ± 0.16	-0.18 ± 0.16
M4	2.35 ± 0.14	5.48 ± 0.14	-0.20 ± 0.18	-0.36 ± 0.18
M5	-0.12 ± 0.16	-0.17 ± 0.16	-0.22 ± 0.20	-0.47 ± 0.20

Table 5.3: The alignment constants with errors aligning the ten half-stations M1 to M5 for translations along x and y with data simulated with the misaligned detector: the halves M4 A and M4 C start from $+3$ mm and $+6$ mm respectively.

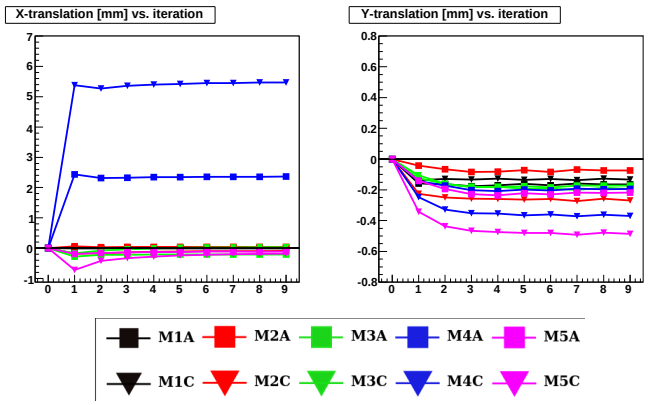

Figure 5.9: The flow of the alignment constants versus iteration aligning the ten half-stations for translations along x (left plot) and y (right plot), obtained with data simulated with misaligned detector: the halves M4 A and M4 C start from $+3$ mm and $+6$ mm respectively.

5.5.3 Error analysis

On these data a study of the errors on the alignment constants calculated by the chisquare minimisation method of alignment was performed. It was intended to verify whether the errors, both in x and y, follow the expected pattern of a dependence on $1/\sqrt{N}$, where N is the number of tracks used. For this purpose the whole sample was splitted in subsamples in order to have the 10%, the 33%, the 50%, and the 100% of the whole available statistics. Figure 5.10 shows the errors on the alignment constants in x and y. For both x and y errors the expected pattern is

reproduced.

However, given the geometry of the detector and the presence of the iron filters, the errors depend not only on the statistics. In fact they also depend on the pad size, that varies with a ratio of $2:1:1:4:4$ in x from the M1 to the M5 station and are roughly constant in y and on the contribution of the multiple scattering. In Figure 5.10 this two other effects are also visible. The y errors in the different stations have no contribution from the pad size, being the y dimension of the pads roughly constant. The spread of the different lines in the plot is then due to the multiple scattering in the iron filters between the stations. In the x errors, also the variable pad size contributes in addition to the multiple scattering.

In fact while the small spread between the lines representing the errors in the various stations is due to the multiple scattering contribution, the larger spread between the couples of lines representing the stations M2 and M3, and M4 and M5 depends on the x pad size. Thus it is the same on the stations M2 and M3, and it is bigger by a factor of 4 on the stations M4 and M5.

The chosen ratio on the x pad size depends on the task of the stations: while M1÷M3 are used for the p_T determination for the Level-0 trigger, M4 and M5 are only used to confirm the presence of penetrating muons.

In addition, the errors on the M1 station are superimposed to those of station M2 as expected: the pad size designed for M1 is such to compensate for the multiple scattering of the particles in the calorimeter materials.

5.6 Conclusions

With the Monte Carlo simulation of single muons coming from the interaction point, the procedure of global alignment of the Muon Detector using tracks that traverse the whole LHCb apparatus was carried out with the Kalman filter fit in the two simulated cases

- all stations in the nominal positions

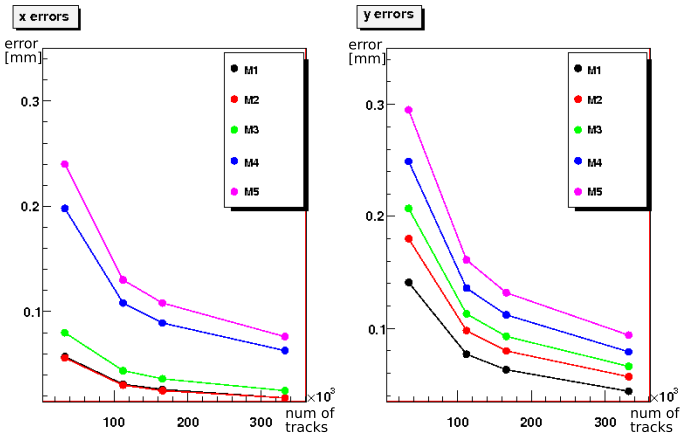

Figure 5.10: The errors on the alignment constats in x (left) and y (right). They show the correct pattern $1/\sqrt{N}$, where N is the number of tracks used. The spread between the different lines in the y error plot has to be ascribed to the multiple scattering in the iron filters between the stations. Since the y size of the pads is about the same in all the stations, no other effects should be present. In the x error plot, in addition to the multiple scattering effect, the influence of the pad size is visible in the spread between the couples of lines representing M2 and M3, and M4 and M5.

- mis-alignment of M4 station, opened asymmetrically of 6 and 3 mm.

The results were satisfactory.

For this purpose, an algorithm for the track finding and reconstruction was developed. The matching to the long tracks and a pad clusterisation to take into account the cross talk hits were performed. A study on the multiple scattering simulation in the iron filters was made.

Chapter 6

Local alignment with real cosmic rays

Since Summer 2008 two kinds of real data acquisitions were carried on during the commissioning of the LHCb detectors for their calibrations. The data taken are beam dump data and cosmic rays. During LHC injection tests, protons with an energy of 450 GeV/c^2 were extracted from the SPS, injected in the LHC ring, and dumped onto a beam stopper (called TED) situated 350 m downstream of LHCb. This created a spray of particles crossing the LHCb detectors. Since detectors like VELO, TT and IT have too small areas to succesfully acquire enough cosmic rays their first calibrations were made with the beam dump data. On the other hand in the interaction with the beam stopper many muons were produced, so that the occupancy in the Muon Detector was too high to be able to use these data for spatial alignment. Therefore OT and Muon Detector used cosmic rays for calibrations.

As far as the cosmic rays are concerned, several runs were acquired from August to October 2008. For the aligment studies carried on in this work, the first runs acquired had to be rejected because the ongoing measurements on the supporting walls and optimisation of the muon chamber thresholds for the cosmic data acquisition did not allow stable conditions.

Furthermore, in 2008 the station M1 was not yet in place, and actually

it was planned to run without that station for the first year of data taking, and to profit of the first winter shutdown for its installation. However, the one year delay caused by the incident occurred to the LHC machine in September 2008 allowed to perform the M1 installation, that was completed in July 2009.

6.1 Cosmic data trigger and acquisiton

The events were triggered by the coincidence of signals in the Electromagnetic and Hadronic calorimeters, except for run 34120, where the logical AND of the two bi-gaps of M3 chambers was also triggering the events.

During the commissioning period the configuration was not the nominal one: no CF_4 was present in the gas mixture of the Muon chambers, the high voltage was set at 2.5 kV, and the thresholds at 7.5 fC (10.5 fC on M4R3 and M5R3) for the pad readout and at 15 fC (18 fC on M4R4 and M5R4) for the wire readout, *i.e.* a factor 1.5 higher than the nominal values in order to reduce noise [50]. Moreover, during the cosmic data taking some readout channels had to be masked because too noisy or malfunctioning. Nevertheless some remaining noisy channels were still present and could affect the reconstruction of the tracks. For this reason an algorithm was developed to remove these channels off-line, before the reconstruction. Thus the signals coming from the readout channels counting more than the 5% of the total counts were ignored (they are 1% of the 18604 logical channels in M2÷M5).

The distribution of the hits in stations M2 to M5 after the noisy channel removal is shown in Figure 6.1. The empty regions correspond to the logical channels that were excluded from the acquisition. They are evident especially in M2, M4 and M5.

The cosmic runs acquired with stable geometry and threshold conditions, then used for the alignment after the removal of noisy channels, are listed in Table 6.1 together with the trigger used.

Since the time alignment of the readout channels was not optimized

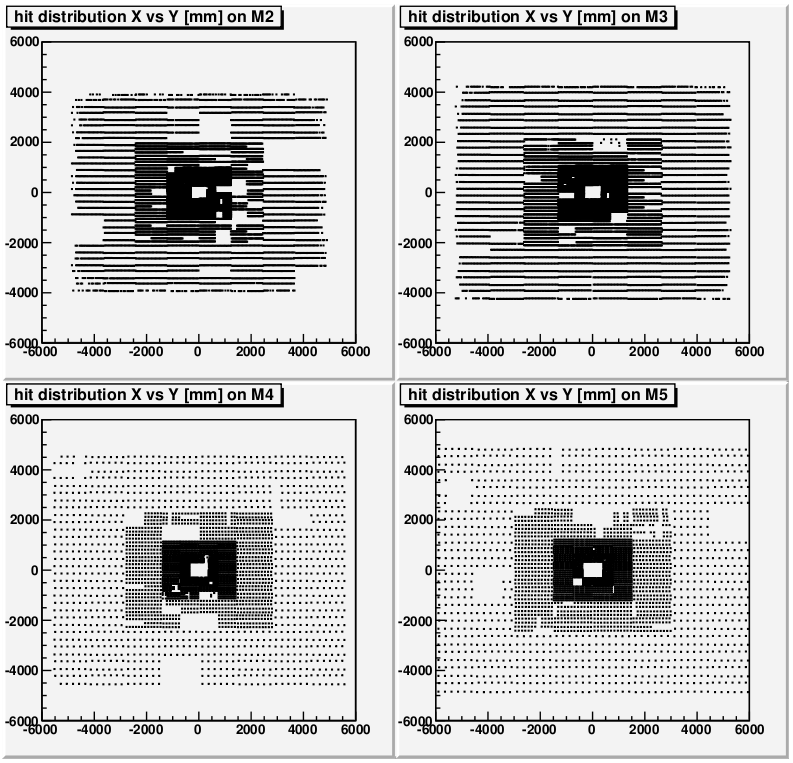

Figure 6.1: The hit distribution on stations M2-M5. Readout granularity and areas with dead channels are visible.

yet, in these runs the time window has been enlarged to accept events belonging to multiple bunch crossings around the central one. These events are defined Time Alignment Events (TAE) and the number of TAE indicates the number of bunch crossing accepted around the central one [51, 52]. For the runs used in this study, the TAE acquired is ± 3 for runs 34083 and 34117, ± 2 for the others. The enlarged time window allows to detect also backward going tracks that have a different time development in the detector.

In addition, most of the runs used are triggered by the calorimeters, which add constraints to the acceptance for the cosmic ray slopes.

Since samples of cosmic rays were acquired by OT and by the Muon Detector, these data were used to perform local alignments of the Muon Detector and OT, and then for a preliminary study to the relative alignment between the two detectors.

Run Number	Date	Trigger
34083	20/09/2008	
34117	20/09/2008	
34120	21/09/2008	Calo and Muon
35664	19/10/2008	Calo
35665	19/10/2008	Calo
35666	19/10/2008	Calo
35667	19/10/2008	Calo
35669	19/10/2008	Calo
35671	19/10/2008	Calo

Table 6.1: Run number, date of acquisition, and trigger used.

6.2 The Muon Detector from the cosmic ray point of view

The geometry of the Muon Detector was devised to detect muons coming from the interaction point. Its main features are accurately suited to meet this aim. Although already discussed, some of these features are here reminded since in conflict with the geometry of the cosmic rays.

- To detect particles with low slopes with respect to the horizontal plane, coming from the interaction point, the stations are projective with respect to the interaction point, while the cosmic rays have higher slopes and can also be directed backward, towards the interaction point.

- The stations are built with staggered chambers on the supporting walls to assure a complete coverage in the angular acceptance for particles from the interaction point. For cosmic ray directions this arrangement presents gaps in the acceptance. A detailed discussion of the effect of the gaps on the distribution of data is presented in the next Chapter.

- To properly associate the detected muons to the bunch crossing they belong to, the time windows of 25 ns, in which the signal is collected, need to be shifted in order to take into account the time

of flight of the particles. This means that the times, in which a backward going cosmic track hits the Muon stations, have a reverse order. The time needed for a cosmic muon to cross the entire Muon Detector, with the reverse timing, may not be fully enclosed in the 25 ns time window. To be able to also detect backward going cosmic tracks the time window has been enlarged to five or seven consecutive bunch crossings, depending on the run.

All these features, also including the trigger based on the calorimeters, affect the distribution of the acquired cosmic rays, and the results of the alignment show characteristics that may depend on that. A better insight on the detection of cosmic rays could be obtained studying a Monte Carlo simulation

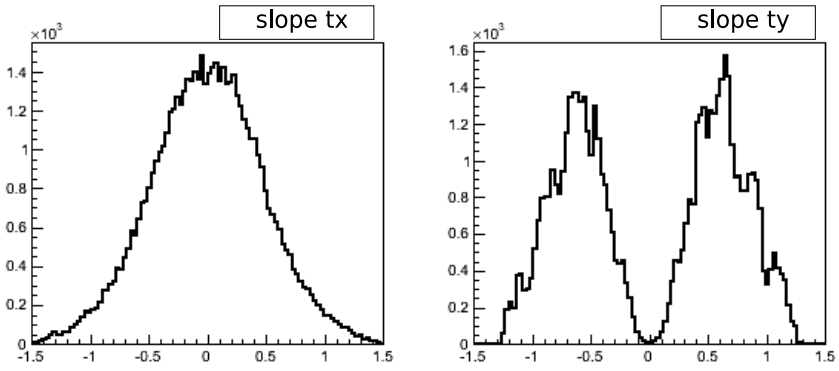

Figure 6.2: The slope distribution of cosmic tracks in (xz) (left) and (yz) (right) plane.

6.3 Data sample selection and reconstruction

The track reconstruction algorithm previously discussed and used with Monte Carlo muons was developed for the track coming from the interaction point, thus it was not suited for the reconstruction of cosmic

tracks. Therefore a different algorithm, belonging to the `MuonNNet` package, was adopted. It was developed for the cosmic track reconstruction in the on-line monitoring of the detector during the cosmic data acquisition.

This algorithm is based on the neural network approach [53, 54]. All the hits in an event are connected by segments (*neurons*). A weight is assigned to the segments based on the angle they form one with respect to the other. The neurons with the smaller relative angles (more aligned to form a straight line) are chosen to build a track. Subsequently a linear track fit is performed, separately in the (x, z) and (y, z) planes.

With this algorithm the tracks were selected for the reconstruction only if they hit at least three out of the four operating stations, in order to reduce most of the combinatorial background. The three stations hit were allowed not to be adjacent, to take into account the inefficiencies in the detection of the hits. In fact, the staggering of chambers on the supporting walls does not assure the total coverage of the detector for any value of particle slope. So that it may happen that cosmic rays pass through the gaps between the chambers of a stations.

The slope distribution of the reconstructed tracks is shown in Figure 6.2. In the right plot the two peaks correspond to the forward ($t_y < 0$) and backward ($t_y > 0$) going cosmic tracks.

The effect on the data collection of the staggering of the chambers on the support walls could be evidentiated with a Monte Carlo simulation, as discussed later on.

In addition, a cut on the track χ^2 of 20 was applied in order to have good tracks.

6.4 Cross Talk

As previously mentioned, the cross talk produces hits that have to be recognised and taken into account not to bias the track reconstruction with fake tracks. For the cosmic rays the cross talk correction is handled with a different strategy from that adopted for the Monte Carlo single muons. In fact in the `MuonNNet` package, after the tracks are built, a

check is performed to retrieve the cross talk hits. The hits found within a distance of $3/2$ of the pad size with respect to the track, are associated to the track itself as cross talk hits.

6.5 Local alignment with Histogram Based method

For the local alignment a system of reference has to be set by fixing two stations. The study was made with three different couples of stations fixed, namely M2-M4, M2-M5, and M3-M5.

As mentioned, in this method the tracks are defined as straight lines connecting hits on the reference stations. The residuals are defined as the distance between the hits and the extrapolated straight line, on the free stations

$$Res\, w = w_{hit} - w_{extrap}\ , \quad \text{where} \quad w = x,\, y\,. \tag{6.1}$$

This procedure is made independently in the (x, z) and (y, z) planes. Only translations along x and y were studied.

The results obtained are listed in Table 6.2. The values of the x alignment parameters are all far form the expected position for more than 3σ. The x and the y parameters are variable with the system of reference. In particular, when M4 is fixed M5 A side shows a displacement of 6.3 mm, while when M5 is fixed M4 A side is displaced by -5.6 mm (M2-M5 fixed) and -4.2 mm (M3-M5 fixed). This seems to show a correlation between the mis-alignment in x of M4 A side and M5 A side. Because of the correlation between M4 A side and M5 A side, this local alignment does not give indications whether one half-station is mis-aligned and which between M4 A side and M5 A side, or both.

In Figure 6.3 the mean residual x and y distributions ($Res\, x$ and $Res\, y$) on the stations M3 and M4, A and C sides, are plotted as a function of x and y respectively, with M2 and M5 as reference stations. In both plots the distributions assume an approximate lying-S-shape,

M2 M4 fix	$Tx\ (mm)$	$Ty\ (mm)$
M3 A	-0.4 ± 0.1	-0.0 ± 0.3
M3 C	-0.6 ± 0.1	$+0.2 \pm 0.3$
M5 A	$+6.3 \pm 0.5$	-3.4 ± 0.6
M5 C	$+2.9 \pm 0.4$	-1.1 ± 0.6
M2 M5 fix		
M3 A	-2.9 ± 0.2	$+1.2 \pm 0.5$
M3 C	-1.2 ± 0.2	$+0.4 \pm 0.5$
M4 A	-5.6 ± 0.3	$+1.8 \pm 0.4$
M4 C	-3.1 ± 0.3	$+0.3 \pm 0.4$
M3 M5 fix		
M2 A	$+3.4 \pm 0.3$	-1.8 ± 0.7
M2 C	$+1.3 \pm 0.2$	$+0.4 \pm 0.6$
M4 A	-4.2 ± 0.3	$+1.1 \pm 0.5$
M4 C	-2.3 ± 0.3	$+0.1 \pm 0.4$

Table 6.2: **Histogram Based method -** Alignment constants for translations in x and y, in the three systems of reference. The alignment parameters are expressed in the local system of reference and calculated with respect to the survey measurements, listed in Table 3.3 of Section 3.

as in Figure 6.6. The different colours represent the different regions (R1÷R4) of the station in which the straight track is extrapolated, *i.e.* in which the residual is computed. The detailed analysis of the residuals evidentiated that the distribution of tracks over a station is not uniform, and it is progressively less uniform and asymmetrical approaching the border of the station, thus producing the observed lying-S-shapes. In the following Chapter the lying-S-shapes and other features like the jumps in y, are discussed.

6.6 Local alignment with Kalman filter fit

For the alignment, the cosmic tracks were selected requiring to have a track reduced χ^2 less than 2.5 in order to assure reliable tracks. Only the tracks lying in the same half of the detector (non overlapping tracks) were chosen to independently align the half-stations. From a total of $680,000$ triggered events, $130,000$ tracks were so obtained.

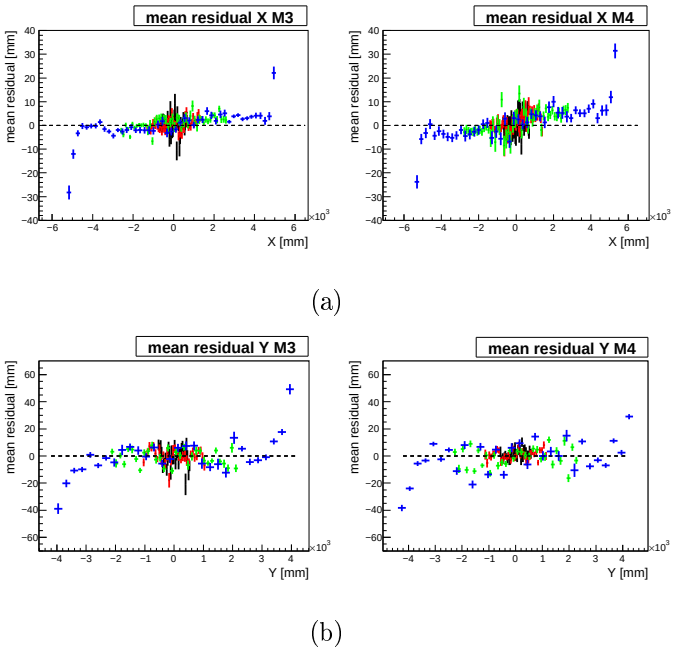

Figure 6.3: **Histogram Based method -** Residual distribution in x (a) and y (b) on M3 and M4 stations A (black) and C (red) sides obtained assuming M2 and M5 stations in their nominal position.

The initial alignment conditions were the survey measurements performed on the four stations that were installed at the time of the acquisition and reported in Table 3.3 of Chapter 3.

As already mentioned, for a local alignment it is necessary to set a system of coordinates, fixing two stations as reference. Here three systems of reference were chosen, fixing in turn the couples of stations M2-M4, M2-M5 and M3-M5.

Initially only translations in x and y were considered, while in a second stage also the rotations of the half-stations around the z axis was introduced.

6.6.1 Results

The resulting alignment constants for translations along x and y, listed in Table 6.3, are of difficult interpretation since all the values are not compatible with the expected postitions within 3σ. In all the three

different couples of stations fixed, an overall pattern can be seen considering that all the station C sides are better aligned than the A sides and that along y the displacements are smaller than along x.

With M2-M4 fixed, a large displacement is shown for the M5 A side, that appears to be open by 11 mm, as similarly detected in the Histogram Based method. Keeping M5 fixed, together with M2 or M3, its misalignment reflects on the misalignment of the free A side half-stations. In particular, when M5 is fixed together with M2, so that the free half-stations are comprised between them, the displacement shown by M4 is larger with respect to when M3 is fixed together with M5.

The y displacements for all the half-stations in A and C side are quite small except for M5 A side, that apperas to be lower of 3.4 mm from the expected position.

The errors are roughly larger by a factor of 10 compared with the errors on the global alignment constants obtained with the Monte Carlo single muons, even though the number of tracks used is comparable. However, in this case the tracks hit mainly the outermost regions of the stations, where the granularity is larger.

The results obtained when also the rotations around the z axis are introduced are listed in Table 6.4. The values of the alignment constants do not change sensibly since the values of the rotations are compatible with zero.

The displacements so far observed can be either interpreted as an actual displacements, or as a shearing in the (x, z) plane together with a displacement of M5 along the x direction, while with the Histogram Based method two stations, M4 and M5, look mis-aligned.

To gain a better picture on the M4 position, a further check aligning M4 and M5 with respect to the frame of reference set by fixing M2 and M3 was tried. The results listed in Table 6.5 show a large mis-alignment of M5 A side, together with a small mis-alignment of M4 A side and M5 C side. However is this case, a sensible mis-alignment along y appears.

With a local alignment performed either with the Kalman filter fit

M2 M4 fix	Tx (mm)	Ty (mm)
M3 A	$+0.7 \pm 0.1$	$+0.5 \pm 0.3$
M3 C	-0.1 ± 0.1	-0.4 ± 0.2
M5 A	$+11.0 \pm 0.3$	-3.4 ± 0.5
M5 C	$+2.8 \pm 0.3$	-1.2 ± 0.5
M2 M5 fix		
M3 A	-2.5 ± 0.1	$+1.1 \pm 0.3$
M3 C	-0.8 ± 0.1	-0.3 ± 0.3
M4 A	-6.1 ± 0.2	$+1.1 \pm 0.4$
M4 C	-0.6 ± 0.2	$+0.2 \pm 0.4$
M3 M5 fix		
M2 A	$+3.0 \pm 0.2$	-0.2 ± 0.3
M2 C	$+0.7 \pm 0.2$	$+1.1 \pm 0.3$
M4 A	-4.5 ± 0.2	$+0.5 \pm 0.5$
M4 C	$+0.1 \pm 0.2$	$+0.4 \pm 0.5$

Table 6.3: **Kalman filter fit method -** The alignment constants for translations in x and y, in the three systems of reference. The alignment parameters are expressed in the local system of reference and calculated with respect to the survey measurements, listed in Table 3.3 of Section 3.

method either with the Histogram Based method, a mis-alignment of M4 and M5 is obtained. However, a confirmation that these results are not dependent on the frame of reference used, can only be provided by a global alignment. In any case, since made with experimental data, these first attempts of alignment seem capable to point out information on the actual state of the detector, in spite of the limit of the local alignment and of the particles unsuited to the geometry of the Muon System.

6.6.2 Tentative global alignment

As a premise of a relative alignment between the Muon detector and the Outer Tracker, a study of the residuals between the Muon and the OT cosmic segments was carried on.

The OT segments are reconstructed by the `PatSeeding` algorithm [55] with options for the reconstruction of cosmics, thus for example the drift times are not used. The track state vector of OT segment closest to

M2 M4 fix	$Tx\ (mm)$	$Ty\ (mm)$	$Rz\ (mrad)$
M3 A	$+0.7 \pm 0.1$	$+0.6 \pm 0.3$	$+0.19 \pm 0.06$
M3 C	$+0.1 \pm 0.1$	-0.5 ± 0.3	-0.01 ± 0.06
M5 A	$+10.9 \pm 0.3$	-2.9 ± 0.6	$+0.35 \pm 0.13$
M5 C	$+2.7 \pm 0.3$	-1.1 ± 0.5	$+0.15 \pm 0.13$
M2 M5 fix			
M3 A	-2.5 ± 0.1	$+1.1 \pm 0.3$	$+0.01 \pm 0.07$
M3 C	-0.8 ± 0.1	-0.3 ± 0.3	-0.04 ± 0.07
M4 A	-6.0 ± 0.2	$+0.9 \pm 0.4$	-0.24 ± 0.11
M4 C	-0.6 ± 0.2	$+0.2 \pm 0.4$	-0.01 ± 0.11
M3 M5 fix			
M2 A	$+3.0 \pm 0.2$	-0.4 ± 0.5	-0.16 ± 0.11
M2 C	$+0.7 \pm 0.1$	$+1.1 \pm 0.5$	-0.04 ± 0.11
M4 A	-4.4 ± 0.2	$+0.3 \pm 0.3$	-0.21 ± 0.10
M4 C	-0.1 ± 0.2	$+0.4 \pm 0.3$	$+0.04 \pm 0.10$

Table 6.4: **Kalman filter fit method -** The alignment constants for translations in x and y and rotations around the z axis, in the three systems of reference. The alignment parameters are expressed in the local system of reference and calculated with respect to the survey measurements, listed in Table 3.3 of Section 3.

M2 is extrapolated downstream to the z of the first track state vector of the Muon cosmic segment, in a match procedure analogous to that used to match the long and muon track segments for the global alignment with the Monte Carlo single muons. The bad matched tracks are here discriminated with a loose cut on the matching χ^2 at 100. Then among the OT segments that possibly match a muon segment, the one with the best matching χ^2 is chosen.

After the matching, the distributions of the residuals between the two segments of tracks were studied. The residuals are defined as

$$Res\, w = (w_{ot} - w_{muon})|_{refz} \quad \text{, where } \; w = x,\, y,\, tx,\, ty\,. \tag{6.2}$$

These residuals are examined plotting them as function of the coordinates and slopes of the Muon segment at the reference z (Figure 6.4).

Neglecting some effects at the border of the acceptance, that in general occur with a high error, most of these distributions are flat, a few of

M2 M3 fix	$Tx\ (mm)$	$Ty\ (mm)$
M4 A	-1.9 ± 0.2	-3.4 ± 0.4
M4 C	$+0.3 \pm 0.2$	-1.5 ± 0.4
M5 A	$+6.9 \pm 0.3$	-7.5 ± 0.7
M5 C	$+1.9 \pm 0.3$	-3.6 ± 0.7

Table 6.5: **Kalman filter fit method -** The alignment constants for translations in x and y, in the system of reference set by fixing stations M2 and M3. The alignment parameters are expressed in the local system of reference and calculated with respect to the survey measurements, listed in Table 3.3 of Section 3.

them are lying-S-shaped, others are irregular. In particular, the distributions in plots 8 and 16 seem splitted in two parts.

The distributions so obtained did not allowed a straightforward interpretation. This difficulty suggested a check with another detector. To check whether the unexpected distributions could be related to a misalignment between the Muon Detector and OT, the same test was made with the calorimeters. The muon cosmic segments were matched with the cosmic segments reconstructed by the calorimeters.

The calorimeter track reconstruction is performed by a dedicated tool that combines the position of the deposits of energy in both the electromagnetic and hadronic calorimeters. Even if the calorimeter resolution is necessarily poor since they are not tracking detectors, the test yields some interesting indications. In this case for not degrading even more the resolution on the calorimeter segments, the z position of the calorimeter segment state closest to the station M2 is taken as reference, and the first state of the muon segment is extrapolated upstream at that z. The definition of the residual is the same as before, and also in this case the residuals are plotted as function of the coordinates and the slopes of the muon segment at that reference z. In this case only one segment reconstructed in the calorimeters corresponds to a muon segment, so no χ^2 cuts are applied.

Since calorimeters triggered most of the cosmic rays acquired by the Muon Detector, a very high statistics was available for the match. It is actually a factor ~ 10 higher than in OT. In the distributions shown in

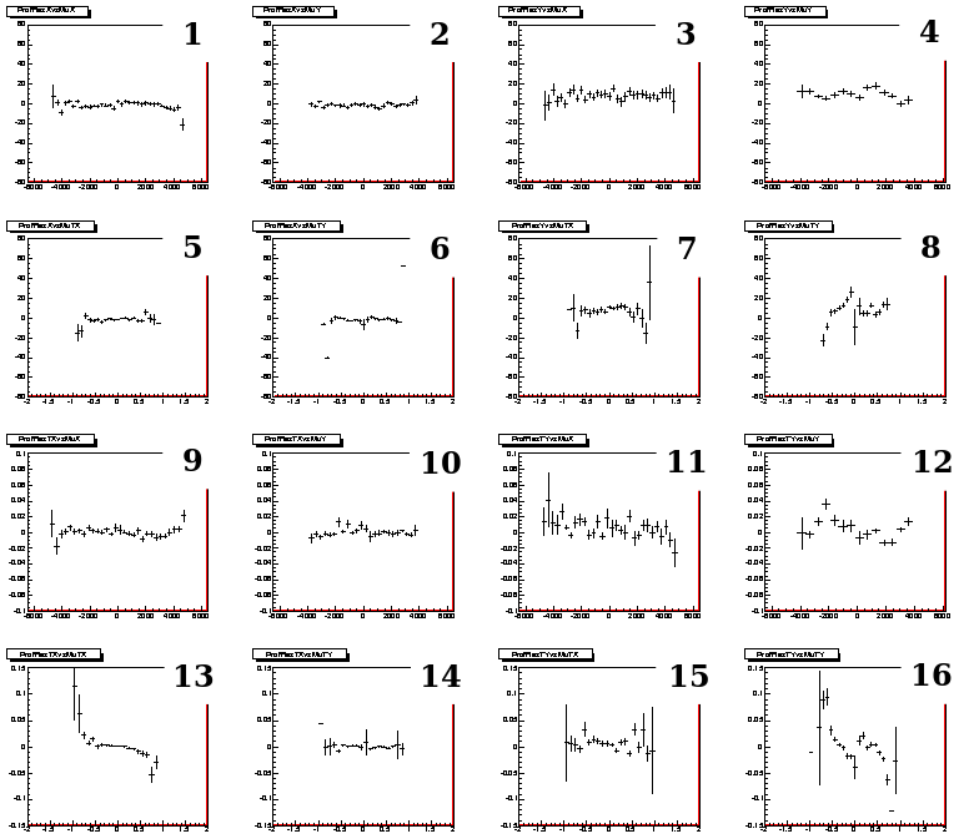

Figure 6.4: Residuals between Outer Tracker and muon cosmic segments versus coordinates and slopes of muon segments at the reference z. First row: x and y coordinate residuals versus x and y; second row: x and y residuals versus slopes tx and ty; third row: tx and ty residuals versus x and y; fourth row: tx and ty residuals versus slopes tx and ty.

Figure 6.5, the same patterns previously obtained for OT can be recognised, although more visible. Since the distributions of the residuals were considered more reliable, some correlations were attempted. The flat patterns appear when the residual is plotted versus a variable external to the residual itself ($Res\,x$ vs y, $Res\,y$ vs x, $Res\,x$ vs t_y, $Res\,y$ vs t_x, $Res\,t_x$ vs y, $Res\,t_y$ vs x, $Res\,t_x$ vs t_y, $Res\,t_y$ vs t_x) as in the eight plots of the two central column of Figure 6.5. The others show approximately a lying-S-shape. In addition, when the slope t_y is involved (plot 6, 8, 14, 16) it is visible a discontinuity around the value $t_y = 0$.

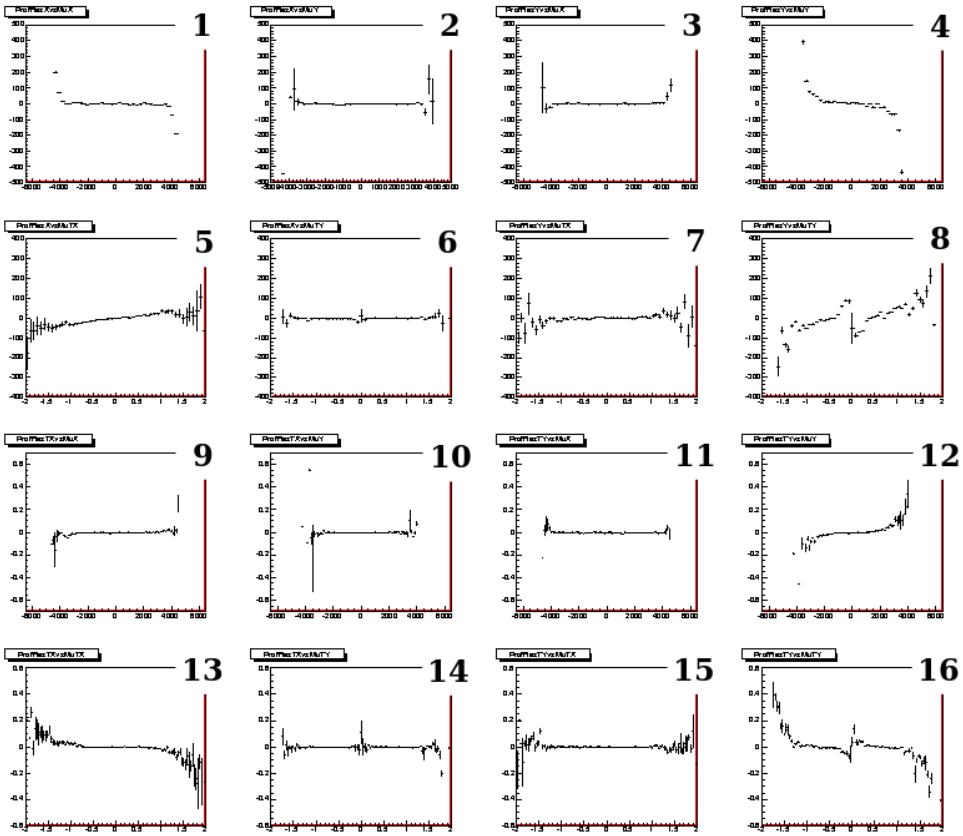

Figure 6.5: Residuals between calorimeter and muon cosmic segments versus coordinates and slopes of the muon segment state at the z taken as reference. First row: x and y coordinate residuals versus x and y; second row: x and y residuals versus slopes tx and ty; third row: tx and ty residuals versus x and y; fourth row: tx and ty residuals versus slopes tx and ty.

The lying-S-shapes of the plots in Figure 6.5 were found similar to the lying-S-shape in Figure 6.6. Although this figure refers to the Monte Carlo cosmics dealt with the Histogram Based method, it is however illustrative of the mechanism that generates the lying-S-shapes. It shows the residuals between the y coordinate of the Monte Carlo hit (continuous distribution) and the y coordinate of the corresponding pad hit (y position of the readout element): $Res\,y = y_{pad} - y_{MonteCarlo}$. The distribution of the particles over a station is not uniform at the borders of the stations, because of their geometry and acceptance, and because the pad

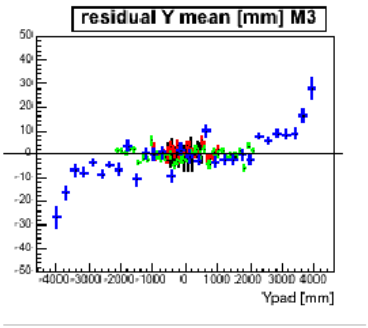

Figure 6.6: Residuals between the y coordinate of the Monte Carlo hit and the y coordinate of the corresponding pad hit. It is illustrative of the mechanism that generates the lying-S-shapes in Figures 6.4 and 6.5

dimension increases getting far from the centre of the station. Thus the mean of the distribution of the y position of the Monte Carlo hits over a pad is progressively small than the y position of the centre of the pad itself.

Also the discontinuities in plots 6, 8, 14, 16, where the residuals are plotted as function of the vertical slopes t_y, were found to depend on the absence of horizontal tracks, that is proper of the cosmic rays.

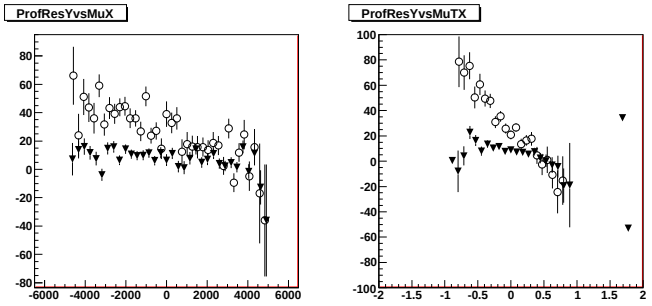

Figure 6.7: Comparison of plots 3 and 7 of Figure 6.4 before (emtpy dots) and after (triangles) correction.

However, comparing the two matches, OT-Muon and Calo-Muon, in the former there still was some effects not completely similar in the distributions of the residuals $Res\,y$ vs x, where the mean is $9\ mm$ (plots

3 in Figures 6.4 and 6.5); the residuals $Res\,y$ vs t_x with the same value of the mean (plots 7); the residuals $Res\,y$ versus t_y where the two parts of the distribution, at negative and positive x, have two different slopes (plots 8); the residuals $Res\,t_y$ versus y where two smooth peaks appear at $y =\sim \pm 2$ m (plots 12).

Carying on this study on the distributions of residuals, some inaccuracies could be detected. Their correction was not resolutive, though an improvement in the residual distributions was obtained, Figure 6.7.

OT-Muon relative alignment within Kalman filter fit method

With the tracks matched as in the residual study, the relative alignment of the Muon Detector with respect the Outer Tracker was performed with the Kalman filter fit method. The resulting alignment constants are shown in Figure 6.8. A displacement along x up to 6 mm is visible for all the M2÷M5 half-stations, together with a huge and progressive displacement along y, especially in the C side of the detector. These results can not be considered reliable given the too large mis-alignments they suggest, and some more work is still in course.

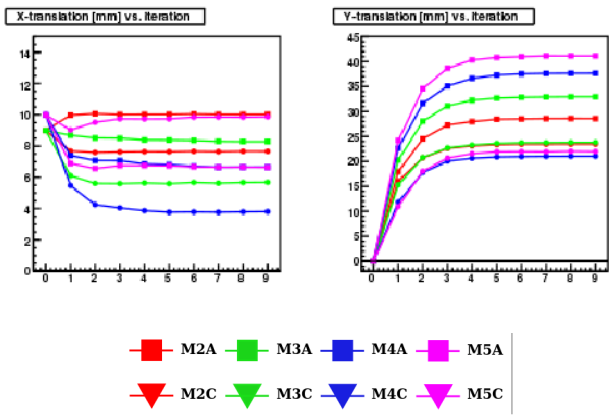

Figure 6.8: The flow of alignment constants of the alignment for translations along x and y of the Muon Detector half-stations form M2 to M5, with respect to the OT.

Here, as already experienced in all the phases of the alignment study of the Muon Detector, the main difficulties do not reside in solving big

problems, but in detecting many small imprecisions that could be easily and readily solved the moment they were identified.

The attempts of relative alignment between OT and the Muon Detector seem to enlarge the field of investigations on small irregularities.

6.7 Conclusions

With the first real cosmic ray data available for the Muon Detector and the Outer Tracker the local alignment of the Muon Detector was performed either with the Kalman filter fit method either with the Histogram Based method. In both cases a mis-aligment of stations is detected. An attempt of relative alignment between the Muon Detector and OT was made. A preliminary work was carried out studying the distribution of residuals between the track segments reconstructed in both the detectors. The alignment procedure, however, did not give reliable results.

Chapter 7

Local alignment with Monte Carlo cosmic rays

In this chapter the results on the alignment performed on two Monte Carlo samples of cosmic muons are presented. They have been produced in order to validate the alignment procedure used with real cosmic rays and to study any possible systematics related to the Muon Detector. The muons are simulated only in the Muon Detector, so that the alignment can only be local. Three pairs of stations, M2-M4, M2-M5, and M3-M5, are in turn supposed to be in their nominal position and fixed to set the local system of reference.

7.1 Simulation

Two samples of Monte Carlo cosmics were simulated, digitised and reconstructed, one with the nominal geometry of the detector elements, and the second with the M5 station misaligned along x (A side opened by 4 mm and C side opened by 2 mm).

The two samples are simulated with the `CosmicsGun` algorithm [56]. According to previous studies [57], the distribution of momentum and polar angle of the cosmic muon at any shallow depth (less than few

hundreds of meters of water equivalent) is parametrised by

$$I(p_\mu, \theta) = \cos^3\theta I_V(p_\mu \cos\theta) \tag{7.1}$$

where θ is the polar angle and I_V the intensity of vertical cosmic muons of momentum p_μ. Thus the cosmic muons generated on a station surface have momentum and polar angle assigned according to Eq. (7.1).

Because the Gauss project allows to follow a particle from the moment of its generation on, a muon generated on the surface of a station, M2 for instance, is followed only forwards, *i.e.* towards station M5, loosing track of what happend before M2. To overcome this feature the particles are then tracked back to a horizontal plane on top of the detector at $y = +6$ m and from there generated down-going (Figure 7.1). The Monte Carlo cosmics then will always have an origin at $y = +6$ m, with different z and x, depending on which station the generation is devised [56].

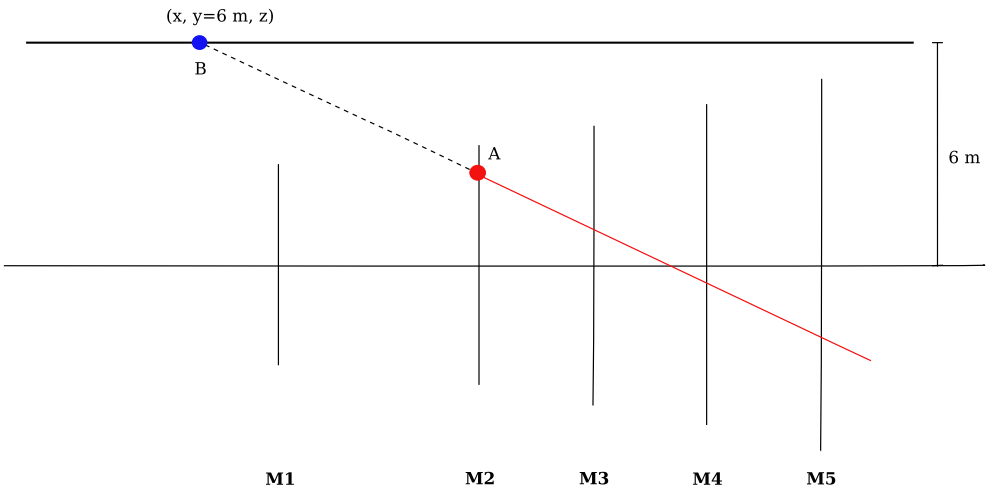

Figure 7.1: The geometry of the Monte Carlo cosmic muons generation. The particle A generated on a station surface, M2 for instance, has momentum and polar angle assigned according to the distribution in Eq. (7.1). It is tracked back towards an horizontal surface at $y = 6$ m (black dashed line). B is now the new origin of the trajectory.

However, the horizontal plane at $y = +6$ m from which the cosmics

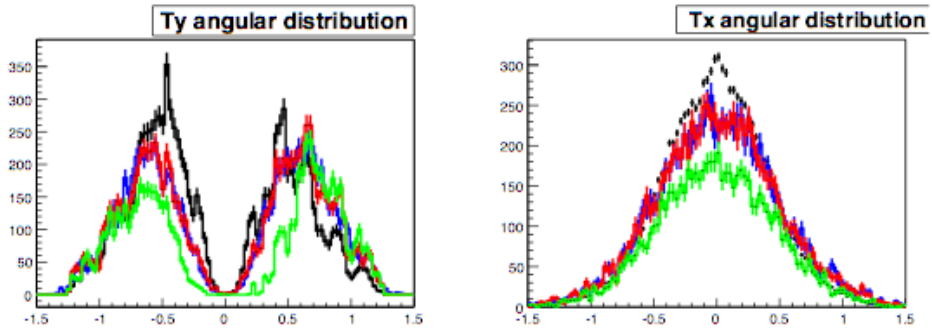

Figure 7.2: Angular distributions of cosmic tracks in (y, z) (left) and (x, z) (right) planes. Real cosmic rays (black) and Monte Carlo generated with three different dimensions of the horizontal plane placed at $y = +6$ m: in green the original plane, in red and in blue the differently enlarged planes.

muons are generated had to be enlarged with respect to the original version of the algorithm in order to include particles with smaller vertical slope. In fact a check on the angular distribution of the Monte Carlo cosmics produced with the original settings of the algorithm showed a loss of muons with small slopes compared to the real data. In Figure 7.2 the angular distributions are shown. The distributions of real data are plotted in black, and the distributions of Monte Carlo cosmics produced with the original settings of the algorithm `CosmicsGun` in green. It is visible that the two distributions are not compatible in the region of small slopes. In the plots the angular distributions of Monte Carlo cosmics produced with two differently enlarged horizontal planes are also superimposed (red and blue). As can be seen the difference between the two distributions is negligible but both are in better agreement with the distributions of real data.

The samples here discussed are a merge of Monte Carlo cosmics simulated on the surface of M2, M3 and M4 stations. For each station $500,000$ particles are generated, so that the two samples (aligned, and M5 mis-aligned along x) have a total of 1.5 million of muons each.

In the subsequent phase of the production of Monte Carlo cosmics - the digitisation phase in which the response of the detector and its

imperfections are simulated - cross talk and electronic noise are added. However, during the acquisition the thresholds of the muon chambers were modified from the nominal ones in order to adjust the detector to the collection of the cosmic rays, thus the simulated noise and cross talk can be slightly different from that in the acquired data. In addition, dead logical channels were not simulated.

7.2 Track reconstruction and study of systematics

In order to make a comparison with the acquired cosmic rays, the Monte Carlo samples were reconstructed with the same algorithm and the same configurations used for the real data, *i.e.* without the information of the hits in M1, since during the data taking this station was not in place. Some other requirements were then used in the selection of tracks for the alignment analysis.

The Monte Carlo cosmic muons have been generated according to the conditions previously discussed with the algorithm `CosmicGun` with an uniform spatial distribution over a station. The slope distributions of the simulated muons are reported in red in Figure 7.2, and compared with the slope distributions of the real cosmic rays, in black.

The track reconstruction, with its implicit or explicit requirements, changes the initial uniform distributions. An implicit condition is the trajectories to cross the Muon stations, so that the geometrical acceptance of the detector affects their distributions. In addition, it is required the track extrapolation to lie in the calorimeter volumes, to mimick the trigger used for the acquisition. Moreover, at least three stations hit are required to reconstruck a track. This means that if by chance a track misses two stations of the detector passing in a gap between chambers because of its slope, the track is not reconstructed and the gap is "projected" onto the other stations.

Once the tracks are reconstructed with the hit pads - *i.e.* on top of the continuous distribution of the Monte Carlo hits the "filter" of the readout

granularity is applied - and satisfy the requirement of having at least three stations hit and to lie in the calorimeters, the x and y distributions of the Monte Carlo hits associated to the tracks are plotted. These distributions are reported in Figure 7.3. The upper row contains the plots of the x distributions over the four stations M2÷M5, and the lower row the y distributions. A pattern of alternate peaks and holes is visible. In the x Monte Carlo hit distribution (upper row of plots) the four peaks and the four holes should correspond to the eight columns in which the chambers are arranged on the supporting walls along the x axis (Figure 3.3 in Chapter 3). More precisely, the loss of hits should correspond to the chambers in position $z_{1,4}$. In the y Monte Carlo hit distribution (lower row of plots) the sixteen peaks and the sixteen holes should correspond to the thirtytwo chambers mounted in the same column, sixteen in front and sixteen on the back of the supporting walls.

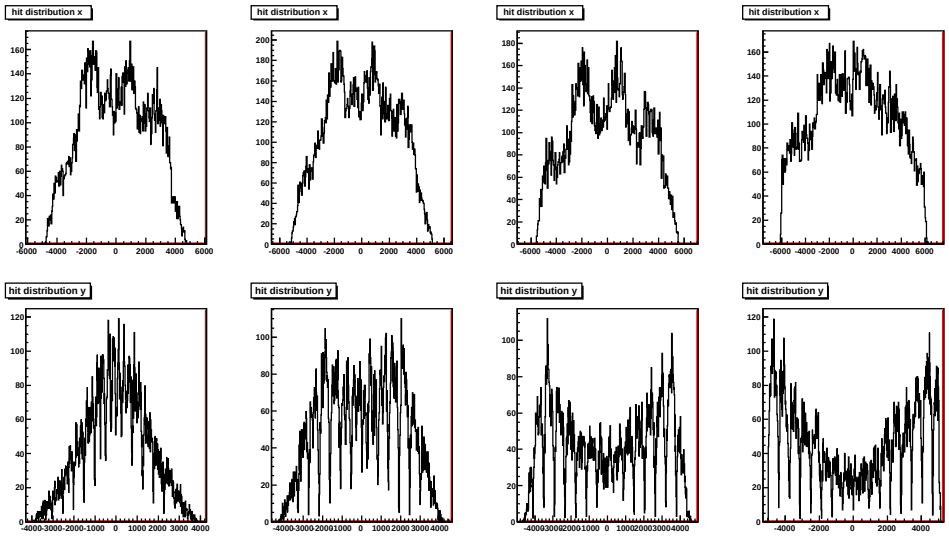

Figure 7.3: The distribution of Monte Carlo hits on the Muon stations M2-M5. The plots in the first row refer to the hit distribution in x, while the bottom row plots to the hit distribution y. The staggering in z of the chambers and the requirement that the tracks pass through the calorimeters affect the initial uniform distribution.

In addition, while the distribution with which the Monte Carlo cosmics are generated is uniform on the surface of the stations (M2, M3, M4),

it roughly assumes peak and concave shapes by the requirement of the tracks to pass through the calorimeters. In Figure 7.4 it is schematically depicted the geometrical acceptance of the Muon Detector for backward going cosmic tracks, either the calorimeters are taken into account or not. The situation is almost symmetrical for forward going tracks.

Tracks crossing the M5 station at the upper y edge have a large interval of vertical slopes t_y available to reach M2 - from the more horizontal slopes that allow to reach M2 at the upper edge, to the more vertical slopes that allow to reach M2 at the lower edge - while tracks crossing M5 in the central y area have less slopes available and thus less probability to reach M2 anywhere.

The requirements for the tracks to cross the calorimeters reduce even more these intervals of slopes cutting the more vertical slopes. So that tracks in the M5 y central area have a very small interval of slopes available and thus less probability to be selected, but also the tracks reaching M2 at the y edges are too inclined to reach the calorimeters. This geometrical selection results in a modification of the initial flat distributions to the shapes in Figure 7.3. Rough peaks are so found for M2 and M3 stations, while concavities are found for M4 and M5.

This effect can be also shown dividing the y hit distribution in four intervals of vertical slopes $t_y = dy/dz$. The plot in Figure 7.5 shows that some regions of the detector are accessible only for large values of the t_y slope.

The effects of this irregular geometrical acceptance then reflect on the distributions of the residuals. Figure 7.6 shows the residuals between the hit (pad centre coordinates, discrete distribution) and the corresponding Monte Carlo hit (continuous distribution)

$$Res\, w = w_{hit} - w_{MC}\,, \quad \text{where} \quad w = x,\, y \tag{7.2}$$

plotted as function of the hit coordinates x and y. Some of the visible effects (lying-S-shape) have been anticipated in the previous Chapter. The "jumps" of the residual mean values, more evident in the $Res\, y$ vs y distribution on M4 station, are due to the "holes" in the acceptance

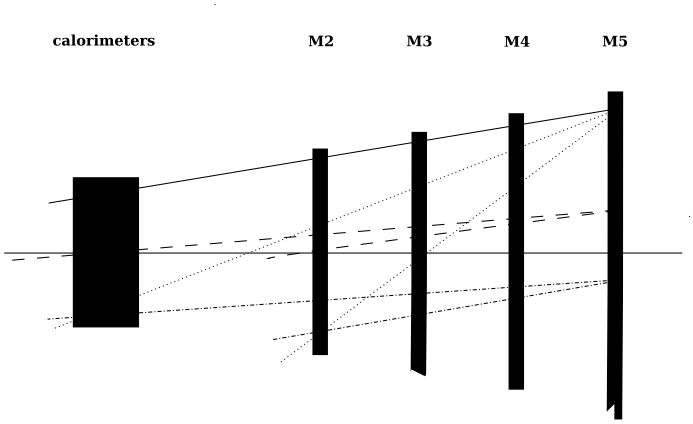

Figure 7.4: A schematic view of the Muon Detector as it is used with the cosmic muons, without the station M1. The lines represent the vertical slope of tracks lying in the acceptance of the detector whether the extrapolation of tracks to the calorimeter volumes is taken into account or not. The slopes of the couples of dashed, dotted, and dash-dotted lines change if the calorimeters are included. The solid line slope is not affected by the presence of the calorimeters. This pattern symmetrically applies to backward and forward cosmic tracks.

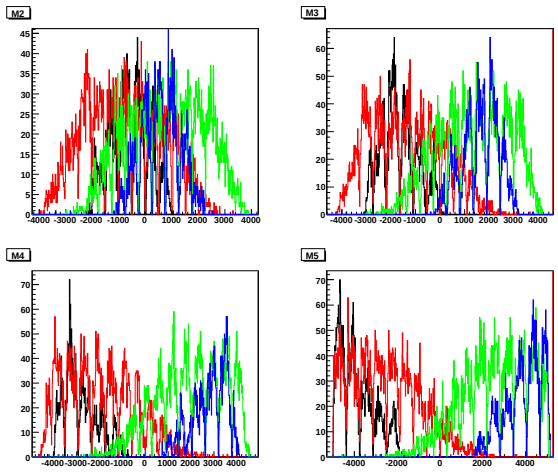

Figure 7.5: The y distribution of Monte Carlo hits associated to the reconstructed tracks on the Muon stations M2-M5. The track $t_y = dy/dz$ slopes have been divided into four intervals: black t_y in $(-1.5, -0.75)$, red t_y in $(-0.75, 0)$, green t_y in $(0, 0.75)$ and blue t_y in $(0.75, 1.5)$.

corresponding to the different chambers in a column mentioned above.

Within the Histogram Based method all these effects can be easily

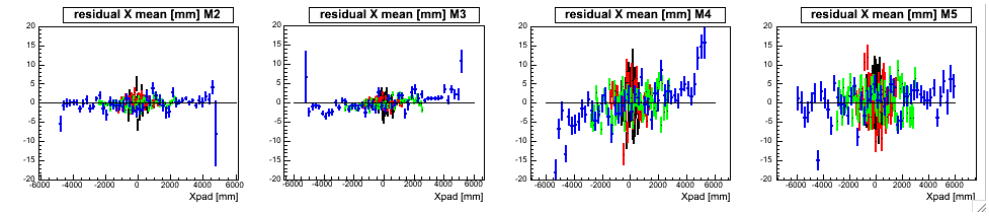

(a)

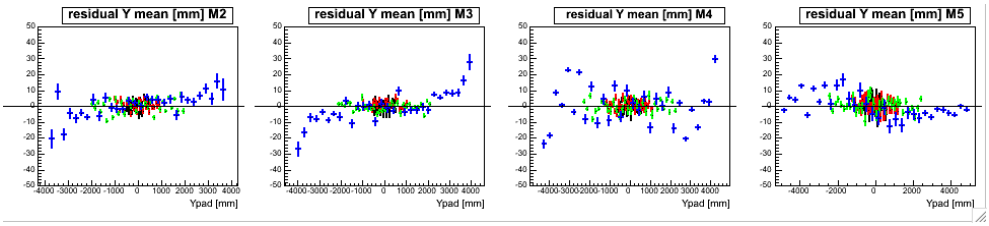

(b)

Figure 7.6: The residuals between the hit and the Monte Carlo hit for (a) x and (b) y, Eq. (7.2).

studied. Having an ideal detector, with a very high spatial resolution, even reconstructing tracks in the naive way of connecting the hits in the two stations fixed to set the frame of reference, would produce a flat mean residual distribution. In Figure 7.7 this ideal scenario is mimicked. The Monte Carlo hits (continuous distribution) are used for the track reconstruction and the residuals plotted are the distance between the Monte Carlo hits on stations M2 and M4, and the tracks reconstructed connecting the Monte Carlo hits in stations M3 and M5. The residuals are

$$Res\, x = x_{MC} - x_{MC-track}\,. \tag{7.3}$$

In Figure 7.8 sampling is progressively introduced: in (a) the tracks are still reconstructed using the Monte Carlo hits in M3 and in M5, however the residuals plotted are now the distance between the track and the hit pad x coordinate (discrete distribution) on the stations M2 and M4

$$Res\, x = x_{hit} - x_{MC-track}\,. \tag{7.4}$$

In (b) the last step towards the real situation is made: the track is

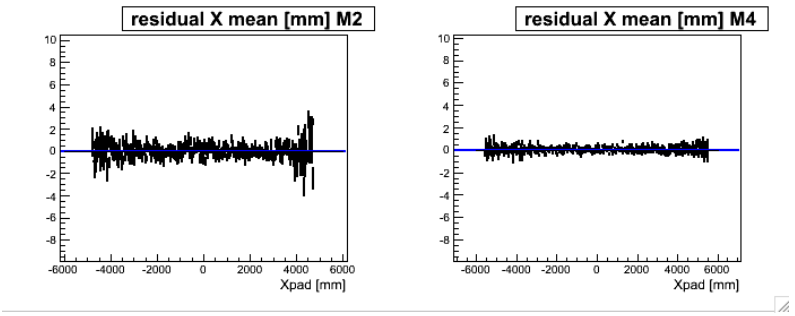

Figure 7.7: **Histogram Based method -** The residuals between the Monte Carlo hits and the track reconstructed with the Monte Carlo hits Eq. (7.3)

now reconstructed with the hit pads in M3 and M5, and the residuals are

$$Res\, x = x_{hit} - x_{hit-track}\,. \tag{7.5}$$

The sampling affects the shapes of the distributions introducing the lying-S-shape, and the jumps between the points along the distributions.

7.3 Local alignment with Kalman filter fit method

7.3.1 Selection

In order to analyse the Monte Carlo cosmics under conditions as close as possible to those used in the analysis of the real cosmics, the further requirements are applied in addition to the exclusion of the information of station M1

- at least three stations hit
- track $\tilde{\chi}^2 < 2.5$
- the extrapolation to lie in the calorimeter volumes.

The first is the basis requirement used for the cosmic rays reconstruction in the Muon Detector to avoid fake tracks made by noise hits.

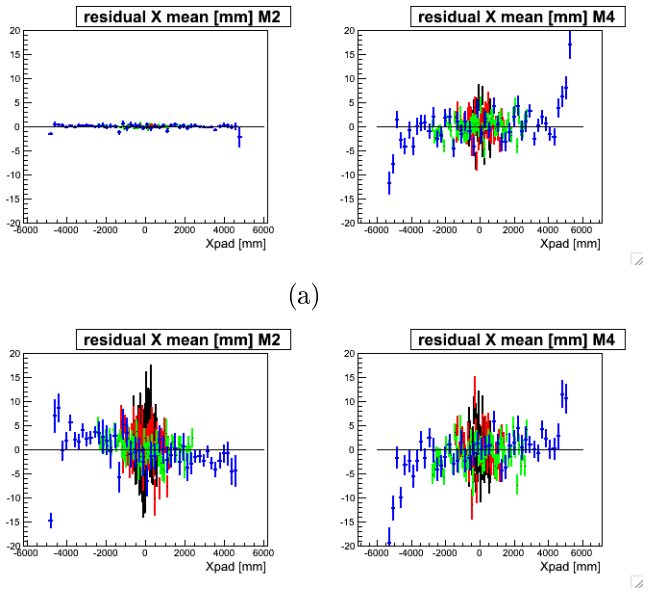

Figure 7.8: **Histogram Based method -** The residuals between (a) the pads hit and the tracks reconstructed with the Monte Carlo hits Eq. (7.4), (b) the pads hit and the tracks reconstructed with the pads hit Eq. (7.5)

The third requirement is applied because the real data are mainly triggered by the calorimeters, so to reproduce the geometrical acceptance of the real tracks.

Only the tracks lying in the same half of the detector (non overlapping tracks) were chosen to independently align the half-stations. In addition, the $\tilde{\chi}^2$ cut assures to have reliable tracks.

Under these conditions only a total of $41,000$ $(44,000)$ tracks in the aligned (mis-aligned) sample are available for the alignment out of the 1.5 million of events.

7.3.2 Results

In this section the results of the alignment performed with different samples and with different degrees of freedom are presented.

Following the procedure used with the real cosmics illustrated in the previous Chapter, the alignment of half-stations for translations along x

and y was made first, and subsequently the rotation around the z axis was added as a degree of freedom.

Being a local alignment, the Muon Detector internal frame of reference is set by keeping fix two stations that are assumed to be in their nominal positions. Three pairs of stations are in turn fixed, M2-M4, M2-M5, and M3-M5.

Aligned sample, translations

- Nominal position of all the half-stations
- alignment for translations along x and y.

The results on the alignment constants of the half stations, listed in Table 7.1, are good. All of them are compatible with the input aligned position within 3σ.

The errors scale with the pad sizes and with the statistics. As already mentioned the x pad dimensions double from stations M2-M3 to M4-M5 and affects the variation of the x errors from one station to the other.

Aligned sample, translations and rotations

- Nominal position of all the half-stations
- alignment for translations along x and y and for rotations around the z axis.

Rotations Rz around the z axis affects the x and y coordinates. In the case under discussion the rotations are compatible with zero, so that the translations along x and y axes do not change significantly with respect to the previous case. The results obtained when the rotations around the z axis is included are listed in Table 7.2.

Mis-aligned sample, translations

The mis-aligned sample was generated to check the sensitivity of the alignment with the cosmic rays in figuring out mis-alignments, and how

M2 M4 fix	Tx (mm)	Ty (mm)
M3 A	-0.1 ± 0.2	0.5 ± 0.5
M3 C	0.0 ± 0.2	0.0 ± 0.5
M5 A	1.5 ± 0.6	-2.0 ± 1.0
M5 C	1.5 ± 0.6	-2.5 ± 1.0
M2 M5 fix		
M3 A	-0.3 ± 0.2	1.2 ± 0.5
M3 C	-0.3 ± 0.2	0.9 ± 0.5
M4 A	-0.2 ± 0.4	1.5 ± 0.7
M4 C	-0.3 ± 0.4	1.7 ± 0.7
M3 M5 fix		
M2 A	-0.1 ± 0.3	-2.0 ± 0.8
M2 C	-0.0 ± 0.3	-1.2 ± 0.8
M4 A	0.3 ± 0.4	0.9 ± 0.6
M4 C	0.1 ± 0.4	1.2 ± 0.6

Table 7.1: **Kalman filter fit method -** The alignment constants for half-stations aligned for translations in x and y, using the sample generated with the nominal geometry. The values are given in the local systems of reference of each half-station.

M2 M4 fix	Tx (mm)	Ty (mm)	Rz $(mrad)$
M3 A	-0.1 ± 0.2	0.5 ± 0.5	0.0 ± 0.1
M3 C	-0.3 ± 0.2	0.2 ± 0.5	0.1 ± 0.1
M5 A	1.5 ± 0.7	-1.8 ± 1.1	0.3 ± 0.2
M5 C	1.8 ± 0.7	-2.5 ± 1.1	0.1 ± 0.2
M2 M5 fix			
M3 A	-0.3 ± 0.2	1.2 ± 0.6	-0.2 ± 0.1
M3 C	-0.7 ± 0.2	1.0 ± 0.6	0.0 ± 0.1
M4 A	-0.3 ± 0.4	1.4 ± 0.7	-0.3 ± 0.2
M4 C	-0.6 ± 0.4	1.7 ± 0.7	-0.2 ± 0.2
M3 M5 fix			
M2 A	-0.1 ± 0.3	-2.0 ± 0.8	0.3 ± 0.2
M2 C	0.5 ± 0.3	-1.4 ± 0.8	0.0 ± 0.2
M4 A	0.2 ± 0.4	0.9 ± 0.6	-0.2 ± 0.2
M4 C	0.0 ± 0.4	1.1 ± 0.6	-0.2 ± 0.2

Table 7.2: **Kalman filter fit method -** The alignment constants for half-stations aligned for translations in x and y and rotations around the z axis, using the sample generated with the nominal geometry. The values are given in the local systems of reference of each half-station.

the mis-alignment of one station taken as reference affects the alignment of the other elements.

- M5 A side opened by 4 mm, M5 C side opened by 2 mm, and the other half-stations in their nominal positions

- alignment for translations along x and y.

In the case where the halves of M2 and M4 are fixed the alignment constants reproduce the displacement with which the station M5 has been simulated. The other two pairs of stations fixed contain M5, so that its displacement affects the alignment constants of the aligning elements. The results obtained, listed in Table 7.3, show an apparent shearing of the other stations.

M2 M4 fix	Tx (mm)	Ty (mm)
M3 A	-0.5 ± 0.2	-0.1 ± 0.4
M3 C	-0.3 ± 0.2	0.4 ± 0.4
M5 A	3.8 ± 0.6	0.7 ± 0.9
M5 C	2.1 ± 0.6	-1.0 ± 0.9
M2 M5 fix		
M3 A	-1.6 ± 0.2	-0.2 ± 0.5
M3 C	-0.7 ± 0.2	0.6 ± 0.5
M4 A	-2.5 ± 0.4	-0.3 ± 0.6
M4 C	-1.0 ± 0.4	0.2 ± 0.6
M3 M5 fix		
M2 A	1.3 ± 0.2	-0.2 ± 0.7
M2 C	0.0 ± 0.2	-0.1 ± 0.7
M4 A	-1.0 ± 0.3	-0.1 ± 0.6
M4 C	-0.0 ± 0.3	-0.1 ± 0.6

Table 7.3: **Kalman filter fit method -** The alignment constants for half-stations aligned for translations along x and y, using the sample generated with the M5 station A (C) side shifted of 4 (2) mm along x. The values are given in the local systems of reference of each half-station.

7.4 Conclusions

The procedure adopted for the local alignment of the Muon Detector with real cosmic rays is here tested with Monte Carlo simulated cosmic muons using the Kalman filter fit method. The half-stations have been aligned for translations along x and y, and for rotations around the z axis, with data simulated with the nominal position of the half-stations. With the sample simulated with a mis-alignment, namely M5 A (C) side opened by 4 (2) mm, the half-stations have been aligned for translations along x and y axes. The results of all the alignment were satisfactory. Moreover, the systematics related to the detection of the cosmic rays by the Muon Detector have been studied with the Histogram Based method. The sampling was found to affect the shapes of the residual distributions producing lying-S-shapes and jumps between the points along the distributions.

Conclusions

The software procedure to align the Muon Detector, locally and globally, has been carried out.

Specific algorithms for the track finding and reconstruction in the Muon Detector were developed. The reconstructed tracks are now in the standard LHCb format and the tracks are fitted with the default Kalman filter fit. A pad clusterization has been chosen and implemented to take into account the cross talk in the detector. The default simulation of multiple scattering in the LHCb framework has been studied in order to find the better conditions for the Muon Detector.

The alignment procedure was tested by Monte Carlo simulation of single muons coming from the interaction point, using the Kalman filter fit method. The simulations with both aligned and mis-aligned stations gave satisfactory results. Overall the procedure can be considered ready to be applied to real muons coming from the collisions.

The first real cosmic rays were collected during this thesis work and were used for local alignment with the Kalman filter fit and the Histogram Based methods. Though the Muon Detector was not devised for the cosmic ray geometry, the alignment procedure, properly adjusted, pointed out a possible mis-alignment which can be interpreted either as a mis-alignment of a half-station or as a shearing of half of the detector. With a local alignment no discrimination between the two types of mis-alignment could be achieved.

With real cosmic rays, after a study on the distribution of residuals between the track segments reconstructed in the Muon Detector and in the OT, a relative alignment between the two detectors was attempted.

However the results were unreliable, and further investigations are in course.

The local alignment procedure with real cosmic rays was tested with Monte Carlo cosmic data using the Kalman filter fit method. The results, when obtained with data simulated with the nominal geometry of the detector and when obtained with data simulated with a mis-alignment, gave good results within the limit of a local alignment.

With the Histogram Based method a detailed study was made on the geometrical acceptance of the Muon Detector for the cosmic rays in order to understand possible systematics related to the detector layout, not suited for the cosmic rays. The sampling due to the detector granularity was found to affect the shapes of the residual distributions producing lying-S-shapes and jumps between the points along the distributions.

Appendix A

Errors on the alignment constants with different cross talk treatments

station	(a)	(b)	(c)
M1	0.03	0.05	0.03
M2	0.02	0.04	0.02
M3	0.02	0.05	0.02
M4	0.09	0.16	0.09
M5	0.10	0.18	0.11

Table A.1: Comparison of the errors on the alignment constants of the 10 half-stations aligned for translations along x (Figure 5.4 of Chapter 5). Data simulated with the detector aligned, and reconstructed with the three different treatments of the cross talk as described: (a) no cross talk is considered; (b) only the hit pad closest to the extrapolated direction; (c) the pad clustersation is taken into account.

station	(a)	(b)	(c)
M1	0.05	0.03	0.03
M2	0.04	0.02	0.02
M3	0.05	0.03	0.02
M4	0.16	0.11	0.08
M5	0.18	0.12	0.10

Table A.2: Comparison of the errors on the alignment constants of the 10 half-stations aligned for translations along x (Figure 5.5 of Chapter 5). Data simulated with the half-stations of M4 opened by 3mm (A side) and 6mm (C side), and reconstructed with the three different treatments of the cross talk as described: (a) no cross talk is considered; (b) only the hit pad closest to the extrapolated direction; (c) the pad clusterisation is taken into account.

Bibliography

[1] A. D. Sakharov, *Violation of CP invariance, C asymmetry, and baryon asymmetry in the universe*, Pisma Zh. Eksp. Teor. Fiz. **5** (1967) 32.

[2] J. H. Christenson, J. W. Cronin, V. L. Fitch and R. Turlay, *Evidence for the* 2π *decay of the* K_2^0 *meson*, *Phys. Rev. Lett.* **13** (1964) 138

[3] B. Aubert et al., Babar collaboration, *Measurement of CP violation asymmetry amplitude* $\sin 2\beta$, *Phys. Rev, Lett.* **89**, **201802** (2002)

[4] K. Abe et al., Belle Collaboration, *Measurement of CP violation parameter* $\sin 2\phi$ *with* 152 *million* B *anti-*B *pairs*, Belle-Conf-0353 (2003)

[5] The LHCb Collaboration, *Roadmap for selected key measurements of LHCb*, arXiv:0912.4179, LHCb-PUB-2009-029

[6] L. L. Chau and W. Y. Keung, *Phys. Rev. Lett.* **53** (1984) 1802
S. Eidelman et al., *Phys. Lett.* B**592** (2004) 1

[7] L. Wolfenstein, *Phys. Rev. Lett.* **51** (1983) 1945

[8] C. Amsler et al. (Particle Data Group), *Phys. Lett.* **B667** (2008) 1

[9] A. J. Buras, M. E. Lautenbacher and G. Ostermaier, *Phys. Rev.* D**50** (1994) 3433 [hep-ph/9403384]

[10] UTfit Collaboration, www.utfit.org

[11] P.F. Harrison and H.R. Quinn (editors), *The BaBar physics book*, SLAC-R-504 (1998)

[12] S. L. Glashow, J. Iliopoulos and L. Maiani, *Weak Interactions with Lepton-Hadron Symmetry*, *Phys. Rev.* D **2** (1970) 1285

[13] S. P. Martin, *A Supersymmetry Primer*, [hep-ph/9709356]

[14] E. Gabrielli and G. F. Giudice, *Nucl. Phys.* B*433* (1995) 3, [hep-lat/9407029]

[15] G. Buchalla et al., *B, D and K decays, report on the CERN workshop:Flavor in the era of the LHC* [arXiv:0801.1833] (2008).

[16] T. Aaltonen et al, CDF collaboration, *Phys. Rev. Lett.* **100** 101802, (2008)

[17] D0 collaboration, D0 public note 5344-CONF, (2007)

[18] *The LHC machine*, 2008 JINST 3 S08001

[19] The ALICE Collaboration, *The ATLAS Detector at the CERN Large Hadron Collider*, 2008 JINST 3 S08003

[20] The ALICE Collaboration, *The ALICE Detector at the CERN LHC*, 2008 JINST 3 S08002

[21] The CMS Collaboration, *The CMS Detector at the CERN LHC*, 2008 JINST 3 S08004

[22] The LHCb Collaboration, A. Augusto Alver Jr et al., *The LHCb Detector at the LHC*, 2008 JINST 3 S08005

[23] E. Aslanides, J.-P. Cachemiche, J. Cogan, P.-Y. Duval, R. Le Gac, R. Hachon, O. Leroy, P.-L. Liotard, F. Marin, and A. Tsaregorodtsev, *Conception and validation software tools for the level 0 muon trigger of LHCb*, LHCb-CONF-2009-030

[24] LHCb Collaboration, *LHCb Muon system: second Addendum to the Technical Design Report*, CERN-LHCC-2005-012

[25] R. Fruhwirth, T. Todorov and M. Winkler, *Estimation of detector alignment parameters using the Kalman filter with annealing*, J. Phys. G **29** (2003) 561.

[26] J. A. Hernando, and E. Rodrigues, *Tracking Event Model*, LHCb Internal Note, LHCb-2007-007. CERN-LHCb-2007-007

[27] V. Blobel, *Software alignment for tracking detectors*, Nucl. Instrum. Meth. A **566** (2006) 5

[28] W. Hulsbergen, *The global covariance matrix of tracks fitted with a Kalman filter and an application in detector alignment*, Nucl. Instrum. Meth. A **600** (2009) 471

[29] R. E. Kalman, *A new approach to linear filtering and prediction problems*, Trans. ASME J. Bas. Eng. **D82** (1960) 35.

[30] J. van Tilburg, *Track Simulation and Reconstruction in LHCb*, CERN-THESIS-2005-040 (2005).

[31] W. Baldini, J. Blouw, S. Blusk, N. Gilardi, O. Deschamps, F. Maciuc, J. Nardulli, A. Papanestis, C. Parkes, S. Viret, M. Needham, J. van Tilburg, S. Vecchi, and K. Vervink, *LHCb alignment strategy*, LHCb Internal Note, LHCb-2006-035

[32] S. Amato, A. Satta, B. Souza de Paula, and L. De Paula, *Hlt1 Muon Alley Description*, LHCb-2008-058, CERN-LHCb-2008-058

[33] G. Barrand et al, *GAUDI - A software architecture and framework for building HEP data processing applications*, Proceedings CHEP 2000, Padova, Italy, Feb. 2000

[34] LHCb Collaboration, *The GAUDI Project*, `http://proj-gaudi.web.cern.ch/proj-gaudi/`

[35] T. Sjöstrand, S. Mrenna and P. Skands, *PYTHIA 6.4 Physics and Manual*, hep-ph/0603175, 2006

[36] D. J. Lange, *The EvtGen particle decay simulation package*, Nucl. Instr. and Methods A **462** (2001) 152

[37] Geant4 Collaboration, *The GEANT4 Toolkit*, `http://geant4.web.cern.ch/geant4/`

[38] S. Agostinelli et al. [GEANT4 collaboration], *GEANT4: A simulation toolkit*, Nucl. Instrum. Meth. **A506** (2003) 250

[39] LHCb Collaboration, *The GAUSS Project*, `http://lhcb-release-area.web.cern.ch/LHCb-release-area/DOC/gauss/`

[40] LHCb Collaboration, *The BOOLE Project*, `http://lhcb-release-area.web.cern.ch/LHCb-release-area/DOC/boole/`

[41] LHCb Collaboration, *The BRUNEL Project*, `http://lhcb-release-area.web.cern.ch/LHCb-release-area/DOC/brunel/`

[42] LHCb Collaboration, *The DAVINCI Project*, `http://lhcb-release-area.web.cern.ch/LHCb-release-area/DOC/davinci/`

[43] LHCb Collaboration, *The PANORAMIX Project*, `http://lhcb-release-area.web.cern.ch/LHCb-release-area/DOC/panoramix/`

[44] A. Satta, *Muon identification in the LHCb High Level Trigger*, CERN-LHCb-2005-071.

[45] Geant4 User's Documents page, `http://geant4.web.cern.ch/geant4/G4UsersDocuments/Overview/html/index.html`

[46] H. A. Bethe, *Molière's Theory of Multiple Scattering*, Phys. Rev. **89** (1953) 1256

[47] S. Goudsmit, and J. L. Saunderson, *Multiple Scattering of Electrons* Phys. Rev. **57** (1940) 24

[48] H. W. Lewis, *Multiple Scattering in an Infinite Medium*, Phys. Rev. **78** (1950) 526.

[49] G. Martellotti, R. Nobrega, E. Furfaro, G. Penso, and D. Pinci, *Study of the performance of the LHCb MWPC with cosmic rays* LHCb Public Note LHCb-2008-056, CERN-LHCb-2008-056

[50] A. Sarti, R. Nobrega, and A. Kashchuk, *Procedure for determination and setting of thresholds implemented in the LHCb Muon system*, LHCb Public Note, LHCb-2008-052. CERN-LHCb-2008-052

[51] G. Manca, L. Mou, and B. Saitta, *Studies of Efficiency of the LHCb Muon Detector Using Cosmic Rays* LHCb-INT-2009-026., CERN-LHCb-INT-2009-026

[52] G. Manca, L. Mou, and B. Saitta, *Studies of Efficiency of the LHCb Muon Detector Using Cosmic Rays* LHCb-PUB-2009-017. CERN-LHCb-PUB-2009-017

[53] J. J. Hopfield and D. W. Tank, *Disordered system and biological organization*, Springer-Verlag, Berlin, 1985.

[54] R. Muresan and M. Pentia, *Hopfield neural network in hep track reconstruction*, 1995.

[55] O. Callot, and M. Schiller, *PatSeeding - A standalone track reconstruction algorithm* LHCb-2008-042, CERN-LHCb-2008-042

[56] G. Manca, L. Mou, and B. Saitta, *Monte Carlo Generator for Cosmic Ray Events in the LHCb Detector*, LHCb Internal Note, LHCb-INT-2010-001. CERN-LHCb-INT-2010-001

[57] D. Reyna, *A Simple Parameterization of the Cosmic-Ray Muon Momentum Spectra at the Surface as a Function of Zenith Angle*, [arXiv:hep-ph/0604145v2]

Acknowledgements

Thanks to Prof. Mauro Savriè and to Dr. Stefania Vecchi for their supervision and stimulating criticisms. Through this work I was introduced in the amazing world of CERN and had the opportunity to work with the very first real data acquired by the detector, when real particles were still a mirage for most of the people of the LHCb community. From my point of view, as a theoretical physicist, this was an exciting moment.

Thanks to Prof. Bepo Martellotti for his suggestions and for the time he spent relating weird plots to the features of the Muon Detector.

Thanks to Dr. Wouter Hulsbergen for his patient explanations. Sorry for having an Italian keybord on my laptop, but this handicap that slowed you (just) a bit, allowed me to understand (just) a bit more.

Thanks to Jan Amoraal for being a, not always very patient, LaTex /python/C++/alignment framework living manual.

To all the others, many thanks for their friendship, support, help, patience, comprehension and love.

Abstract

The phenomenology of particle physics is well described by the Standard Model. However, some of the parameters of the model are not predicted and have to be experimentally determined, as for instance, the four parameters of the quark mixing matrix, the Cabibbo-Kobayashi-Maskawa (CKM) matrix. One of these parameters, the phase of the CKM matrix, is responsible of the violation of the CP symmetry that was identified as one of the causes for the asymmetry between matter and anti-matter in the Universe [1].

LHCb is one of the four experiments of particle physics at the Large Hadron Collider accelerator built at CERN.

The LHCb experiment is dedicated to high precision measurement of CP violating parameters in the system of B mesons. The large samples of $B - \overline{B}$ pairs that will be produced allow to measure very rare B decays like $B_s \rightarrow \mu^+\mu^-$. The branching ratio predicted by the Standard Model for this decay is of the order of $O(10^{-9})$, but it can receive large contributions by virtual processes involving new particles.

The challenge of the LHCb experiment is to efficiently discriminate the events of interest from the background produced by the $p - p$ colli-

sions. For this reason the experiment is equipped not only with specific detectors, but also with an efficient trigger system, in which the Muon Detector plays an important role. The Muon Detector task, in the first stage of the trigger system, is the detection of muons with high transverse momentum[1]. Moreover, in the high level trigger and in the off-line reconstruction the Muon Detector provides the muon identification. The information on muons in the final states of B meson decays are used by the tagging algorithms for the determination of the b flavour of the decaying B mesons. This procedure is of great relevance in CP violation measurements.

Because of the role it plays in the experiment, it is crucial to know the actual position of the Muon Detector, and to monitor it during the time. This is the aim of the software alignment of the detector and the subject of this thesis.

The software procedure to align the Muon Detector, locally and globally, has been carried out developing specific algorithms for the track finding and reconstruction. The reconstructed tracks have been expressed in the standard LHCb track format and fitted with the default LHCb track fit method. The Muon Detector software alignment procedure has been tested with three kinds of data: Monte Carlo muons coming from the interaction point, real cosmic rays and Monte Carlo cosmic data. The real cosmic rays, analysed in this work, have been the first experimental data ever acquired by LHCb.

This thesis is divided in the following chapters:

[1]Given the large mass of the B mesons, their decay products have a transverse momentum larger than the background particles.

Chapter 1 describes the CP violation in the Standard Model of particles with the phenomenology of interest in the LHCb experiment.

Chapter 2 briefly describes LHC and then discusses all the detectors that constitute the LHCb experiment.

Chapter 3 is entirely dedicated to the Muon Detector for its relevance to this thesis.

In Chapter 4 the alignment methods used are described.

Chapter 5, after a brief description of the LHCb software organisation, discusses the first test of the global alignment procedure applied to the Muon Detector, and performed with Monte Carlo data of single muons coming from the interaction point.

With real cosmic rays a local alignment of the Muon Detector was performed. In addition a preliminary study for a relative alignment of the detector with respect to the Outer Tracker was also carried on. This is the subject of Chapter 6.

In Chapter 7 a Monte Carlo cosmic data sample has been produced for testing the local alignment performed with real cosmic rays and for studying local systematics arising from the acceptance of the Muon Detector unsuited for the cosmic ray geometry.

Sommario

La fenomenologia della fisica della paticelle elementari è ben descritta dal Modello Standard. Tuttavia il modello non predice alcuni parametri, che devono essere determinati sperimentalmente, come ad esempio i quattro parametri della matrice di mixing dei quark, la matrice di Cabibbo-Kobayashi-Maskawa (CKM). Uno di questi parametri, la fase della matrice CKM, è il responsabile della violazione della simmetria CP, che viene considerata una delle cause dell'asimmetria tra materia e antimateria nell'Universo [1].

LHCb è uno dei quattro esperimenti di fisica delle particelle elementari al collider adronico LHC del CERN.

L'esperimento LHCb è dedicato a misure di alta precisione dei parametri che violano CP nel sistema dei mesoni B. La grande quantità di coppie $B - \overline{B}$ che può essere prodotta permetterà infatti la misura di decadimenti rari del B come $B_s \to \mu^+\mu^-$. Il *branching ratio* predetto dal Modello Standard per questo decadimento è dell'ordine $O(10^{-9})$, ma può ricevere grandi contributi da processi virtuali che coinvolgono nuove particelle.

La sfida di LHCb è quella di essere in grado di discriminare con effi-

cienza gli eventi di interesse dal fondo prodotto dalle collisioni $p - p$.

A questo scopo l'esperimento è dotati non solo di rivelatori specifici, ma anche di un efficiente sistema di *trigger* in cui il Rivelatore di Muoni riveste un ruolo importante. Compito di questo rivelatore, nel primo stadio del sistema di trigger è la rivelazione di muoni di alto impulso trasverso[2]. Inoltre, nel trigger di alto livello e nella ricostruzione off-line il Rivelatore di Muoni fornisce l'identificazione dei muoni. Le informazioni sui muoni presenti negli stati finali dei decadimenti dei mesoni B vengono utilizzate dagli algoritmi di tagging per la determinazione del contenuto in quark b del mesone B. Questa procedura riveste grande importanza nelle misure di violazione di CP.

A causa del ruolo che ha nell'esperimento, è di fondamentale importanza la conoscenza della posizione effettiva del Rivelatore di Muoni, e il suo controllo nel tempo. Questo è lo scopo dell'allineamento software del rivelatore, e l'oggetto di questa tesi.

La procedura di allineamento software del Rivelatore di Muoni, locale e globale, è stata portata a termine sviluppando algoritmi specifici per la ricerca e la ricostruzione delle tracce. Le tracce ricostruite sono espresse nel formato standard di LHCb e sono sottoposte al fit di traccia con il metodo di default in LHCb. La procedura di alineamento software del Rivelatore di Muoni è stata verificata con tre diversi tipi di dati: muoni Monte Carlo provenienti del punto di interazione, raggi cosmici reali e raggi cosmici Monte Carlo. I raggi cosmici reali, analizzati in questo lavoro, sono stati i primi dati sperimentali acquisiti da LHCb.

[2]Data la grande massa dei mesoni B i loro prodotti di decadimento hanno un impulso trasverso maggiore delle particelle che costituiscono il fondo.

Questa tesi si divide nei seguenti capitoli:

Il Capitolo 1 descrive la violazione di CP nel Modello Standard delle particelle elementari insieme alla fenomenologia che interessa l'esperimento LHCb.

Il Capitolo 2 descrive brevemente LHC e discute i rivelatori che costituiscono l'esperimento LHCb.

Il Capitolo 3 è interamente dedicato al Rivelatore di Muoni, per l'importanza che esso riveste per questa tesi.

Nel Capitolo 4 vengono descritti i metodi di allineamento software usati.

Il Capitolo 5, dopo una breve descrizione dell'organizzazione del software di LHCb, discute le prima verifica della procedura di allineamento globale del Rivelatore di Muoni usando dati Monte Carlo di muoni singoli provenienti dal punto di interazione.

Con raggi cosmici veri è stato effettuato l'allineamento locale del rivelatore. Inoltre sono stati fatti degli studi prelimninari per un allineamento relativo tra il Rivelatore di Muoni e l'Outer Tracker. Questo è trattato nel Capitolo 6.

Nel Capitolo 7 si descrive l'allineamento locale effettuato con campioni di raggi cosmici Monte Carlo, per verificare l'allineamento locale effettuato con raggi cosmici reali. Inoltre sono state studiate le sistematiche locali dovute alle caratteristiche dell'accettanza del Rivelatore di Muoni incompatibile con la geometria dei raggi cosmici.